DEVELOPMENT OF RADIOFREQUENCY CARPETS FOR ION TRANSPORT AT THE NSCL

By

Gregory Keith Pang

A DISSERTATION

Submitted to
Michigan State University
in partial fulfillment of the requirements
for the degree of

DOCTOR OF PHILOSOPHY

Chemistry

2011

ProQuest LLC.
789 East Eisenhower Parkway
P.O. Box 1346
Ann Arbor, MI 48106 - 1346

ABSTRACT

DEVELOPMENT OF RADIOFREQUENCY CARPETS FOR ION TRANSPORT AT THE NSCL

By

Gregory Keith Pang

The low-energy research program at the NSCL is dependent on gas thermalization techniques to convert the energetic nuclear reaction products (100 MeV/u) from projectile fragmentation reactions into high quality low-energy beams (eV). The NSCL is currently developing a gas-filled reverse cyclotron to provide a high stopping efficiency for the incoming fast beams at pressures that will allow rf ion-guiding techniques to be effective. In this work, the development and characterization of rf carpets for the efficient ion-guiding and extraction of projectile fragments from a cyclotron gas stopper was achieved. The transport of Rb ions within the pressure range expected for cyclotron gas stopper operation of 40 - 110 torr and over transport distances (up to 40 cm) were investigated. Ion extraction from the rf carpet was also successfully demonstrated. This work shows that large rf carpets can be constructed that will work in the cyclotron gas stopper.

ACKNOWLEDGMENTS

Before I thank anyone, I would like to give a special thanks to the graduate program in nuclear chemistry (and physics) at the NSCL. I could not have asked for a better place to do my graduate research with regards to personnel, opportunities, and resources.

In preparation of this thesis, many thanks have to go to my advisor Dave Morrissey for giving his corrections and feedback. I would also like to thank my family and friends for all their support during my graduate years. Thanks to all LEBIT/Gas Cell members past and present. You have become some of my closest friends.

Upon leaving, I will certainly miss the intelligent discussion during the Cycstopper/Rf carpet meetings. I will miss Dave Morrissey's intuition, Georg Bollen's enthusiasm, and Stefan Schwarz's technical expertise.

Finally, I'd like to thank again my advisor Dave Morrissey and Georg Bollen for giving me such sound advice throughout my graduate career.

You all have taught me more than I know.

Table of Contents

List of Tables

List of Figures

Chapter 1

Introduction

The thermalization of fast ion beams is a proven technique to convert the energetic nuclear reaction products (100 MeV/u) from projectile fragmentation reactions in to suitable low energy beams (eV) for precision experiments at the NSCL [5–7]. The NSCL has demonstrated the thermalization through the success of its low-energy program originally centered on precision mass measurements of exotic nuclei with the LEBIT [8] experimental setup and is expanding the low-energy program at the NSCL to include colinear laser spectroscopy. In addition to the low-energy experiments, the thermal ions will be used to provide ions for further reacceleration. The effectiveness of thermalization of fast ions in a buffer gas can also be seen in the growing number of experimental programs around the world that are developing the ability to thermalize a wide energy range of reaction products from projectile fragmentation, fusion-evaporation reactions and nuclear fission. [3, 5, 9, 10]. As more experimental programs incorporate thermalization in gas, the technique will need to constantly evolve and improve to satisfy the increasing demand to measure nuclei at the limits of stability. In the vein of improving this technique, the goal of this dissertation was to develop techniques for the efficient transfer of ions after thermalization in a buffer gas to a central point for collection within the operating conditions of a cyclotron gas stopper [2, 11, 12].

This introductory chapter will first cover the basic principles and limitations of linear gas catchers and gas cells that are presently used to thermalize fast ion beams. Then, possibly

removing these limitations in the form of the cyclotron gas stopper will be described and the need for the development of the ion-guiding techniques described will become apparent.

1.1 Gas thermalization methods

All of the currently used gas catchers utilize the same general techniques to thermalize fast ion beams. After the fast fragments are slowed down using solid degraders, the ions are thermalized in a chamber filled with high-purity He gas. Due to the high ionization potential of He, the thermalized ions remain singly or doubly-charged and are guided towards the extraction orifice of a cylindrical gas chamber with electric fields. Once at the extraction orifice, gas flow is used to sweep the ions out of the gas chamber. The differences in devices lies in the gas pressure used and the different combinations of dc and/or rf electric fields used to guide the ions towards the extraction orifice.

The two major different approaches to thermalization have relied on 1) a high stopping efficiency by having a high gas pressure (up to 760 torr) and a short stopping length, but with limited ion-guiding with only dc fields due to the reduced effectiveness of using rf electric fields(discussed in Ch. 2). 2) A reduced gas pressure (∼80 torr) and a long stopping path in the stopping chamber with a low stopping efficiency and a combination of dc and rf electric fields to focus and collect the ions. The original NSCL linear gas cell [5–7] was operated with the former approach, and the current RIKEN gas cell [3, 4] is operated with the latter approach. The equivalent gas thickness is given by the product of the chamber pressure and length of the chamber ($p \cdot l$), and for example, a $p \cdot l$ of 0.5 bar-m of He gas is required to thermalize 100% of energetic beams ($A > 60$) of approximately 100 MeV/u. Thus, a gas catcher operated at 1 bar with a chamber length of 0.5 m and and another gas catcher operated at 0.5 bar with a chamber length of 1 m would have an equivalent target thickness. An important parameter in the gas thermalization of rare isotopes is the ion extraction time, which is dependent on the $p \cdot l$ parameter and the strength of the electric field used to guide the ions towards the extraction orifice. Taking a typical electric field strength of 10 V/cm, the

typical reduced ion mobility of K = 20 $cm^2/V{\cdot}s$ for medium mass ions in He gas, a $p \cdot l$ of 0.5 bar-m and a chamber at room temperature (298 K), corresponds to an ion extraction time of 230 ms for ions traveling from the entrance window of the gas chamber to the exit of the gas cell. For the same parameters and a uniform stopping distribution in the gas chamber, the average ion extraction time would be 125 ms. These extraction times impose a limitation in the study of rare isotopes with the shortest half-lives. Reducing these extraction times could be achieved by lowering $p \cdot l$, but this would correspond to a lower stopping efficiency. Lowering $p \cdot l$ would have an even greater impact on light ions because light ions require a longer stopping range because the stopping power, dE/dx, is proportional to Z^2. The RIKEN gas cell (length of 2 m and a pressure of 80 torr) reports a stopping efficiency of only 11% for incident ^{8}Li ions [4]. However, significantly increasing $p \cdot l$ to thermalize 100% of the light ions results in longer extraction times.

At this point, it is useful to introduce the stopping efficiency, extraction efficiency, and the product of both efficiencies which results in the overall efficiency. The stopping efficiency, ϵ_{stop}, is given by the expression:

$$\epsilon_{stop} = \frac{N_{stop}}{N_{incoming}} \tag{1.1}$$

where N_{stop} and $N_{incoming}$ refer to the number of stopped ions and the number of incoming ions respectively. The extraction efficiency, $\epsilon_{extract}$, is given by the expression:

$$\epsilon_{extract} = \frac{N_{extract}}{N_{stop}} \tag{1.2}$$

where $N_{extract}$ is the number of extracted ions. The overall or total efficiency, ϵ_{tot}, is then given by the final expression:

$$\epsilon_{tot} = \epsilon_{stop} \times \epsilon_{extract} = N_{extract}/N_{incoming}. \tag{1.3}$$

In general, with linear gas catchers, there is a tradeoff between stopping efficiency and

extraction efficiency because of the impact of the $p \cdot l$ parameter. A higher stopping efficiency could be gained by increasing $p \cdot l$ at the cost of increasing ion extraction times and if applicable, reducing the effectiveness of rf ion-guiding techniques. Thus, for linear gas catchers, the total efficiency cannot be maximized.

1.2 Limitations of current gas thermalization techniques

With current gas catchers, there has been evidence of decreasing extraction efficiency with increasing beam rate. These ion losses occur because of the ionization of the He gas during

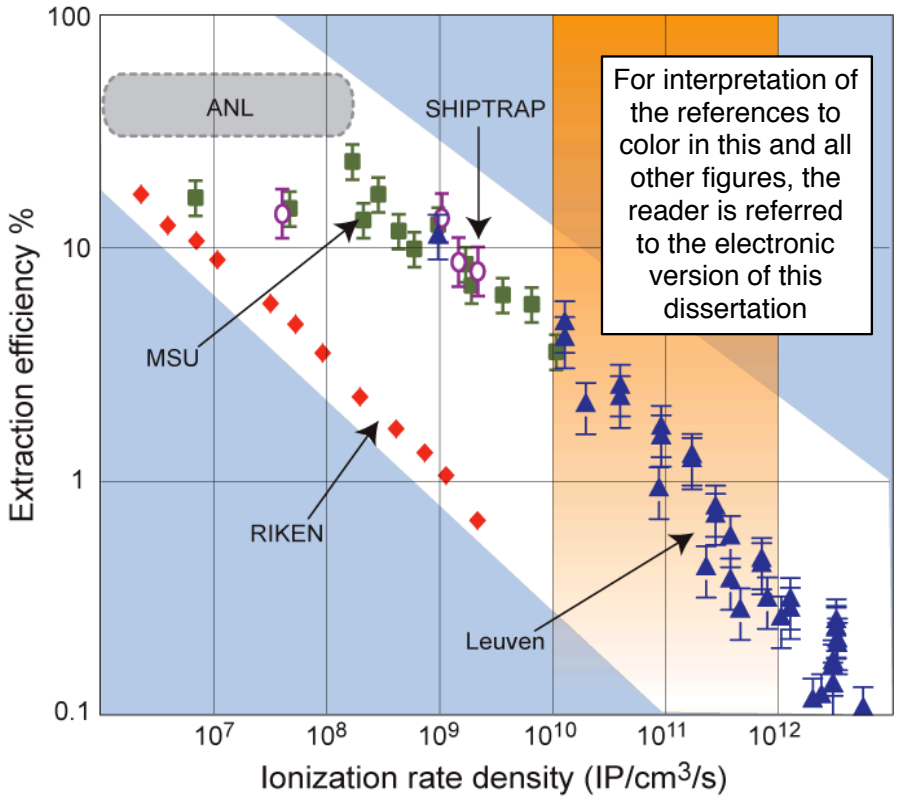

Figure 1.1: Compilation of the observed extraction efficiencies as a function of ionization rate density (number of buffer gas ion-electron pairs (IP) per unit gas volume per time) for linear gas stopping stations (adopted from [1]). For interpretation of the references to color in this and all other figures, the reader is referred to the electronic version of this dissertation.

the slowing down of the incoming ions. The free electrons have a drift velocity in He gas approximately three orders of magnitude greater than the Helium ions, so the electrons are

removed quickly due to the applied fields in the gas cell, leaving the remaining positive charge of He ions in the stopping volume. This large remaining positive charge, or space charge, pushes the desired (positive) ions towards the walls of the gas cell. Without ion confinement in the radial direction, the desired ions would be lost by collisions with the electrodes. Thus, the critical parameter of these devices is the ionization rate density, Q (number of buffer gas ion-electron pairs (IP) per unit gas volume per time), that was introduced by Huyse [13]. The compilation of the extraction efficiency of various gas cells as a function of Q is shown in Fig. 1.1 [1].

High-energy (100 MeV/u) beam rates of 10^5 /s into linear gas catchers have already been observed in experiments [4,6] and confirmed through calculations [4] to result in a loss in extraction efficiency of the thermalized ions. Reducing the space charge effects that are primarily responsible for this loss in efficiency can be achieved by operating rf ion-guiding devices in a manner such that the He ions have an unstable motion and are lost by collisions with the electrodes, whereas the typically heavier ions of interest have a stable motion and are safely guided along the electrodes.

1.3 Proposed solution: cyclotron gas stopper

In order to confront the problems introduced in the previous section, the NSCL is developing a new device to thermalize fast ion beams, called the cyclotron gas stopper [2, 11]. In this device, the stopping chamber is located in a cyclotron magnet, that confines the incident ions during the deceleration process. A conceptual drawing of such a device is shown in Fig. 1.2. The energetic beam is injected into the system and encounters an adjustable solid degrader to degrade the beam, so that the resultant beam follows an inwards spiral path and is thermalized near the center of the magnet. A sample trajectory of an ion in the system along with the distribution of stopped ions near the center of the system from simulations is shown in Fig. 1.3.

The cyclotron gas stopper will provide a much longer stopping path length for the ions to

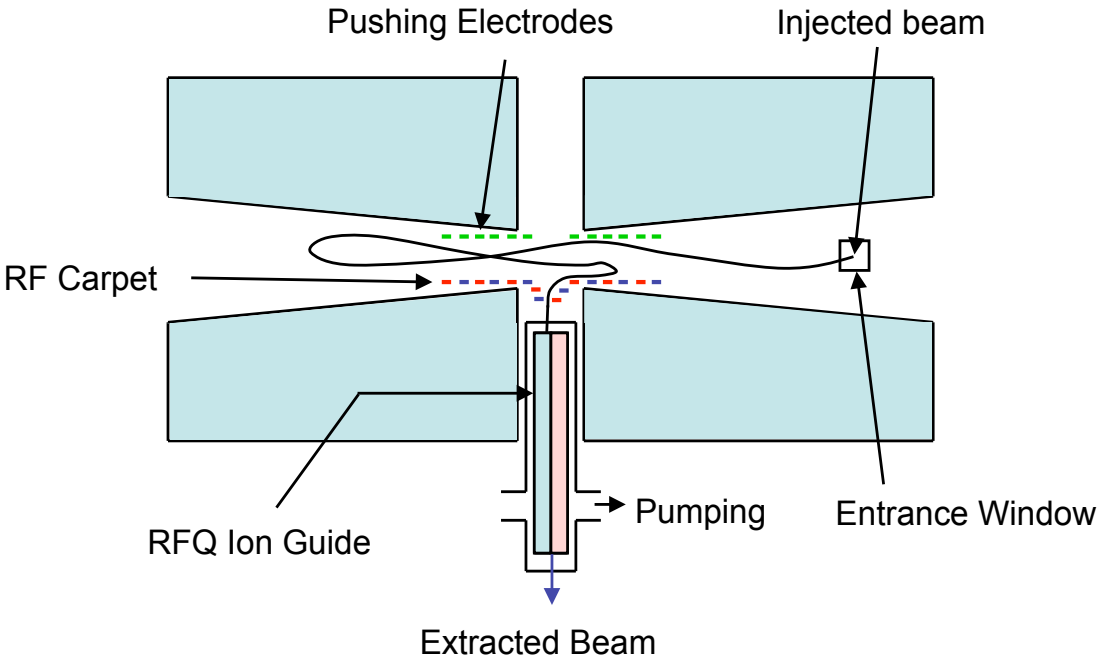

Figure 1.2: Conceptual drawing of a cross-sectional view of the cyclotron gas stopper. The ions are stopped close to the center of the device. Adopted from [2].

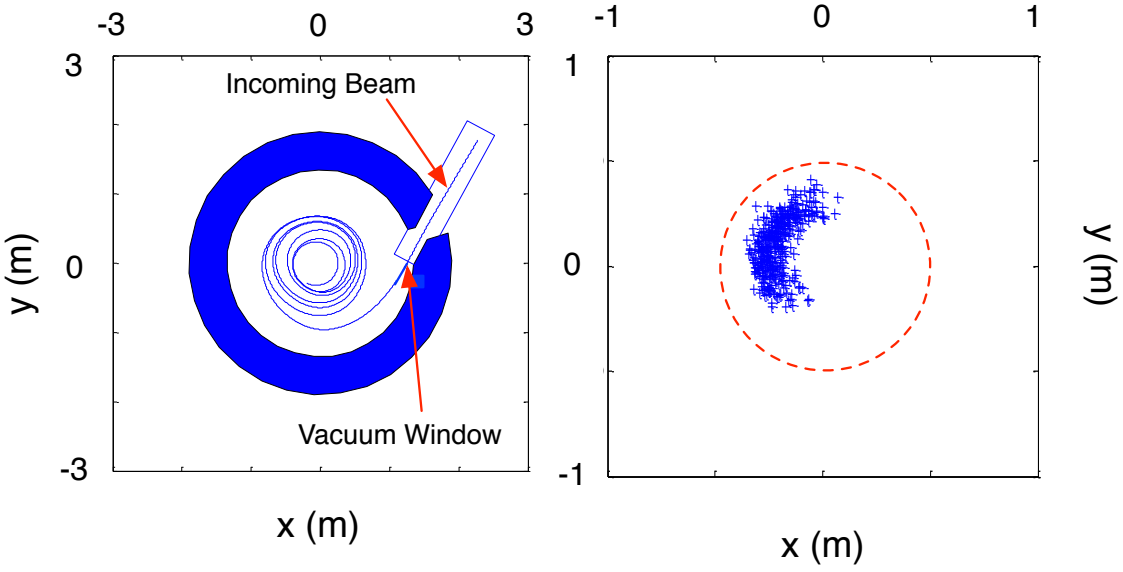

Figure 1.3: Left: Sample trajectory from simulations of a ^{79}Br ion passing through the system at a gas pressure of 175 mbar. Solid degrader not shown. Right: The final distribution of ^{79}Br ions in the system at a gas pressure of 175 mbar. The red circular dashed line has a radius of 50 cm and indicates the area in which the ions are thermalized.

Table 1.1: Stopping efficiencies for the cyclotron gas stopper at 100 mbar

Ion	ϵ_{stop} (no add. degraders)	ϵ_{stop} (with add. degraders)
^{127}I	72%	n/a
^{79}Br	82%	n/a
^{16}O	47%	60%

decelerate than can be achieved in a linear gas catcher, therefore increasing the l component in the $p \cdot l$ parameter, and allowing for higher stopping efficiencies at reduced pressures. The stopping efficiencies from simulations performed by the NSCL to study the thermalization of ions produced from projectile fragmentation in the cyclotron gas stopper for various species based upon this baseline concept and also a more advanced concept of adding solid degraders azimuthally around the gas-filled chamber is shown in Table. 1.1. Additional solid degraders placed at large radii inside the chamber will allow for lower operating pressures to thermalize the light ions. The stopping efficiencies were found to range from 60 - 90% at 100 mbar (80 torr) for the various species studied. At the same time, the reduced pressures will allow rf ion-guiding techniques to be more effective and should provide higher extraction efficiencies. As opposed to traditional linear cells in which the collection path length is on the same scale as the stopping path length, and are both limited by the same $p \cdot l$, the cyclotron gas stopper has a separate l component for the stopping path length and the collection path length.

The cycstopper simulations also show ions are typically thermalized within 50 cm of the extraction orifice that is located on the central axis. Located in the magnet yoke is a rf quadrupole ion guide that will be used to guide the ions through the differentially pumped region. Transport of the ions from the region in which they are thermalized to the extraction orifice will require a transport method to have the following properties: 1) Operate efficiently in the pressure regime of the cyclotron gas stopper, 2) Efficiently transport ions over distances approaching 50 cm, and 3) Efficiently transport ions through an extraction orifice. The transport method will require an electrostatic field to push the ions (designated throughout the text as the push field) towards the half of the magnet yoke in which the extraction orifice is located. Another electrostatic field (designated the drag field) is required

to guide the ions in towards the central axis. The ions will be prevented from colliding with the electrodes by a repelling force provided by an alternating-gradient focusing device.

Fast extraction times are still necessary to study rare isotopes with the shortest half-lives, but will still be determined by the strength of the drag field that guides the ions towards the extraction orifice and the pressure in the stopping chamber. Again, taking a typical electric field strength of 10 V/cm, the typical reduced ion mobility of K = 20 $cm^2/V{\cdot}s$ for medium mass ions in He gas, and now a chamber pressure of 100 mbar and a distance of 50 cm, results in ion extraction times of approximately 25 ms. The operation of rf carpets will be described in detail in the following chapters. The details of such a device will be introduced in the following section and discussed in detail throughout the remainder of this text.

1.4 The need for RF carpets

Once the ions are thermalized near the center of the cyclotron gas stopper, the ions must be guided efficiently towards the extraction orifice located on the central axis and then extracted through the yoke. The advantages in the stopping characteristics of the cyclotron gas stopper would be lost unless ions could be guided and extracted efficiently out of the stopping chamber.

Given the geometry of the cyclotron gas stopper, electrostatic fields and the repelling force provided by an rf carpet can be used to guide the ions towards the extraction orifice. Rf carpets were first developed by M. Wada at RIKEN [3] and are currently in use in their linear gas cell. A photograph of a rf carpet used by M. Wada is shown in Fig. 1.4. Rf carpets consist of a planar arrangement of electrodes (M. Wada used concentric electrodes, but the present study used a variety of electrode shapes) in which rf voltages 180° out of phase on adjacent electrodes, provides a repulsive force that is related to the ion confinement properties of a quadrupole ion guide. A dc gradient, the drag field, is superimposed on the rf carpet electrodes to guide the ions towards the center of the system and the extraction orifice. A constant electric field perpendicular to the rf carpet, the push field, is responsible

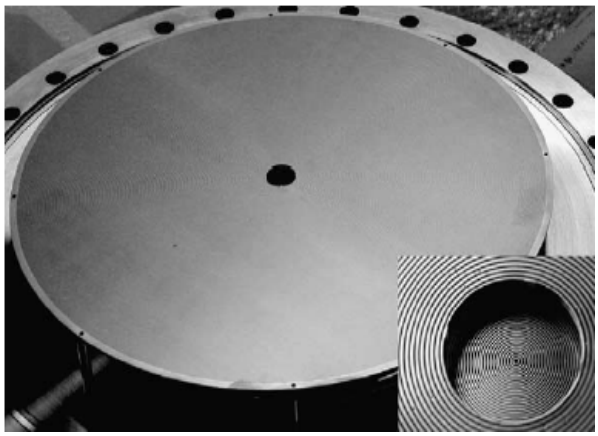

Figure 1.4: Photograph of a ion collection system with a rf carpet from RIKEN [3]. The top electrode system has a diameter of 29 cm with 280 electrodes and a central hole of 10 mm. It is only biased with dc voltages [4] and is used to guide the ions towards the rf carpet (insert). The rf carpet is located below the top electrode system and has a diameter of 3 cm with 43 electrodes and an exit hole of 0.6 mm.

for pushing the ions towards the rf carpet and resulting in nice potential minima directly above the rf carpet.

The motivation of this work was to develop, characterize, and demonstrate a method using rf carpets to transport ions from the central region of a cyclotron gas stopper to the extraction orifice. One of the main challenges of the project was the size the system needed to collect all the thermalized ions (1 meter in diameter based on simulations). The size was also the main difference between the previous uses of rf carpets at RIKEN that were restricted to short ion transport distances ($\sim$5 cm). Transporting ions over a distance approaching 50 cm with a planar rf carpet and the characterization of this device was unique to this project. In addition to the study being an essential component to the cyclotron gas stopper, any information gained could also be applied to the development of next-generation linear gas cell.

Chapter 2

Ion confinement with radiofrequency (rf) carpets & early simulations

Radiofrequency (rf) carpets control the motion of low energy ions by using inhomogeneous alternating electric fields. Devices that employ this method of ion transport and ion confinement have been used extensively in physics, chemistry, and more recently in the study of rare isotopes. Typical and ideal operating environments are in vacuum or in the presence of a dilute buffer gas. The most prevalent of these devices are multipolar rf ion guides, with the quadrupole ion guide being the most commonly employed. Since ion confinement is achieved with inhomogeneous alternating electric fields, it is instructive to begin the present discussion by introducing the differences between a homogeneous alternating electric field and an inhomogeneous alternating electric field with regards to ion confinement.

2.1 Ion confinement with inhomogeneous electric rf-fields

The confining force provided by these structures as introduced by Dehmelt [14] can be illustrated by placing an ion with charge e and mass m in between a set of parallel plates that create a homogeneous electric rf-field as shown in Fig. 2.1. If a time-dependent potential

difference, $\Phi(t)$, between the plates is given by the following equation:

$$\Phi(t) = V_0 \cdot \cos(\Omega \cdot t) \tag{2.1}$$

the ion will oscillate about its original position given by the frequency Ω of the applied rf voltage (called the micromotion). However, the instantaneous force giving rise to this micromotion or displacement averaged over time is zero and the ion's average position does not change over time.

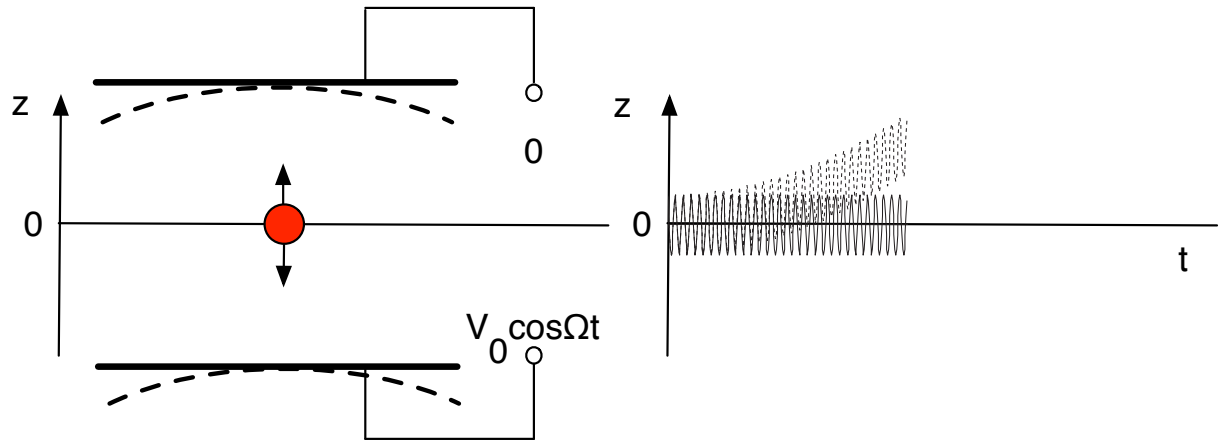

Figure 2.1: Illustration of effective force on an ion in an inhomogeneous electric rf-field. Left: Ion placed in between a set of parallel plates (solid) and curved plates (dotted). Right: Ion's position over time for the parallel plate (solid) case and curved plate (dotted) case.

By replacing the set of parallel plates with a set of curved electrodes and therefore introducing an inhomogeneous electric rf-field, the ion still undergoes a micromotion, but the micromotion now follows a non-zero average force in the direction of the weaker electric rf-field and the ion slowly drifts (called the macromotion) towards this region of weaker electric rf-field strength.

2.2 The effective potential

The confining force provided by an inhomogeneous electric rf-field has been described by the effective or pseudo-potential, V_{eff} in vacuum, given by:

$$V_{eff} = \frac{e}{4m\Omega^2}(E_0^2) \tag{2.2}$$

where e is the elementary charge, m refers to the mass of the ion, Ω refers to the frequency of the rf, and E_0 refers to the electric field strength, respectively.

2.2.1 The effect of a damping force on the effective potential

The devices used to thermalize fast rare isotope beams must operate in the presence of a buffer gas, which damps the micromotion of the ions by collisions and results in a lower effective potential and a modified form of Eq. 2.2 [3]:

$$V_{eff,damp} = \frac{\Omega^2}{\Omega^2 + D^2} V_{eff} \tag{2.3}$$

where the damping factor D has the form of:

$$D = \frac{e}{mK} \tag{2.4}$$

where the K is the ion mobility and is a direct measure of the ion's drift velocity, v_d in gas with a static electric field of strength E:

$$K = \frac{v_d}{E}. \tag{2.5}$$

The ion mobility K is commonly reported as a reduced ion mobility K_0 at standard temperature $T_0 = 273$ K and standard pressure $p_0 = 1013$ mbar. An ion traveling in a He buffer gas has a typical reduced ion mobility of approximately 20 $\text{cm}^2/\text{V}\cdot\text{s}$. Thus, the ion mobility K from the reduced ion mobility K_0 is:

$$K = K_0 \frac{p_0}{p} \frac{T}{T_0}. \tag{2.6}$$

From Eq. 2.3, we can see that the effective potential decreases with $1/p^2$ and high gas pressures renders rf techniques ineffective at confining low energy ions.

2.3 Multipolar rf ion guides

The idea of the effective potential can be extended to the most popular of the devices that employ inhomogeneous electric rf-fields, the quadrupole ion guide [15]. Consider a set of hyperbolic electrodes, in which a potential, V is applied in between the adjacent electrodes, the resultant electric quadrupole potential is:

$$\phi = V \cdot \frac{x^2 - y^2}{r_0^2} \tag{2.7}$$

where $2r_0$ is the interelectrode spacing. The electric field in x and y is then given by:

$$\vec{E}_x = -\frac{2Vx}{r_0^2} \quad , \quad \vec{E}_y = \frac{2Vy}{r_0^2}. \tag{2.8}$$

Using static potentials, the ion confinement is limited in only one direction. Applying an alternating potential modulated with a frequency Ω (e.g., rf) and substituting into Eq. 2.2 provides the following effective potential:

$$V_{eff} = \frac{e}{m} \frac{V^2 \left(x^2 + y^2\right)}{\Omega r_0^4} \tag{2.9}$$

where $x^2 + y^2 = r^2$ and results in a parabolic radial pseudopotential well. Disregarding additional effects that may lead to ion motion instability, the ions are confined to the center of the device where the potential minimum is located.

Conceptually, a quadrupole potential produced purely by static voltages produces a saddle-shape potential that cannot confine an ion in two directions. The application of an

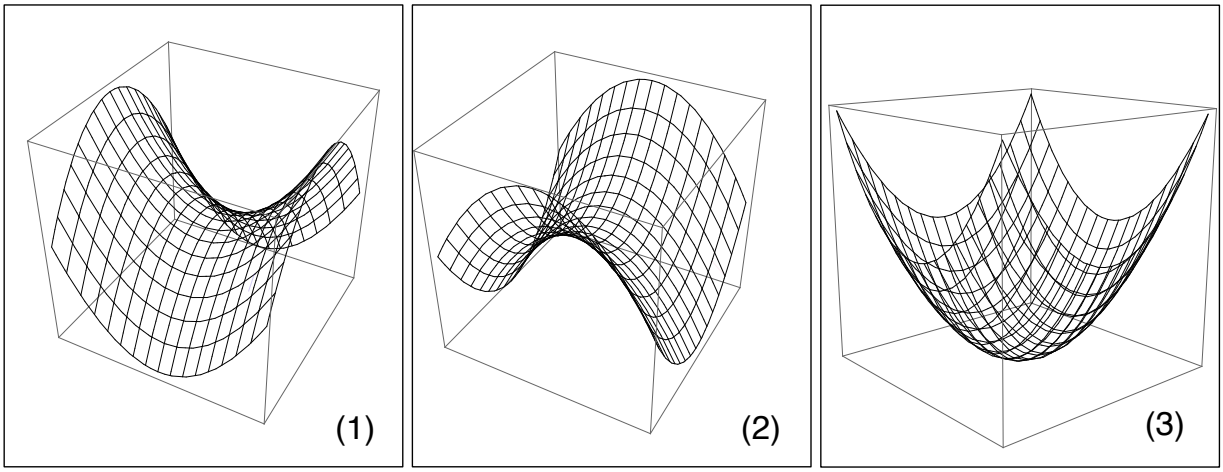

Figure 2.2: (1) Resultant quadrupole potential produced by applying a voltage in between a set of hyperbolic electrodes. (2) Scenario when reversing the polarity of the potential in (1). (3) Parabolic pseudopotential well the ion experiences if a rf potential is applied in between the electrodes.

oscillating potential alternately confines the ions in one dimension and then the other. Classically, this can be viewed as a rotation of the saddle-shape potential along its axis of symmetry so the ion experiences the resultant parabolic pseudopotential well that confines the ion in both directions. In order to achieve this in practical application, radiofrequencies ($\sim$ MHz) are used.

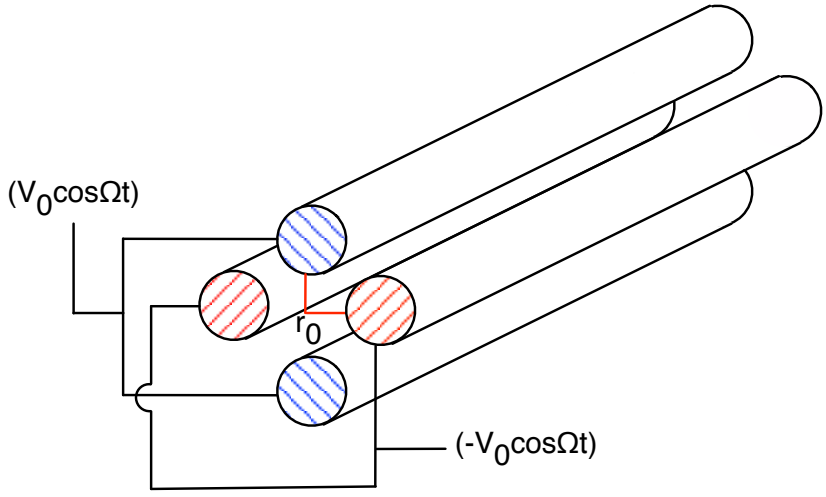

Figure 2.3: rf voltage schematic of a quadrupole ion guide. Blue and red hatched patterns represent the two different rf phases separated by 180°.

The application of rf voltages to operate multipolar rf ion guides requires rf voltages that

are 180° out of phase on adjacent electrodes. A schematic of this is shown in Fig. 2.3 for a quadrupole ion guide with rod-shaped electrodes.

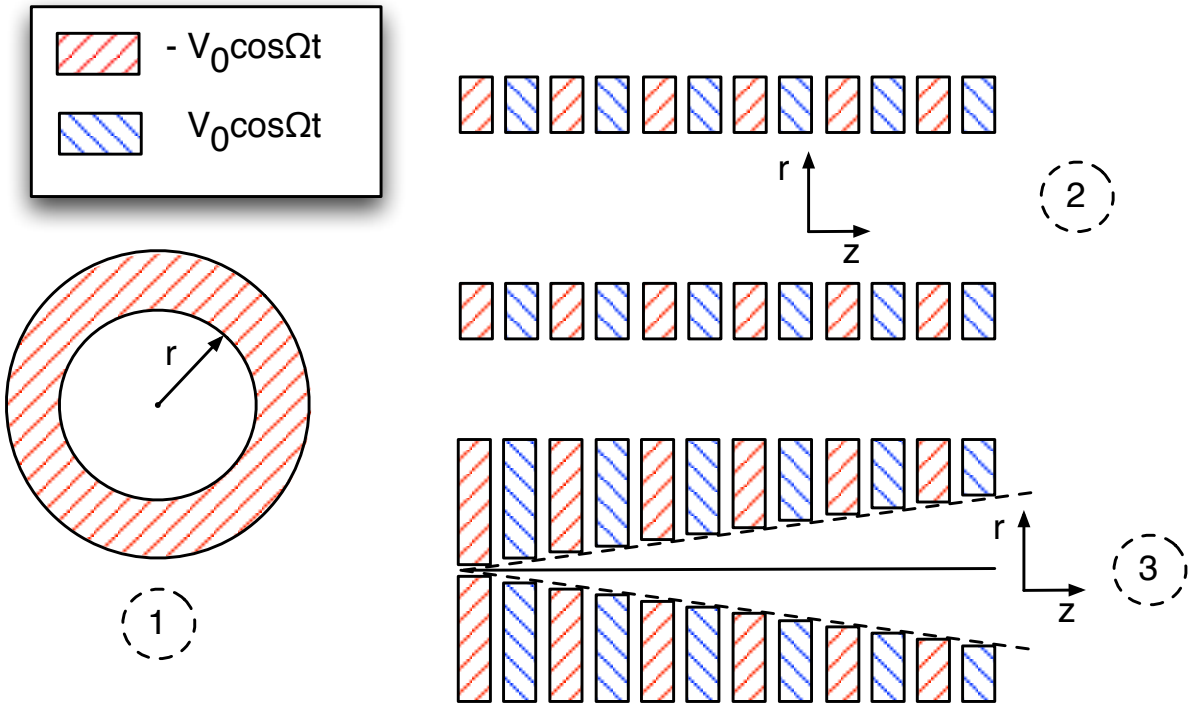

Figure 2.4: Geometrical arrangement of electrodes and rf voltage schematic of a stacked ring rf ion guide and a rf funnel. Similar to the quadrupole ion guide, blue and red hatched patterns represent the two different rf phases separated by 180°. (1) Schematic of an individual ring electrode. (2) Stacked ring rf ion guide: the inner radius is held constant. (3) Rf funnel: the inner radius has a decreasing inner diameter.

2.4 Extension: Stacked ring ion guides, rf funnels, rf carpets

These principles of ion confinement can be extended to stacked ring ion guides, rf funnels, and rf carpets. The application of rf voltages is similar to that in multipole ion guides, in which a rf voltage applied to each electrode is 180° out of phase with any adjacent electrodes. The only difference is the electrode shape in these structures. The stacked ring ion guides, as the name suggests, consists of a stack of rings with the same inner diameter. The rf funnel [16]

consists of the same axial arrangement as the stacked ring ion guides, but each electrode has a decreasing inner diameter (hence the term: funnel). Both rf funnels and stacked ring ion guides consist of discrete rings which must be fabricated individually and are on the order of fractions of a ∼mm. Rf carpets [3] differ in this respect, in which the electrodes are in a planar arrangement of concentric circles laid out on a printed circuit board (pcb). See Fig. 2.4 and 2.5.

Since the principles of ion confinement are identical for the different electrode structures, confined ions exhibit the same characteristic micro- and macromotions. An example of the ion motion along a rf carpet is shown in Fig. 2.6.

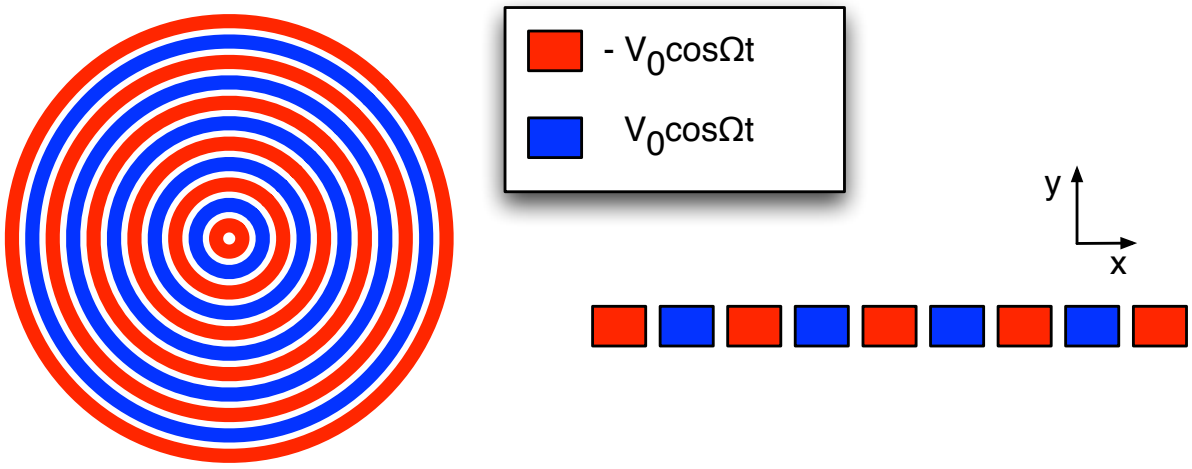

Figure 2.5: Geometrical arrangement of electrodes and RF voltage schematic for a rf carpet. The electrodes are laid out in one plane and are typically plated on printed circuit board (pcb) material. The blue and red stripes represent the two different rf phases separated by 180°.

2.5 The rf carpet effective potential

By solving for E_x and E_y for a rf carpet electrode geometry, the effective potential for a set of rf carpet electrodes in a buffer gas can be calculated using Eq. 2.3. In future discussions, the gap, g is defined as the spacing between adjacent electrodes and the pitch, a, is defined as the sum of the electrode width and the gap. From [17],

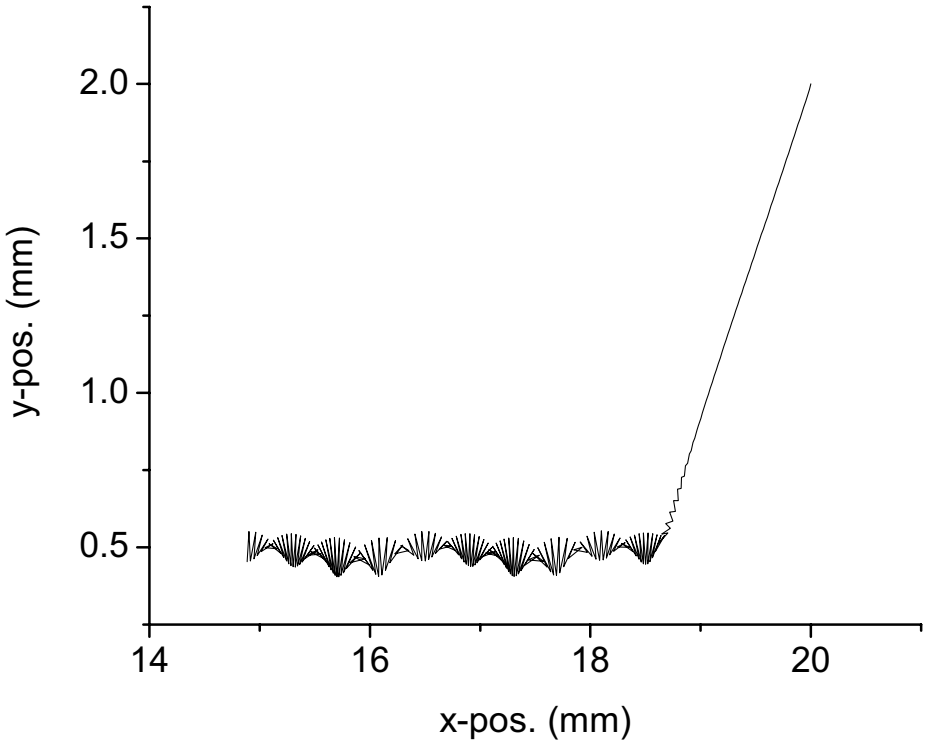

Figure 2.6: Ion trajectory from a simulation of an ion with $m = 85$ u starting at x = 20, y = 2 along a rf carpet with $a = 0.38$ mm and $g = 0.19$ mm run at 1.5 MHz at 200 $V_{RF,pk-pk}$ with a 10 V/cm push field and a 8 V/cm drag field at 100 mbar. The carpet would lie along the lower x-axis and the push electrode would be parallel but at y = 10 mm and are not shown. The trajectory output clearly shows the ion oscillating up and down due to the frequency of the applied rf (micromotion) and moving along the rf carpet (macromotion).

$$E_x = \frac{V}{\gamma a \pi}\left[\arctan\left(\frac{\cos\left(\pi[x_r - \frac{\gamma}{2}]\right)}{\sinh\left(\pi y_r\right)}\right) - \arctan\left(\frac{\cos\left(\pi[x_r + \frac{\gamma}{2}]\right)}{\sinh\left(\pi y_r\right)}\right)\right] \tag{2.10}$$

and

$$E_y = \frac{V}{2\gamma a \pi}\ln\left[\frac{\cosh\left(\pi y_r\right) + \sin\left(\pi\left[x_r + \frac{\gamma}{2}\right]\right)}{\cosh\left(\pi y_r\right) - \sin\left(\pi\left[x_r + \frac{\gamma}{2}\right]\right)} \cdot \frac{\cosh\left(\pi y_r\right) - \sin\left(\pi\left[x_r - \frac{\gamma}{2}\right]\right)}{\cosh\left(\pi y_r\right) + \sin\left(\pi\left[x_r - \frac{\gamma}{2}\right]\right)}\right] \tag{2.11}$$

where γ, x_r, and y_r are defined as:

$$\gamma = \frac{g}{a} \tag{2.12}$$

$$x_r = \frac{x}{a} \tag{2.13}$$

$$y_r = \frac{y}{a}. \tag{2.14}$$

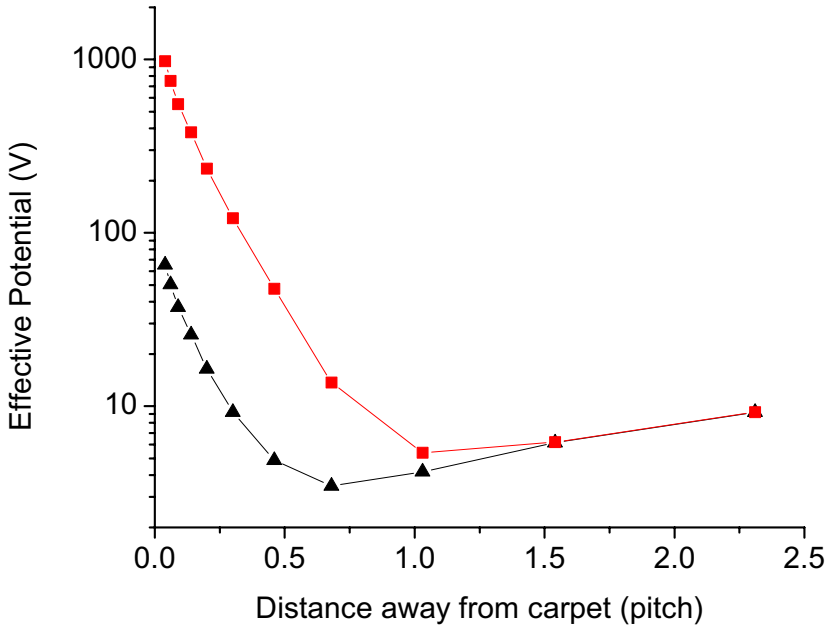

Figure 2.7: Calculated effective potential for a rf carpet (a = 0.5 mm and γ = 0.5) as a function of distance away from the carpet superimposed with the static potentials from an electric field perpendicular to the carpet electrodes (2 V/mm). For an ion with A = 85 amu ion at 2 MHz and a rf voltage of 200 $V_{RF,pk-pk}$ Black Curve: 100 mbar. Red Curve: 10 mbar.

The effective potential for a rf carpet with a = 0.5 mm and γ = 0.5 with a voltage setting of 200 $V_{RF,pk-pk}$ at 2 MHz for a mass of 85 amu is shown in Fig. 2.7 for two different pressures. An electric field with a strength of 2 V/mm in the direction perpendicular to the carpet electrodes, the push field, gives rise to the minima in the potentials.

2.6 Stability of ion motion over rf carpets

The parameters for stable ion motion along rf carpets can be found in a similar fashion to the parameters for stable ion motion in a quadrupole ion guide. The criteria for stable ion motion are stable ion trajectories along the length of the device that are not intercepted by an electrode. In the case of the quadrupole ion guide, arrival at these parameters starts with the equation of motion in the form of the Mathieu equation and ends in a final parameterized form of:

$$\frac{d^2u}{d\xi^2} + (a_u - 2q_u \cos 2\xi)u = 0 \tag{2.15}$$

where u represents the position and ξ, a_u, and q_u represent the dimensionless parameters:

$$\xi = \frac{\Omega t}{2} \quad , \quad a_u = \frac{8eU}{mr_0^2\Omega^2} \quad , \quad q_u = \frac{4eV}{mr_0^2\Omega^2}. \tag{2.16}$$

In Eqn. 2.16, U represents the applied dc voltage, V represents the applied zero-to-peak rf voltage, and the other variables have been previously defined. Stable ion motion in a quadrupole ion guide is dependent on the dimensionless parameters a and q and is represented by a region (the stability region) in the (q, a) plane.

For rf carpets specifically [17], the stability parameters are found by including two additional terms that include the damping of the micromotion due to the presence of gas [18], and the push field term. In the case of the rf carpet, the electric field in the y-dimension will determine if an ion's motion is unstable and the ion collides with an electrode. The resultant Mathieu equation for an rf carpet is now:

$$\frac{d^2y_\pi}{d\xi^2} = E_d \exp(-y_\pi)\cos(\xi) - E_{pr} - \kappa\frac{dy_\pi}{d\xi} \tag{2.17}$$

with the introduction of the term $y_\pi = y\pi/a$ and with now $\xi = \Omega t$. The parameters E_d, E_{pr}, and κ are:

$$E_d = \frac{q8V}{m\Omega^2\gamma a^2}\sin(\pi\frac{\gamma}{2}) \quad , \quad E_{pr} = \frac{q\pi E_p}{m\Omega^2 a} \quad , \quad \kappa = \frac{D}{\Omega}. \tag{2.18}$$

The stability region for stable ion motion over the rf carpet in the (E_{pr},E_d/κ) plane is shown in Fig. 2.8.

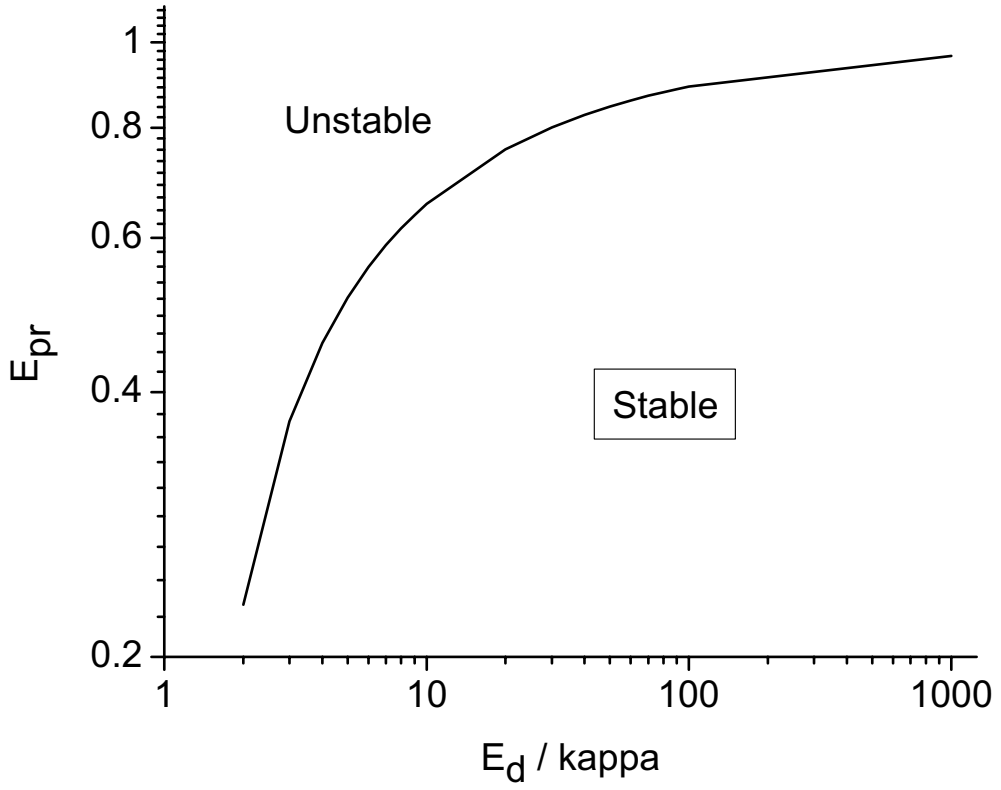

Figure 2.8: The region of ion motion stability over an rf carpet in the (E_{pr},E_d/κ) plane is represented by the area under the curve.

2.7 Rf carpet simulations

Simulations of the ion transport by rf carpets were performed in order to gain an understanding of the operating parameters for rf carpets. In addition, simulations served to confirm experimental results and also explore parameter spaces that could lead to a simplified op-

eration of the rf carpets. For a given simulation with a specific carpet electrode geometry, SIMION [19] was used to solve for the electric field and then to numerically integrate the equations of motion. This section will introduce the rf carpet simulations and cover the simulations preceding the experimental testing of rf carpets. The simulations compared to specific experimental setups will be covered in the experimental sections.

2.7.1 Rf carpet simulation basics

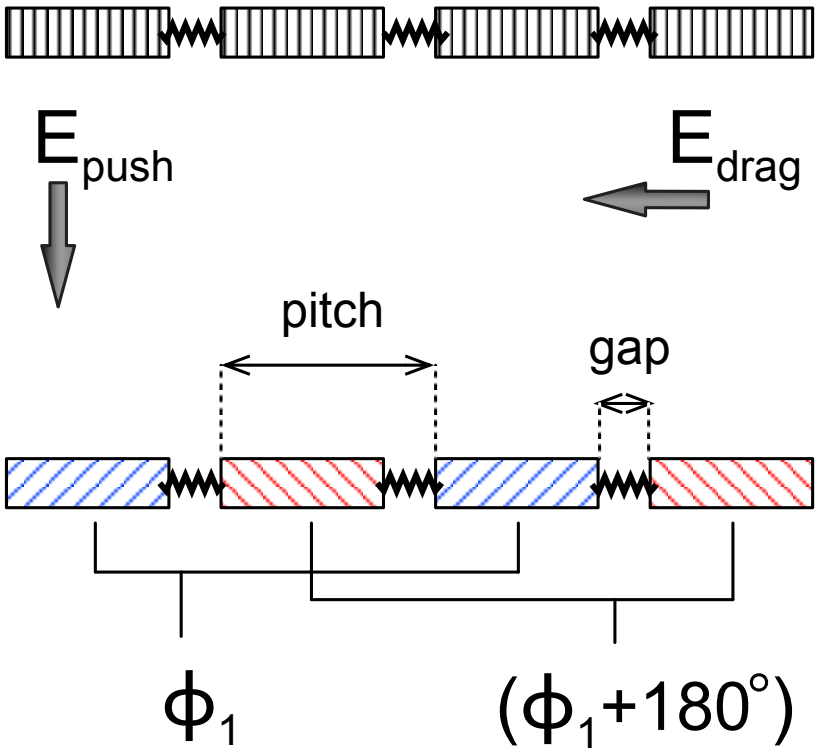

Figure 2.9: Conceptual schematic of the workbench setup used for ion transport simulations. The blue and red hatch patterns represent the two RF phases of the rf carpet separated by 180°. The push electrodes are represented by the vertical black lines. The direction of the push field and drag field are also shown.

Recall that the electrodes on a rf carpet have an applied rf voltage that is 180° out of phase with an adjacent electrode. In addition to this, the drag field is superimposed on the electrodes to establish a dc gradient to move the ions in the desired direction typically towards a collection electrode or extraction orifice. The push field, is established by another

set of electrodes to generate a constant electric field perpendicular to the effective repelling force provided by the carpet electrodes over the entire length of the carpet. A schematic layout of the electrodes is shown in Fig. 2.9.

The first rf carpet simulations were carried out to determine the maximum number of carpet electrodes that could be grouped at the same dc potential without significantly decreasing ion transmission. Grouping electrodes would significantly reduce the number of resistors and connections required to establish the drag field. Two sets of identical symmetric electrodes arranged in concentric circles one above the other served as the carpet electrodes and push electrodes, respectively. The ions were transported from the outer electrodes toward the inner electrodes. The electric drag field was superimposed on both the carpet and push electrodes to maintain a symmetric push field on the carpet electrodes. A view of the electrode geometry used in SIMION is shown in Fig. 2.10 and the parameters are given in Table 2.1.

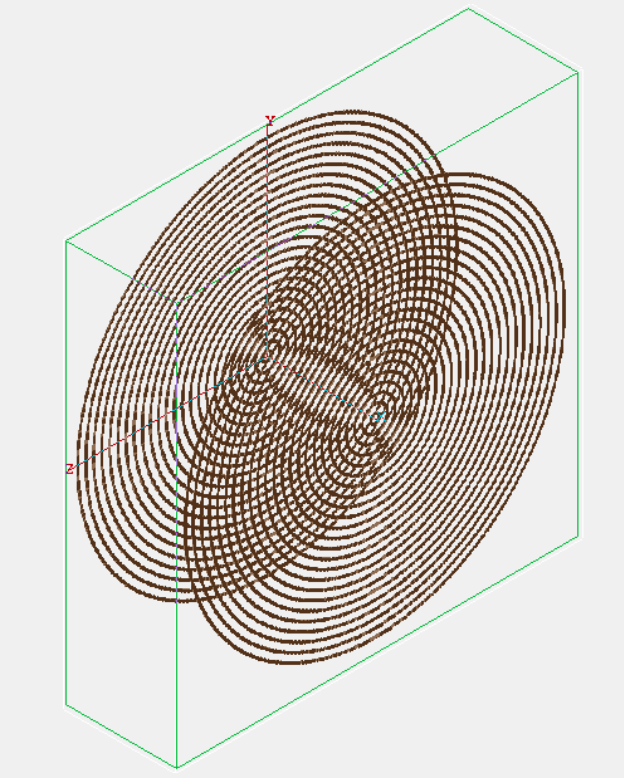

Figure 2.10: Simulation workbench for the rf carpet electrode grouping study. The two sets of electrodes corresponded to the carpet and push electrodes.

Through the use of fast scalable electrodes, only three voltages had to be adjusted to

Table 2.1: RF carpet electrode grouping simulation workbench parameters.

Parameter	Value
a	1.5 mm
g	1.05 mm
distance between carpet and push electrodes	20 mm
maximum transport length	35.55 mm
number of carpet electrodes	24

correctly apply all the voltages to the 48 electrodes in a given simulation called RF_amp, _DC_Drag, and _DC_Push. RF_amp was the rf amplitude in volts (0 to pk) applied to the carpet electrodes. It was configured to have the same magnitude but an alternating sign (+/-) for adjacent electrodes. _DC_Drag set the highest voltage for the outermost electrodes on both the carpet and push electrodes and decreased linearly to the innermost electrodes on both the carpet and push electrodes. _DC_Push set the additional uniform voltage on the push electrodes. Using the distances provided in Table 2.1, _DC_Drag and _DC_Push could be translated into the desired electric fields.

The transport efficiency was determined from the simulations by the following simple relation:

$$\epsilon = \frac{N_{trans}}{N_{total}} \tag{2.19}$$

where N_{trans} refers to the number of transported ions over a specified distance and N_{total} refers to the total number of ions started in the simulation. Criteria for N_{trans} was reaching a position specified by _Ymin from the ion's initial position without colliding with the electrodes and by the ion's time-of-flight not exceeding the time constraint specified by MaxTOF. _Ymin was selected such that the transport efficiency was calculated only over the transport length of the rf carpet and not the innermost electrodes near the center hole. This topic is discussed in later sections. MaxTOF was necessary to identify any rf carpet parameters that could lead to trapping potentials along the transport length.

The ions' initial parameters in the simulation were set to the expected properties of ions thermalized in He gas. A charge of +1e and an initial kinetic energy of 0.025 eV was

Table 2.2: Rf carpet electrode grouping simulation LUA user program variables.

Parameter	Description (units)
_f_MHZ	RF frequency (MHz)
RF_amp	RF amplitude (V) [see text]
_DC_Drag	Drag voltage (V) [see text]
_DC_Push	Push voltage (V) [see text]
_Ymin	Positional constraint in the y-dimension (mm) to stop simulation
Mobility	Reduced ion mobility (K_0)
P_mbar	Pressure (mbar)
MaxTOF	Time constraint in the ion's time-of-flight (μs) to stop simulation

used for an ion with a mass of 85 amu. The ions were generated four pitch units above the carpet electrodes and three pitch units inside of the outermost electrode to ensure that the ions drifted slowly towards the carpet electrodes and were not affected by the boundary conditions. The ions were also generated at 10 equally spaced time intervals over the period of the RF phase to ensure that the entire rf phase was sampled. A summary of the LUA user program variables are shown in Table 2.2.

To simulate the presence of a buffer gas, the implementation of Stokes' Law, or viscous drag force, to damp the ion trajectories was used. The drag force on a particle traveling in a viscous medium acts in a direction opposite and proportional to the velocity of the particle. Thus, the resultant acceleration, a_{tot}, is given by:

$$a_{tot} = a_{viscous} + a_{simulation} \tag{2.20}$$

where $a_{simulation}$ is the acceleration due to the instantaneous electric fields calculated by SIMION and $a_{viscous}$ is:

$$a_{viscous} = -c \cdot v \tag{2.21}$$

where c is the damping term. This damping term for the ion can be calculated from the reduced ion mobility and the buffer gas pressure, the adjustable parameters Mobility and P_mbar, respectively. The resultant acceleration is calculated according to Eq. 2.20 by applying a small correction factor suggested in the SIMION literature (see drag.lua) to increase

the speed and accuracy of the simulation.

2.7.2 Rf carpet electrode grouping simulations

For the 'electrode grouping' simulations, Φ_1 and Φ_2 maintained their 180° phase difference, but the number of adjacent electrodes that held at the same dc potential without degrading ion transmission was investigated. A group implies equal numbers of carpet electrodes from both phases. The dc-grouping was also applied to the push field electrodes. The effect of grouping on ion transmission, only required changing the electrode designation and mapping. Therefore, the physical characteristics of both the carpet and push electrodes did not change throughout this part of the study. The initial parameters of ions and the user program for each simulation workbench were also identical.

The initial simulations were conducted before any experimental work was conducted, and made some naive assumptions. However, since these simulations drove the initial rf carpet designs, it is important to present them. The parameters used in the simulations are shown in Table 2.3 and used the expected values for the voltages that could be applied to the electrodes.

The loss mechanism acting when having groups of adjacent electrodes on the same bias comes from the larger local potential drop experienced by the ion when it transitions between the potential steps. This can be seen in Fig. 2.11, where the ion trajectory with an electrode grouping of 4 comes much closer to the carpet electrodes than the ion trajectory with no electrode grouping also shown in Fig. 2.11. This effect can be reduced by decreasing the drag field, but this would slow the overall transport time proportionally to the reduction in the drag field. In addition, large groupings of electrodes would result in ions being confined (or trapped) along a single potential step and not being transported to the desired location.

From the simulation results, an electrode grouping of 4 electrodes (2 from each rf phase) did not differ strongly with regards to ion transmission efficiency. Thus, a grouping of 4 electrodes was implemented into the rf carpet design.

Rf carpet simulations that employed viscous damping were much faster in terms of

Table 2.3: Rf carpet electrode grouping simulation parameters.

Parameter	Value (units)
RF frequency	1 MHz
RF amplitude	(70 - 100) V
Pressure	100 mbar
Drag Field	10 V/cm
Push Field	10 V/cm
Mass of ion	85 amu
K_0	20 $cm^2/(V \cdot s)$
Transport length in y-dimension	2.4 cm
MaxTOF	10000 us
SIMION Trajectory Quality	10

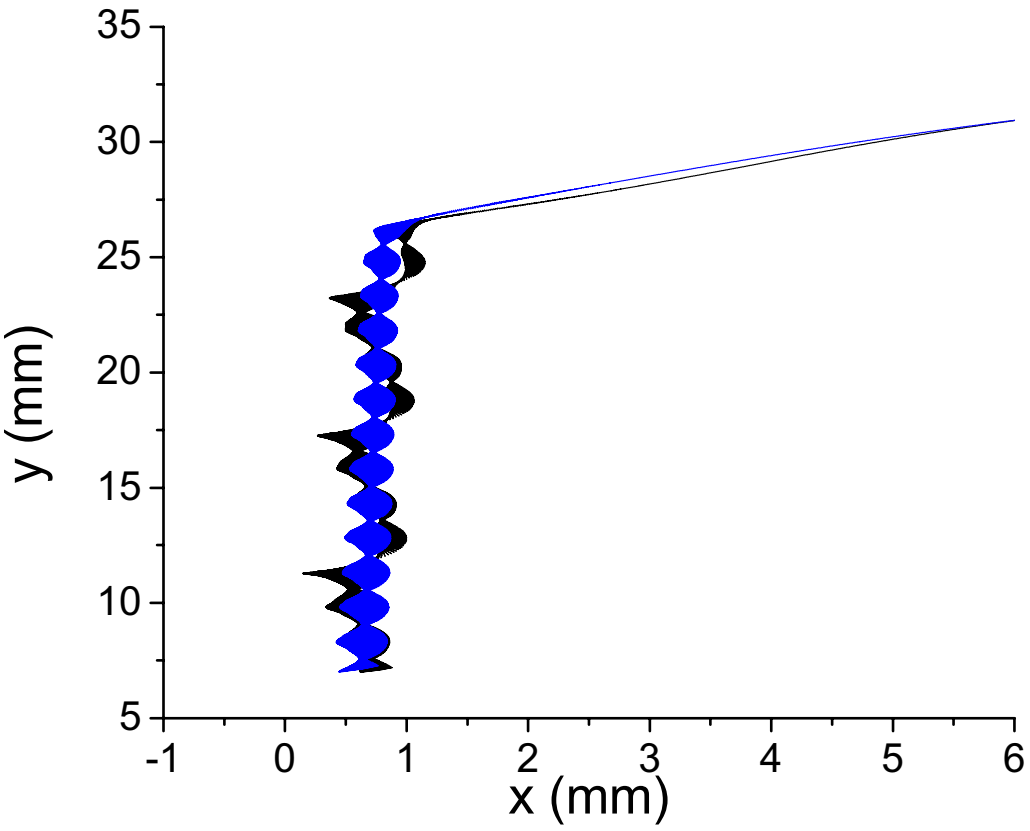

Figure 2.11: Trajectories from a rf carpet simulation with a=1.5, γ=0.7 with simulation parameters shown in Table 2.3. The carpet electrodes (not shown) are located at x=0 and the push electrodes (not shown) are located at x=20. Blue line: No electrode grouping. Black line: Electrode grouping of 4.

calculation time than those that employed Monte-Carlo collisions with hard-spheres (HS-collisions). However, this lack of microscopic detail later proved to be insufficient to explain experimental trends (as will be discussed in later sections). Even with that drawback, viscous damping still allowed for us to gain a general understanding of the ion motion along the rf carpet.

2.7.3 Hard-sphere (HS) collisions

Since the macroscopic viscous damping model was unable to reproduce the results observed in experiment, microscopic detail was added to the simulations in the form of collisions with the neutral background gas using a hard-sphere (HS) collision model. A SIMION user program, collision_hs1.lua, contains a complete hard-sphere collision model and could be called from within another user program (e.g. the main user program for the rf carpet simulations) to handle every ion-neutral gas collisional event.

A quality check of the collisional model was carried out by comparing the ion's average velocity with that of the velocity from the experimentally measured ion mobility in He. The adjustable parameter in the HS collisional model with the most impact on the ion's average velocity is the collision cross-section, which determines the frequency of collisions between the ion and the background gas. By default, the collision cross-section is the cross-sectional area with a diameter that corresponds to the sum of the diameters of the colliding particles. In collision_hs1.lua, this diameter was 17 angstroms that corresponds to the sum of the diameters of a He atom and a mass 200 amu ion. For this work, a collision cross-section for a He atom and a mass 85 amu ion needed to be determined. Rather than using a geometric cross-section, the collision cross-section that matched the average velocity given by ion mobility in He was found by creating a SIMION workbench that consisted of two parallel plate electrodes biased to generate a 10 V/cm electric field. A test ion was placed between the electrodes and migrated towards one plate in the presence of a He background gas. The simulation parameters are shown in Table 2.4 and collision cross-section of 2.75×10^{-19} m^2 matched the TOF according to the experimental ion mobility. The TOF distribution is shown

Table 2.4: HS collisions cross-section simulation determinations.

Parameter	Value (units)
Pressure	30, 60 torr
Electric Field	10 V/cm
Mass of ion	85 amu
K_0	20 $cm^2/(V \cdot s)$
Transport distance	1.0 cm

in Fig. 2.12. This cross-section results in a lower collision frequency as calculated from the geometric collision cross-section for a He atom and Rb ion (6.16×10^{19} m^2).

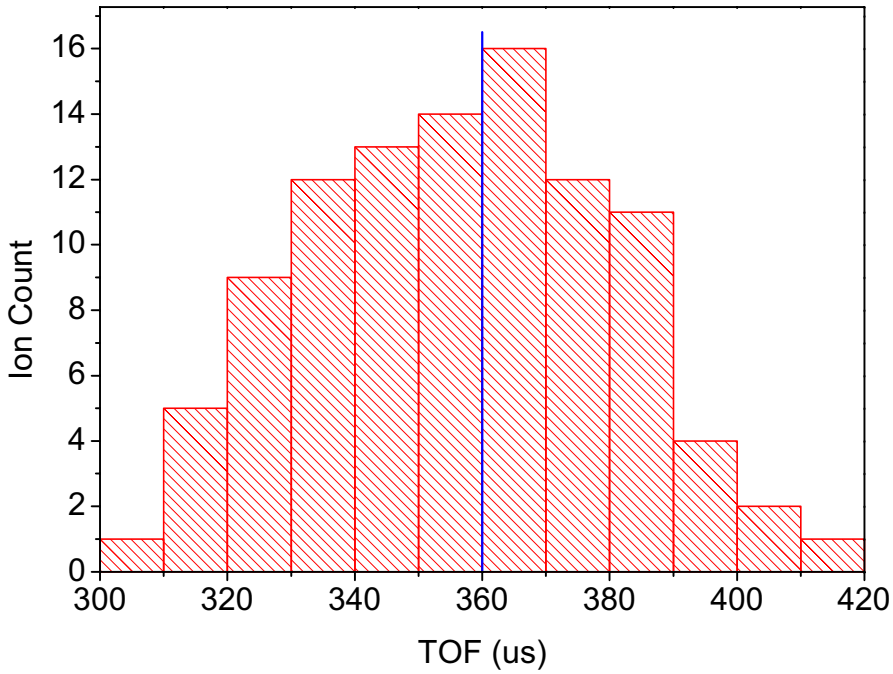

Figure 2.12: Histogram showing the TOF distribution of 100 ions with a collision cross-section of 2.75E-19$\times10^{-19}$ m^2. The blue vertical line refers to the TOF according to the ion mobility.

The HS collision model with the collision cross-section determined by the ion time of flight above was used throughout the rest of the simulations for comparison to the experimental results. It was more computationally intense to include HS collisions rather than the viscous damping approach, but the improved realism proved to be worth the additional calculation

time.

Chapter 3

Rf carpet transport

The primary focus of this dissertation project was to develop an ion transport device to be used in the transport of thermalized rare isotopes, and specifically in the cyclotron gas stopper. Thus, it was only natural for the bulk of the study to be comprised of ion transport measurements in the context of providing a future direction for the development of a transport device for rare isotopes.

3.1 The rf carpet test chamber

In order to test ion transport over distances approaching 50 cm, a chamber had to be built that would be large enough to house 50 cm rf carpet electrodes, all the necessary feedthroughs for the application of the necessary voltages, the ion source to generate the ions, and the diagnostic tools for pressure readings and ion current collection. The design of the test chamber was influenced by the geometrical arrangement of the rf carpets in the cyclotron gas stopper. A modular design for the test stand was chosen to provide a device to allow varying size, shape, and method of application of voltages.

The rf carpet test chamber that was constructed for this project is 1.2 m in diameter with a 45 cm depth and is shown in Fig. 3.1. Three support legs are mounted to the floor by bolting fixtures to increase physical stability when the chamber door is opened. In total,

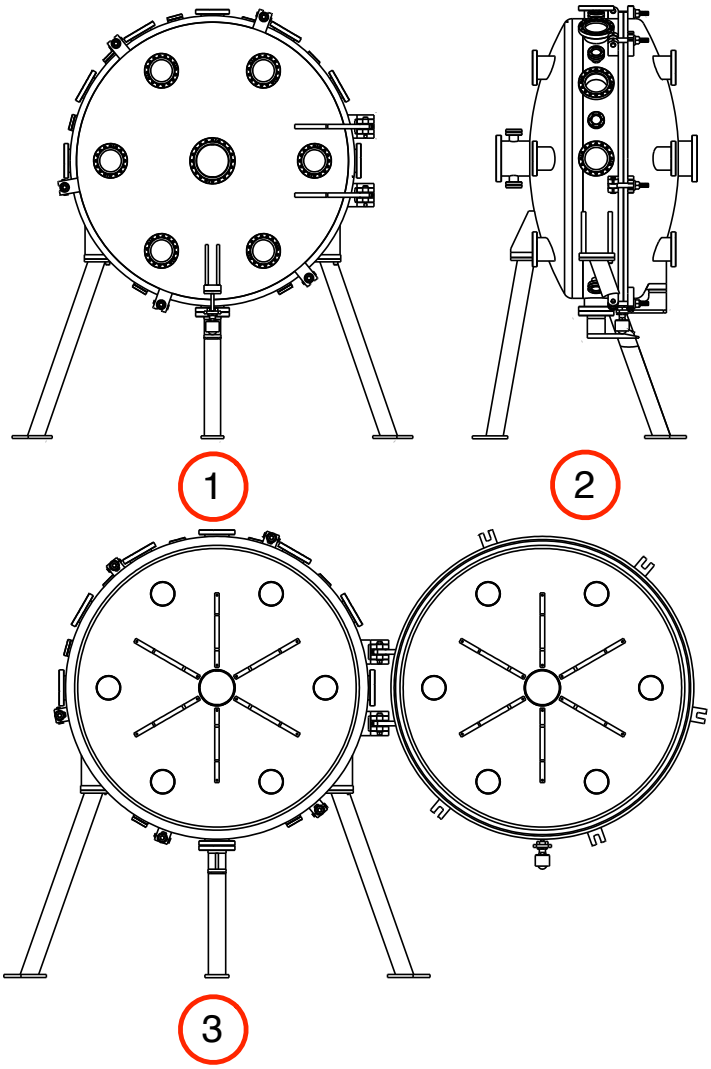

Figure 3.1: Mechanical drawing of the rf carpet test stand used for ion transport (1) Front view of closed test stand. (2) Side view of closed test stand. (3) Front view of open test stand. The inner diameter of the chamber is 1.2 m.

there are 19 x 6", 9 x 2.75", and 2 x 8" conflat flanges on the chamber. Along the door, there are 6 x 6" and 1 x 8" conflat flanges primarily used for viewports and feed-throughs for the push electrodes. Arranged along the edge of the chamber, are 7 x 2.75" and 7 x 6" conflat flanges used for mounting the turbomolecular pump, pressure diagnostic tools (cold cathode gauge, pirani gauge), current measurement feedthroughs, dc voltage feedthroughs, and the gas inlet for the high-purity He gas (99.999%). The backside of the chamber has exactly the same flange arrangement as the chamber door, except that there are 2 x 2.75" conflat flanges, one of which was used for the flexible hosing for the roughing line. The central 8" conflat flange on the backside of the chamber was used to mount a special 2 x 2.75" adapter to input the two phases of the rf. The remaining 6" conflat flanges were used as viewports and to house the rotary feedthrough for the ion source. Due to the various carpet electrodes studied in the chamber, the exact purpose of each flange assignment changed very often.

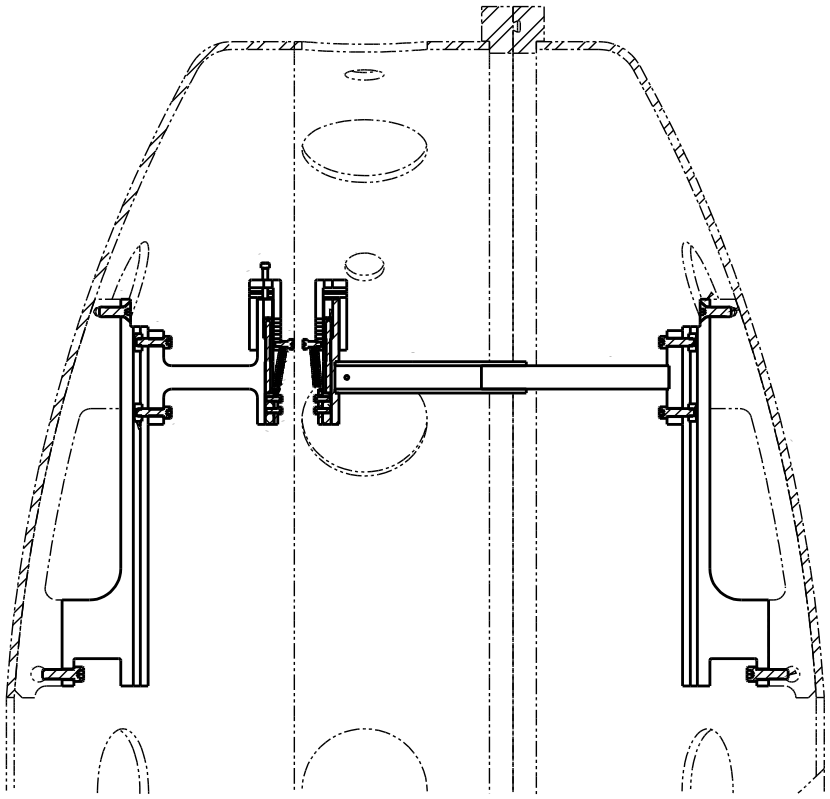

Figure 3.2: Mechanical drawing of the rf carpet test stand and the original carpet and push electrode supports. The (dot-dot-dash) lines show the rf carpet test stand and the (solid) lines show the carpet and push electrode supports.

A symmetrical set of slide holders in which support bars can be mounted to hold the carpet electrodes and the push electrodes. On the inside of the chamber and the innerside of the chamber door as can be seen in (3) of Fig. 3.1. The symmetry of the holders allowed the easy alignment of the carpet and push electrodes by matching the positions of the supports on each slide holder and on its mirrored partner. In addition, the supports could be adjusted to change the distance between the carpet and the push electrodes. Unfortunately, the practical size of the ion source body and arm did not allow for its height to be adjusted. Since the carpet and push electrodes themselves were typically on the order of 1 - 2 mils and made of flexible pcb material, the clamping method shown in Fig. 3.2 was used for several of the first rf carpet prototypes. This clamping method was limited to only six contact points per

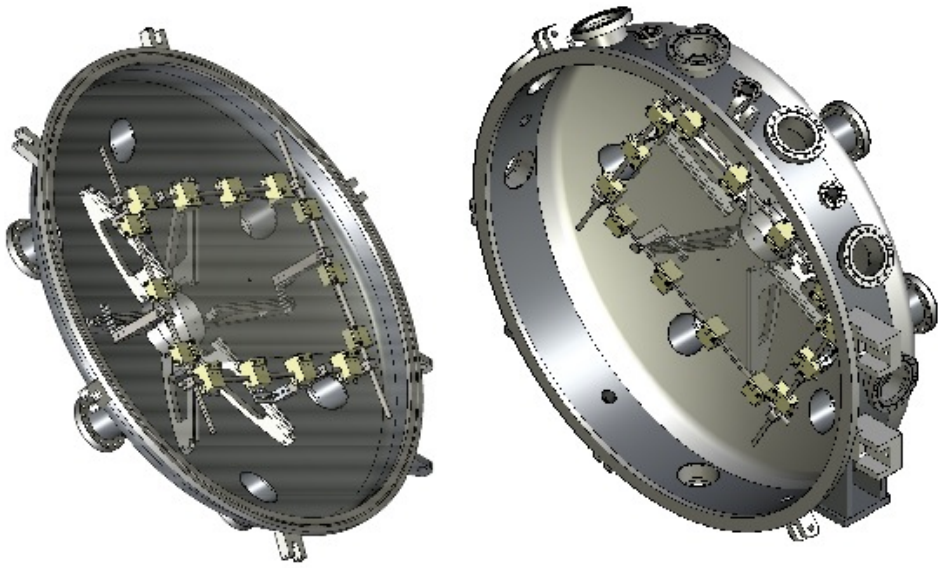

Figure 3.3: Mechanical drawing of the clamping method that allowed for easier modification of the carpet electrodes without having to redo the clamping process. The carpet electrodes are represented by the opaque grey rectangular sheets. Left: Frame on the door side. Right: Frame on the chamber side.

electrode and that each clamp only had 0.9 cm^2 of surface contact with the flex pcb material. This resulted in surface non-uniformities in the electrode surface and especially in close proximity of the clamps. Another difficulty with this clamping method was that any repairs that needed to be done to the carpet electrodes required all the connections for applying

the voltages and current collection to be disconnected and the entire electrode system to be unclamped from the individual clamps. Since special care was taken to establish a uniform surface on the electrodes, this process could take several hours depending on the particular set of electrodes. Electrical discharges occurred frequently between the stainless steel clamp held at the same electrical potential as the test chamber (ground) and the biased carpet and push electrodes. A stand-alone clamping system (a frame) that kept the carpet electrodes clamped with insulators when dismounted from the test stand was developed in order to make the connections easier to the carpet electrodes, anchor points could be established on the clamping frame that retained the connection to the electrodes and allow for connectivity to the feedthroughs. A photograph of a carpet held with this improved clamping method

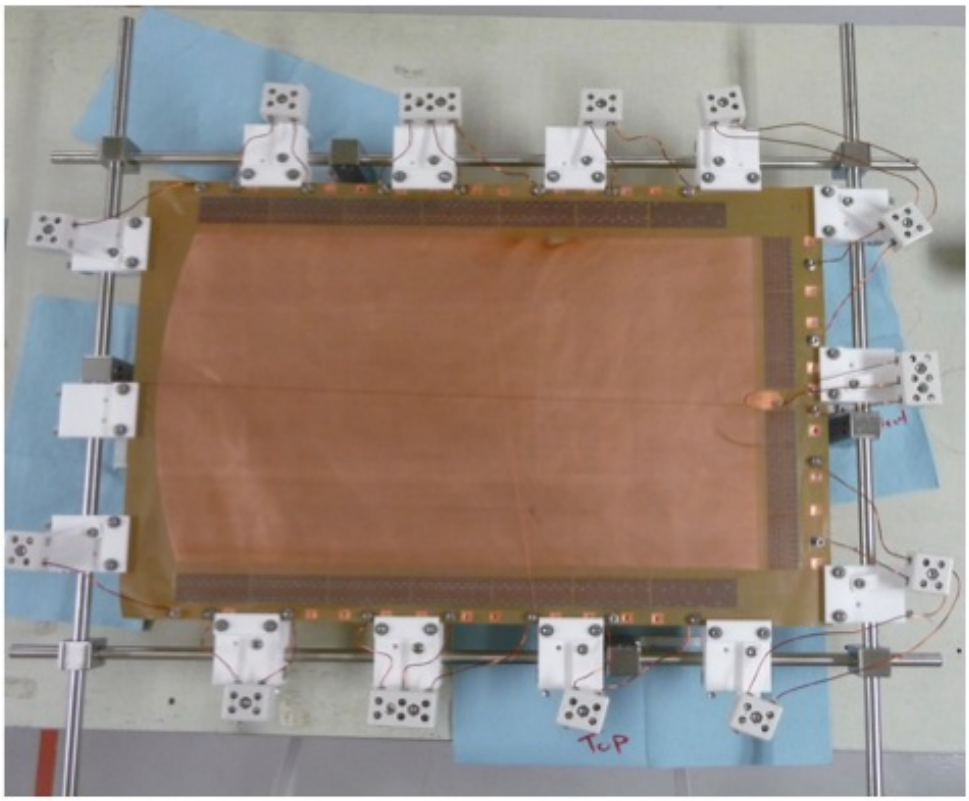

Figure 3.4: 50 cm carpet mounted in a frame. The electrical connections between the carpet electrodes and the ceramic terminal blocks are visible.

is shown in Fig. 3.3. The electrodes are clamped by Teflon blocks (white) which served to minimize discharges between the frame and the electrodes. Ceramic terminal blocks (gray) attached to the frame were used to connect the carpet electrodes to the feedthroughs on the

Table 3.1: Pressure readout for rf carpet test chamber and roughing line.

Device	Location	Pressure Observed (units)
Pirani Gauge 1	Roughing Line	1×10^{-3} mbar to 5 mbar
Pirani Gauge 2	Chamber	1×10^{-3} mbar to 5 mbar
Cold Cathode Ion Gauge	Chamber	1×10^{-5} mbar to 1×10^{-8} mbar
Baratron Gauge	Chamber	5 torr to 760 torr

chamber. Thus, if the carpet needed to be removed from the chamber, only the connections at the terminal blocks and the bolts fastening the frame to the slide holders had to be removed.

The chamber was pumped down by a Oerlikon Leybold TW 290H turbomolecular (turbo) pump backed by a Varian Triscroll 300 mechanical scroll pump. The pressure gauges included two MKS convection pirani gauges, a MKS cold cathode ion gauge, and a MKS absolute baratron gauge. A MKS 937A controller was used to readout the pressure from the two pirani gauges and the cold cathode ion gauge. A MKS 250E pressure/flow controller was used to readout the baratron gauge. Table 3.1 shows the pressure gauges, their locations, and the associated pressure observed in the system. A gate valve was used to isolate the test chamber from the turbo pump during ion transport measurements when the test chamber was held at a static pressure. The gas flow into the chamber was controlled by a MKS 250E flow controller and a MKS 148J 30000 SCCM solenoid valve. The flow option on the 250E flow controller was not used since the chamber was generally held at static pressure for these studies and did not need to maintain a constant flow rate. Each time the chamber was opened, the chamber was purged three times and then pumped down with the turbomolecular pump. A purge cycle consisted of pumping down the chamber to $\sim 8\times10^{-2}$ mbar with the scroll pump and filling the chamber with ∼5 mbar of He gas. This volume was then pumped back down to $\sim 8\times10^{-2}$ mbar. The complete process was considered one complete purge. The purging process had a significant positive effect on the pump out time of the chamber, resulting in a $\sim 1\times10^{-7}$ mbar base pressure after 16 - 24 hours as opposed to a $\sim 1\times10^{-6}$ mbar base pressure over the same time frame without purging. The pressure inside the chamber during pump down was recorded to check for leaks after any modification to the flanges occurred.

These pump out rates were in good agreement with each other between modifications as can be seen by three examples in Fig. 3.5. Since the chamber was held at static pressures, the

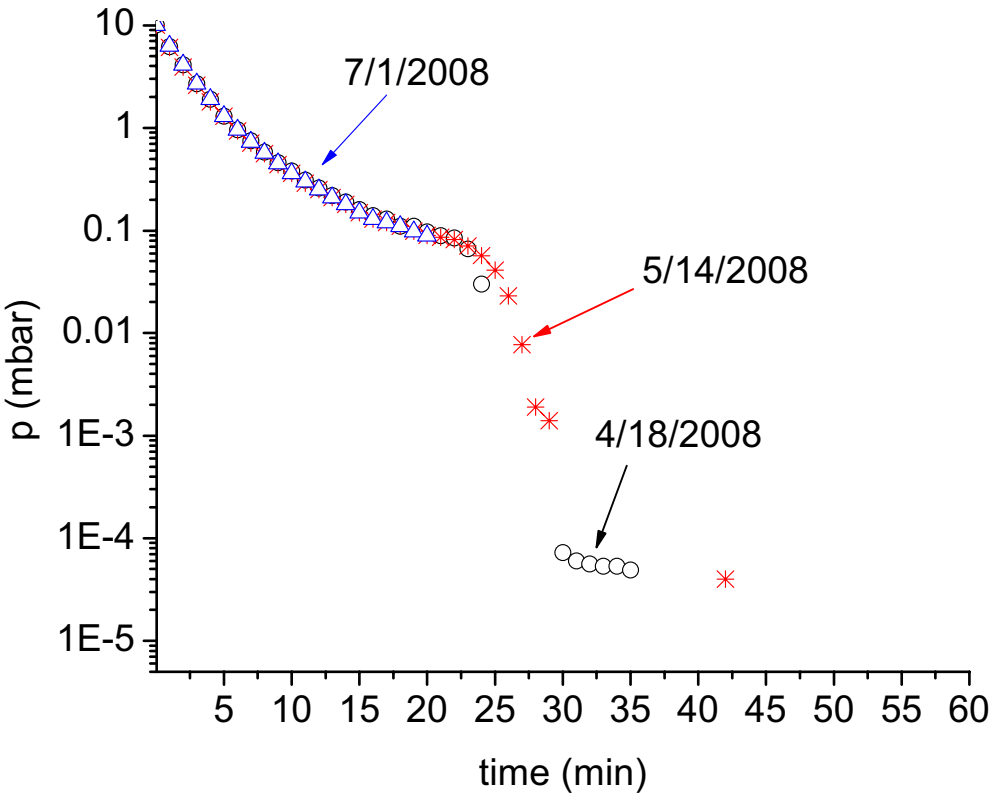

Figure 3.5: Pressure reading inside the chamber during pump out after the chamber was opened and modified on three different dates. Black circles: 4/18/2008, Red stars: 5/14/2008, Blue Triangles: 7/1/2008. Blue triangles overlap black circles and red stars. The TMP was started at ∼22 minutes.

partial pressure of contaminants for a given transport study could be estimated. Closing off the chamber after pumping for 12 - 24 hours and observing the pressure rise in the chamber typically resulted in a pressure rise of 6.3×10^{-9} mbar/s. Approximating the time spent for a transport study at one particular pressure to be 60 minutes with at an average chamber pressure of 100 mbar, the partial pressure of contaminants would be 0.2 ppm. There would be more contaminants in the He gas (99.999%) than from the equipment inside the chamber!

3.2 Alkali ion source characteristics

The ion source used throughout the transport tests was an alkali aluminosilicate ion source from Heatwave Labs (Model 101139). For this study, a Rb ion source was primarily used. The source operates on the principle of thermionic emission of the alkali ions from an aluminosilicate ion emitter material. A schematic diagram of the ion source obtained from the manufacturer is shown in Fig. 3.6. A table of the operating parameters in vacuum can be found in Table 3.2. The ion source for the ion transport tests had to operate in the presence of helium gas, whereas the intended operation of these ion sources is in vacuum. Thus, the required heater current to produce an ion current leaving the source on the order of nA was approximately 3 A in the presence of the He gas. Thus, the operation of these ion sources differed from the standard operating procedure as suggested in the literature.

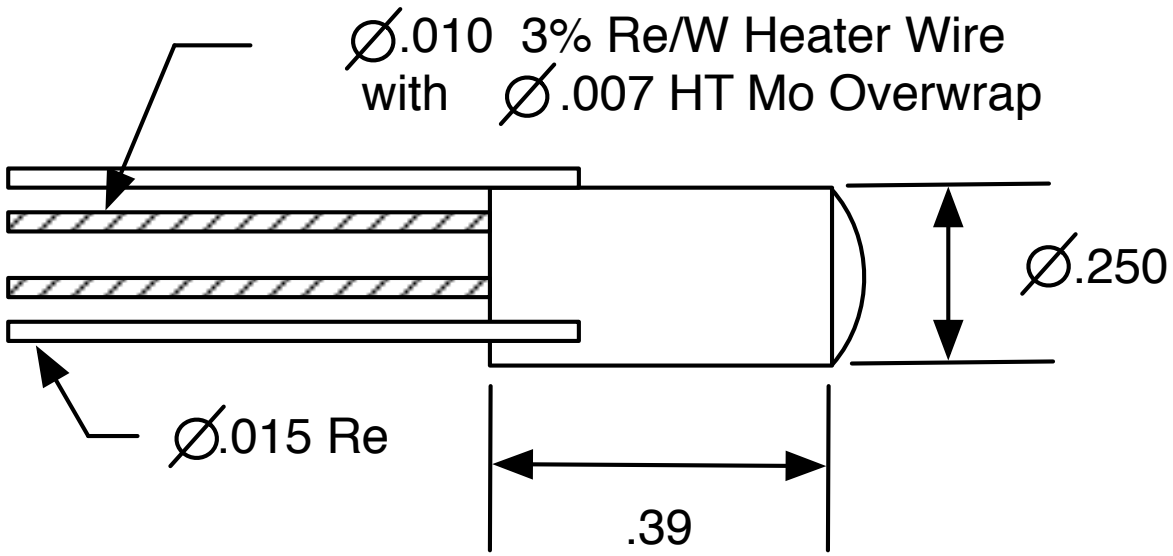

Figure 3.6: Dimensions for the ion source given in inches.

In order to perform the ion transport measurements, the physical position of the ion source had to move, the ions needed to be able to reach the carpet, and a method of measuring the current leaving the source had to be developed. Moving the ion source to different positions was accomplished by placing the ion source on an arm attached to a rotary

feedthrough with a control knob with an integrated position indicator on the outside. This allowed the ion source to be moved to the exact same location (different transport distances) when the chamber was closed. In order for the ions to reach the carpet electrodes reliably, simulations were conducted to design an electrode system that would provide the best focusing for ions to reach the carpet. A simulation of the ion motion for the two electrode system that was adapted into the final design (exact dimensions) for the ion source housing is shown in Fig. 3.7.

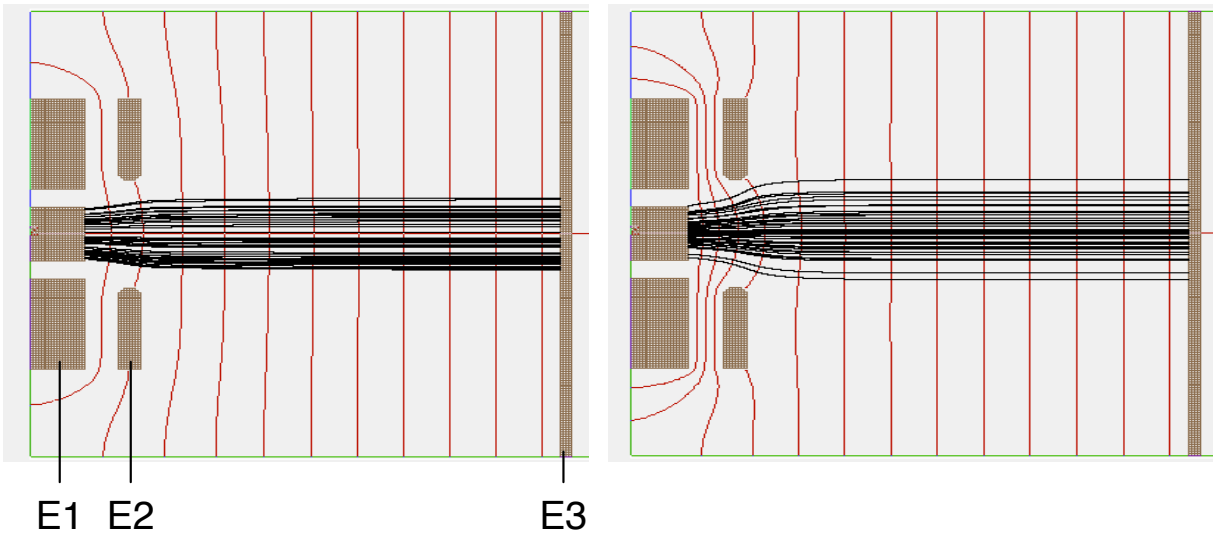

Figure 3.7: Results of simulations of the two electrode system for the ion source using the SIMION code. Both cases were for a pressure of 100 mbar using viscous damping. Equipotential lines shown in red. Ion trajectories shown in black. E1 (electrode 1) is the ion source body and the electrode surrounding it at the same potential. E2 (electrode 2) is the lens in front of the ion source that eventually became the entire ion source housing. E3 (electrode 3) is a collection plate. Left: E1 = 90 V, E2 = 80 V, E3 = 33 V. Right: E1 = 100 V, E2 = 80 V, E3 = 33V.

The final design of the ion source housing allowed the mounting and biasing of the ion source at a separate potential from the rest of the housing. It also incorporated a support for the leads for the heater current.

Measuring the ion current reaching the carpet electrodes was important for this study because it provided the basis for determining the transport efficiency. Transport efficiency was determined by the ratio of the ion current on the collection electrode to the total ion current

Table 3.2: Operating parameters for the Heatwave Labs (Model 101139) ion source in vacuum.

Parameter	Value
Temperature	900 - 1200°C
Voltage	6.3 V
Current	1.8 A @ 1100°C

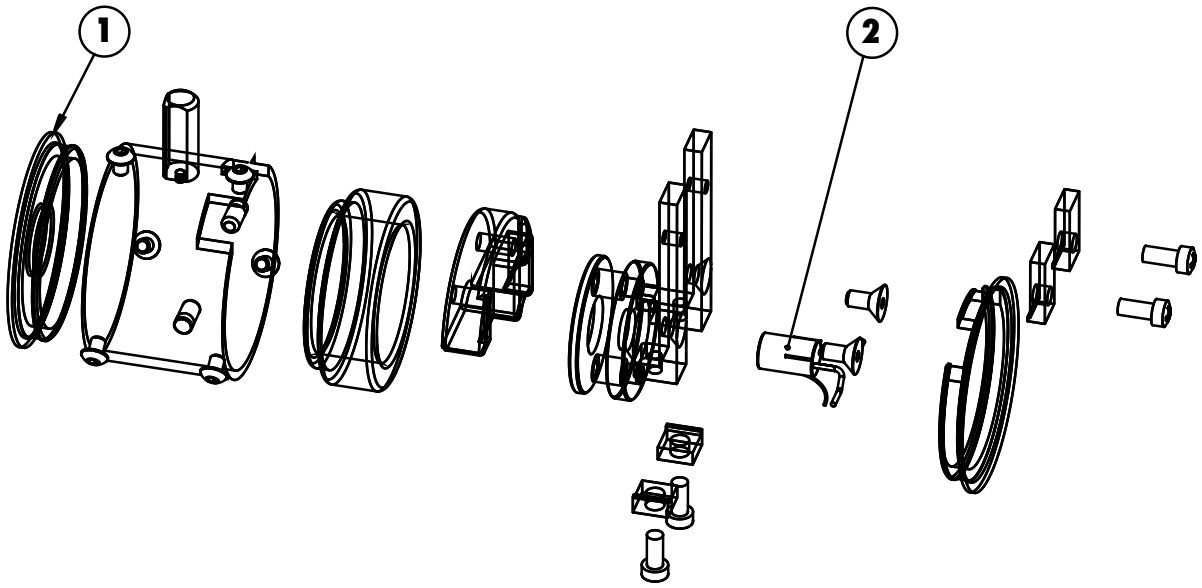

Figure 3.8: Exploded view of ion source housing. 1) Lens face of the ion source housing (electrode #2 in Fig. 3.7). 2) Ion source (electrode #1 in Fig. 3.7). The ions exit to the left from the lens (1).

interacting with the carpet electrodes. Initially, the only information on the ion current leaving the ion source was the current observed on a collection plate located somewhat away from the carpet electrodes. This was regarded as the total ion current from the ion source. However, when ion transport efficiencies greater than 100% were observed on the rf carpet, this simple method of determining the ion source output had to be rejected. The ion source total output was found to be sensitive to not only the heater current, but also the extraction voltage. If the electric fields at the lens when it was near the collection plate were not identical to those experienced over the carpet electrodes, different ion source currents leaving the source would be produced at the carpet electrodes and at the collection plate. Numerous attempts were made to mimic the electric fields that the ion source experienced over the carpet electrodes at the collection plate, but this resulted in cooling/heating effects in

the ion source and still rendered efficiency determinations to be difficult with this technique.

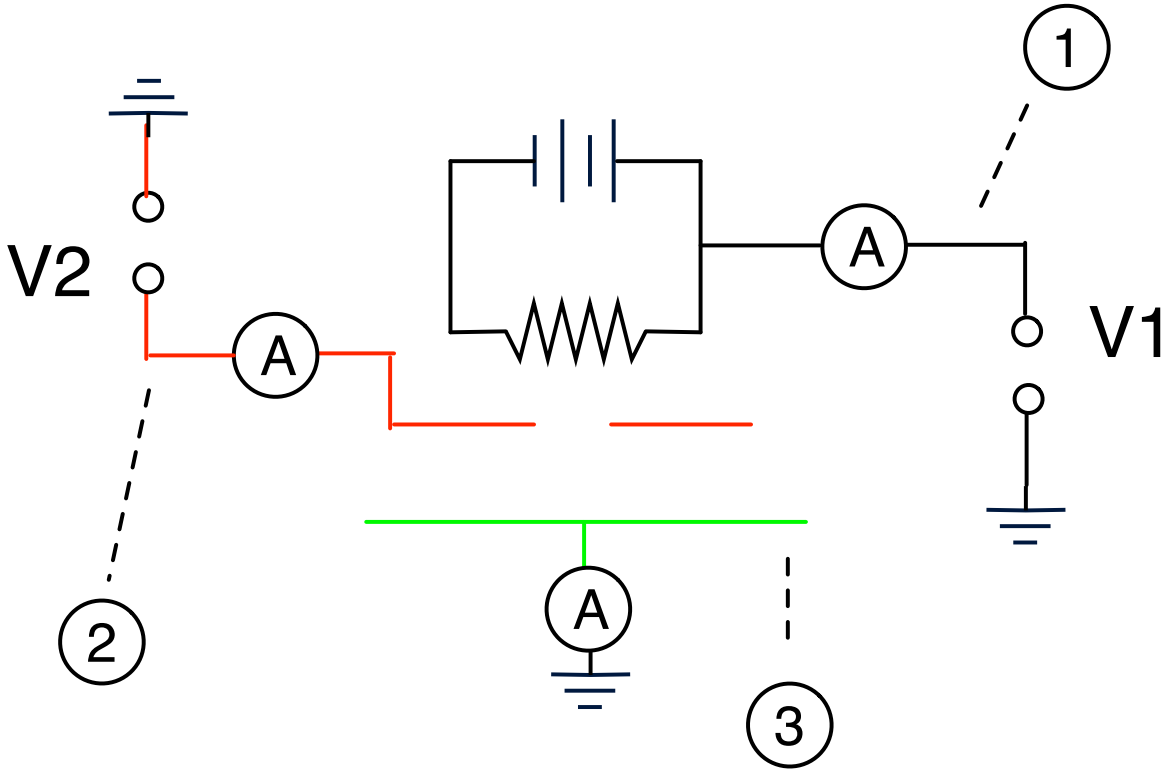

Figure 3.9: Schematic circuit diagram of the revised current measurement setup that allowed measurement of the ion current leaving the ion source, the ion current reaching the ion source housing, and the ion current reaching the collection plate. Label (1), Black: Ion source. Label (2), Red: Ion source housing. Label (3), Green: Collection plate.

A new configuration was developed to give the greatest amount of dynamic control involving measurement of the total ion current leaving the ion source [$I(IS)$] and any ion current impinging on the ion source housing [$I(Lens)$]. Then, [$I(IS)$] - [$I(Lens)$] = [$I(Collect)$], where [$I(Collect)$] is the ion current impinging on the collection plate / carpet electrodes. From these measurements, a transport efficiency is determined and is discussed in detail in section 3.6 (Calibration measurements). A rechargeable car battery was used to provide low-noise power to heat the ion source.

3.3 Rf carpet design

3.3.1 Material requirements

The requirements on the printed circuit board (pcb) material for the rf carpets include a low outgassing rate, good signal transmission, and robust thermal properties. The low outgassing rate is required because impurity ions can charge exchange with the He buffer gas ions created during the slowing down process and can be extracted out of the stopping chamber. Good signal transmission, or low signal attenuation, is important to make sure that the applied rf signal was constant over the length of an electrode stripe over the desired frequency range. Robust thermal properties are important because surface mount devices must be soldered onto the flex circuit without degrading the material or delaminating the Cu.

To fulfill these requirements, Kapton, a polyimide film that is commonly used as an insulator in UHV environments was chosen as the substrate for the rf carpets. In addition, a Kapton based adhesive can be used to adhere the Cu to the Kapton substrate avoiding the use of epoxy adhesives. An all-polyimide laminate available from Dupont (Pyralux AP) was chosen to be the specific Cu-clad laminate because it fulfilled the material requirement, had a low signal attenuation up to the GHz frequencies, and passed thermal stress tests for soldering without any delamination of the Cu. The flexible nature of the laminates has given the resultant printed circuit boards the name of 'flexible pcb' or 'flex pcb'.

3.3.2 Typical flex pcb manufacturing constraints

Once the substrate material was chosen, a set of pcb manufacturers had to be found that could do low-volume (prototype) work and be technically proficient enough to manufacture large size pcbs with a consistent Cu trace and gap size on the sub-mm level over the entire area. The typical manufacturing limit with regards to size is a maximum panel area of 45 cm x 60 cm and minimum trace and gap width of 0.125 mm. The flex pcb manufacturers that were used for this project were Innovative Circuits, Gigatek Inc., and Stevenage Circuits.

3.3.3 General design elements of RF carpets for ion transport

Taking into account the manufacturing constraints mentioned in the previous section for flex pcb manufacturing, early rf carpet prototypes used for ion transport required four main design elements:

1. The transport area
2. The collection area
3. Rf & dc contacts
4. Clamping area for physical support

An example of a prototype rf carpet with these general design elements for all RF carpets (arranged in a linear fashion) for ion transport is shown in Fig. 3.10.

The transport area, as its namesake suggests, is the area of the carpet electrodes responsible for transporting the ions. It generally consisted of a repeating electrode and gap structure with a uniform spacing over the desired transport area. Due to the minimum areas required for the other three design elements, the active area of the rf carpet was typically 40 cm x 50 cm or less.

The collection area contained an electrode array adjacent to the transport area that could be biased and connected to an electrometer to measure the ion current. In the carpet design with linear stripes, such as in Fig. 3.10, the collection area was segmented in order to observe the distribution in the transverse direction of ions transported along the surface. For carpet designs consisting of semi-circle stripes, the collection area was the innermost semicircular electrode.

In order to apply the appropriate RF & DC voltages, a portion of the circuit board was reserved to make the necessary connections to the carpet electrodes. The contacts had various shapes depending on the nature of the connection method. An early connection method used a clamping mechanism constructed of Teflon bars with the individual wires from the 9-pin feedthroughs woven through the Teflon bars. The connection area shown

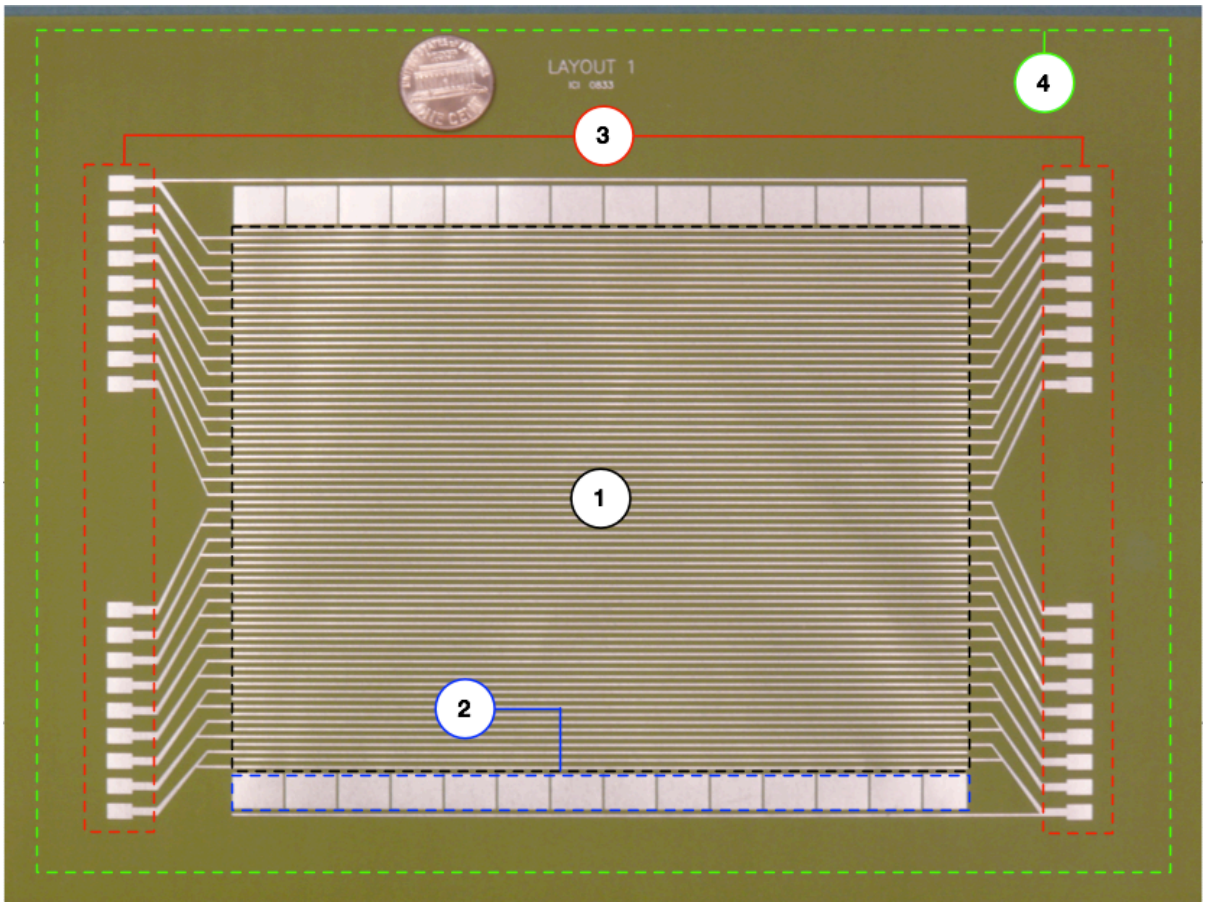

Figure 3.10: A linear carpet design with straight (linear) stripes for the transport area. The different design elements are designated by the numbered areas that are outlined outlined by the colored dashed lines. (1) Dashed black line: transport area; (2) Dashed blue line: segmented ion collection area; (3) Dashed red line: Rf & dc contacts; (4) Dashed green line: clamping area - Kapton (substrate) border. The coin, included for scale, is a US penny.

in Fig. 3.10 is representative of the electrodes used for this clamping method. Connection methods were simplified in later designs to be a square pad with sufficient surface area for a hole that allowed a bolt to secure an individual wire to make a good electrical contact.

The clamping area refers to the available material of the substrate (Kapton) around the border of the pcb by which the flex pcb could be fastened and mounted inside the vacuum chamber. Typically 1 cm between the pcb of the board and any Cu traces was provided for clamping.

Figure 3.11: Photograph of a large rf carpet with a 48 cm transport distance and a pitch of 0.38 mm. The collection electrode (center bottom of the transport area) has a diameter of 1.8 cm.

Over the course of the present work, the transport area electrode shapes evolved from initially parallel linear stripes to semi-circular stripes. The semi-circle rf carpets had the feature that they also guided the ions in towards the central electrode in a manner necessary for the

final operation of rf carpets in the cyclotron gas stopper. However, given the manufacturing limit of the maximum area, a design consisting of purely semi-circles would only have a maximum transport distance of 20 cm. In order to take advantage of the maximum area for one Kapton panel and extend the transport distance as far as possible, a semi-circle design continued by a series of arcs allowed a maximum transport length of 48 cm. A photograph of an example of such an rf carpet is shown in Fig. 3.11.

Later designs which moved the resistors onto the flex pcb in order to establish the drag field. These pcb's required an additional element that provided pads designated for specific surface mount resistors. In addition to the resistor pads, the routing to the appropriate electrode had to be present. The pads had to have enough space in between each resistor for soldering, as well as leaving most of the area of the flex PCB devoted to the transport of ions. A photograph of surface mount resistors mounted on the rf carpet that satisfied these requirements is shown in Fig. 3.12.

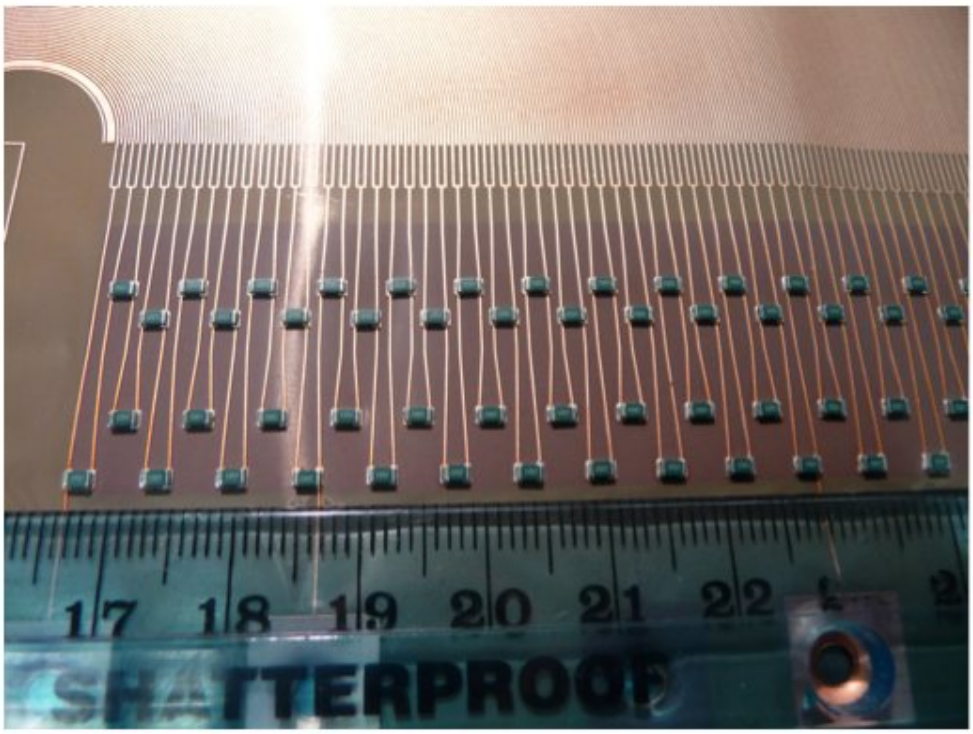

Figure 3.12: Photograph of surface mount resistors mounted on an rf carpet with a centimeter scale for reference.

3.4 Applying rf & dc voltages on the rf carpet

Rf carpets require a combination of rf and dc voltages to operate. This section will first cover the methods used in this study to generate and apply the appropriate rf voltages for the rf carpet, and then the dc voltages for the rf carpet. Lastly, the unique method used to combine the rf and dc voltages and apply them to the rf carpets is presented.

3.4.1 Rf voltages for the rf carpet

The rf voltage for the rf carpet was generated using resonant LC circuits [20]. In this approach, L, the inductor, and C, the capacitor are connected in series to an AC power supply. Depending on the applied signal frequency, the inductive reactance X_L and the capacitive reactance X_C cancel at the resonant frequency, f_r, in units of Hz given by the expression:

$$f_r = \frac{1}{2\pi\sqrt{LC}} \tag{3.1}$$

where L is given in henries and C is given in farads. At the resonant frequency, the only resistance to current flow comes from the resistive losses encountered with the wires in the circuit. These minimal resistive losses allow for minimal power consumption while providing a maximum rf amplitude. This is the major advantage of using resonant LC circuits to provide the rf voltage for the rf carpets.

An Agilent 33120A arbitrary waveform generator (AFG) and a T&C Power Inc. AG series amplifier were used to supply the sinusoidal waveform up to 10 MHz. The AG series amplifier also indicates the reflected power in the circuit and was useful for tuning the circuit to the resonant frequency (taken to be the point at which the amplifier indicated there was no reflected power in the circuit). A ferrite core transformer was used to match the 50Ω output impedance of the amplifier to the impedance of the load. The capacitance of the circuit is dominated by that of the rf carpet. Since the carpet electrodes consists of very many Cu strips sandwiching a dielectric, the carpet electrodes provide a very large capacitive load depending on the size and pitch of the electrode setup. Air-core coil inductors

provided the inductance and were changed as necessary to obtain the desired rf operating frequency. Variable capacitors (15 - 150 pF) were added to the LC circuit in order to match the amplitude of the separate rf phases. A schematic design of the rf circuit is shown in Fig. 3.13.

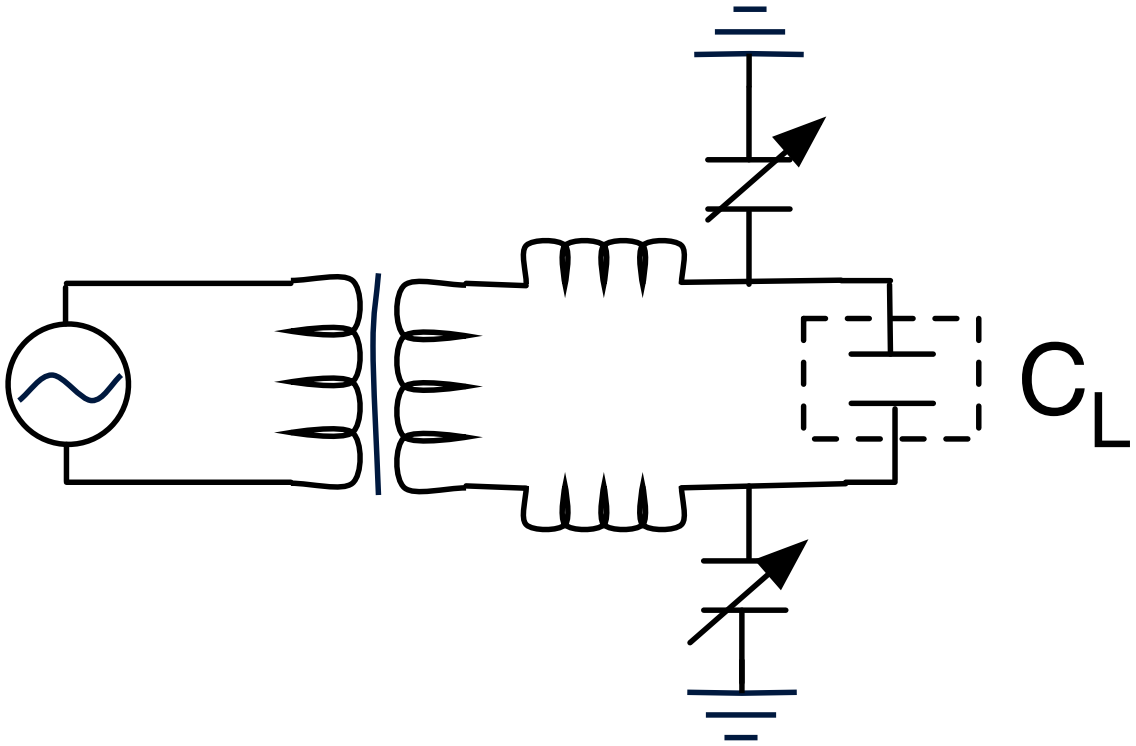

Figure 3.13: Schematic diagram of the LC circuit used to generate the rf voltages for the rf carpet. C_L is the capacitive load determined by the rf carpet. Typical ranges for the components: Variable Capacitors = 15 - 150 pF, Air-core inductors = 3 - 10 μH, C_L = 700 pF - 10 nF.

The disadvantage of using a resonant LC circuit is that the resonant driving frequency depends on the capacitance and the inductance of the individual circuit. Over all of the rf carpet prototypes, the total capacitive load of the system was found to lie in the range of 30 pF to 11 nF. For a desired rf operating frequency in the range of 1 to 3 MHz with a capacitive load of 5 nF requires an inductance of 5 μH to 0.5 μH respectively. At the 5 μH level, the inductance can be introduced in the circuit by using the air core coil inductors

mentioned in the previous paragraph. However, at the 0.5 μH level, the stray inductances of all components begin to be important and keeping the inductance at or below this value becomes difficult.

A method to reduce the capacitive load for the carpets with greater than 4 nF capacitive load (typically carpets with a 20 cm to 50 cm transport distance, $a = 0.38$ mm) was to segregate the carpet electrodes and drive each segment with a separate LC circuit. In order to limit the minimum amount of required electronics, the restriction of using only 1 AFG and 1 amplifier was imposed. Difficulties encountered with this method included segmenting the carpet electrodes in evenly matched capacitive loads and matching the rf phase and amplitude at the segment boundaries. Since the electrodes were part of a pcb, the segmentation had to be designed beforehand and was permanent so that the capacitive load could not be changed unless the design was changed and a new flex pcb was manufactured.

The matching of the rf phase and amplitude at segment boundaries was achieved by using variable capacitors to tune each phase and a 4-channel oscilloscope was used to observe the two rf phases for the adjacent segments. A tune was determined to be satisfactory when there was $< 15\%$ difference in rf amplitudes and 180° difference between each adjacent phase. The rf phase and amplitude were measured at the carpet surface and also at a diagnostic point outside the chamber as a function of input voltage from the AFG because, once the chamber was closed, there would be no easy way to measure the characteristics of the rf inside the vacuum chamber. All of the values reported in the results represent the rf voltages on the surface of the rf carpet.

The Q-value is a measurement of quality for a resonant circuit defined by:

$$Q = \frac{f_r}{\Delta f} \tag{3.2}$$

where f_r is the resonant frequency as defined above, and $\Delta f = f_H - f_L$, where f_H and f_L are equal to the high half-power frequency and the low half-power frequency respectively. The resonant circuits for these studies did not require a very large Q-value because the rf

discharge limit in He gas was reached long before the maximum rf voltage could be applied to the rf carpet electrodes. Therefore, the Q-value of the circuit was not maximized. The Δf for the resonant circuits used in the ion transport measurements was measured to be 0.08 MHz for a f_r of 2 MHz, resulting in a Q-value of approximately 25. The limiting factor to ion transport was not the Q-value of the resonant circuit, but rather the ability to apply the desired resonant frequency over rf carpets with different capacitive loads with minimal adjustments to the resonant circuit.

3.4.2 DC voltages for the rf carpet

The individual dc voltages for the rf carpet were established using a resistive voltage divider chain. Since the ions are positively charged and transported from an outer radius to an inner radius, a positive voltage, VCarpHi, was applied to the carpet electrodes at the outer radius. Then, for each successive inner electrode, the applied voltage was connected to the next voltage step down from VCarpHi. For the innermost electrode, the applied voltage is one resistive division above electrical ground. This was necessary because the collection electrode, located a carpet gap distance g away from the innermost carpet electrode, was held at electrical ground. Originally, the resistor chain was located outside of the chamber and the individual dc voltages for each rf carpet electrode was brought into the chamber by individual pins in two 9-pin subminiature-D (D-sub) feedthroughs.

This method with, for example, 18 traces of carpet pitch on the order of 1.5 mm and the electrode grouping method in Chapter 2, only results in a transport distance of 5 cm. Increasing the transport distance (20 - 50 cm) and decreasing pitch (sub-mm) would require a multi-pin feedthrough with over 1,000 pins. Fabrication of a 1,000 pin feedthrough is possible, but this still has the problem of attaching 1,000 cables to the rf carpet. In order to avoid having a 1,000-pin feedthrough, the resistor chain was moved to the inside of the chamber and included on the same flex board as the carpet electrode itself by using surface mount technology and designing resistor pads and a routing scheme for each individual carpet trace. This significantly reduced the required feedthroughs for the dc voltages for the rf carpet but

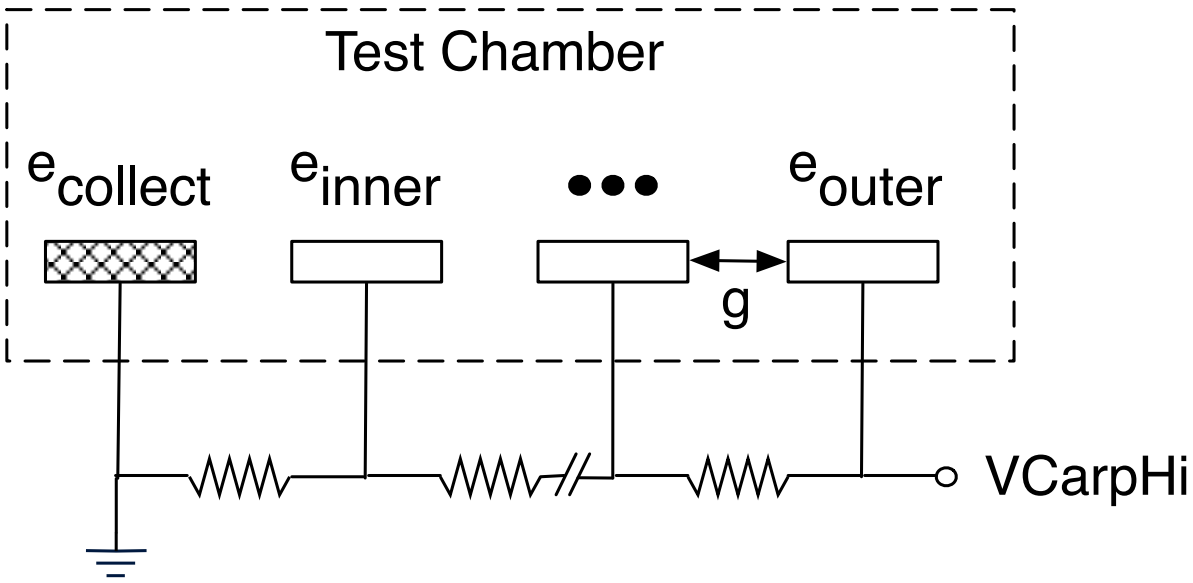

Figure 3.14: Schematic diagram of the initial resistive voltage division used to apply the individual dc voltages to the rf carpet electrodes with the resistor chain located outside the chamber. e_{outer} and e_{inner} refer to the electrodes at the outer radius and inner radius respectively. $e_{collect}$ refers to the collection electrode. g refers to the gap between the rf carpet electrodes. The items encompassed by the dashed line were in the rf carpet test chamber.

increased the complexity of the pcb.

The value of VCarpHi can be converted into the electric drag field strengths, E_{drag}, in (V/cm) by the expression:

$$E_{drag} = \frac{VCarpHi}{MaxDist} \tag{3.3}$$

where MaxDist is the maximum transport distance in cm of the rf carpet (the distance between the outermost radius and the collection electrode).

3.4.3 Combining the rf and dc voltages

Operation of the rf carpet requires a combination of rf and dc voltages. A common method for combining a rf voltage with a dc gradient is to use a resistive voltage divider for the dc gradient and use individual capacitors to transmit the rf signal to each electrode. Originally, like the resistor chain, the capacitors were also located on the outside of the chamber and the

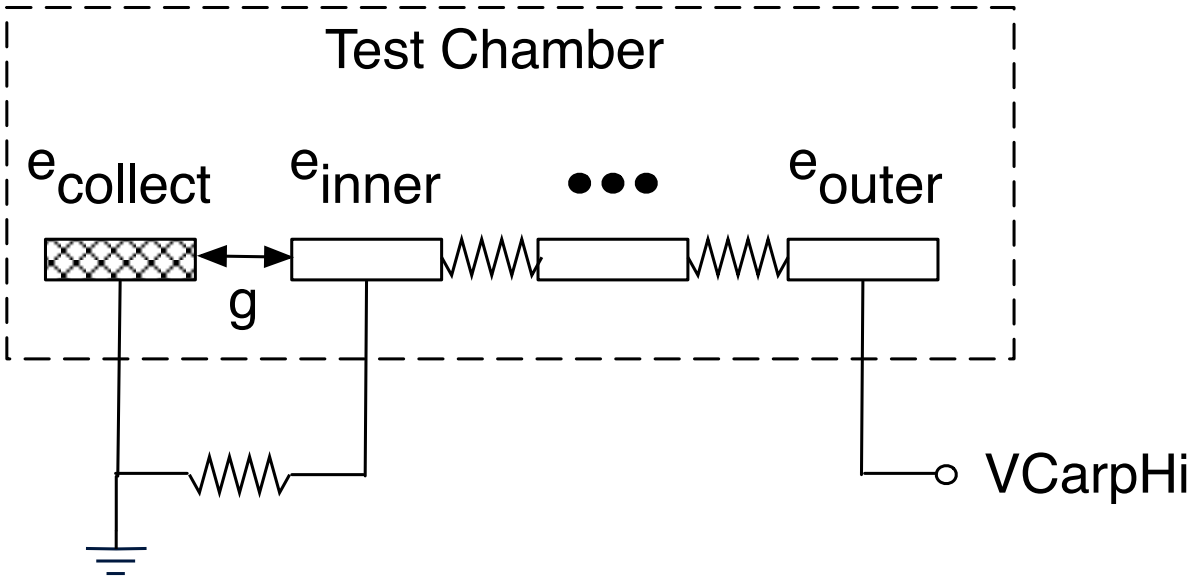

Figure 3.15: Schematic diagram of the resistive voltage division used to apply the individual dc voltages to the rf carpet electrodes with the resistor chain located on the inside of the chamber.

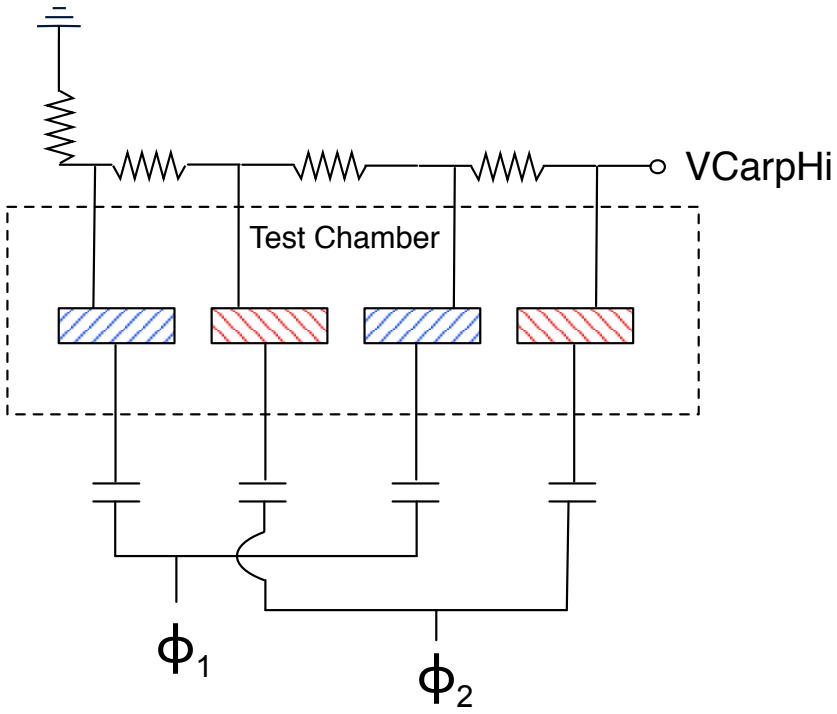

Figure 3.16: Schematic diagram of the method used for early rf carpet prototypes to apply the dc voltages and rf voltages to the individual traces. The resistor chain and capacitors were located on the outside of the test chamber.

combined rf and dc voltage was brought into the chamber with the 9-pin D-sub connectors. A schematic diagram of this method to combine the rf and dc voltages for the rf carpets is shown in Fig. 3.16, where the two phases from the rf circuit are indicated by ϕ_1 and ϕ_2. The same problem was encountered for the capacitors as was for the resistor chains outside of the chamber as discussed in section 3.4.2. It was necessary to devise a way to bring the capacitors into the chamber and to reduce the number of required feedthroughs. Using surface mount capacitors was an option, but this would require mounting of a large

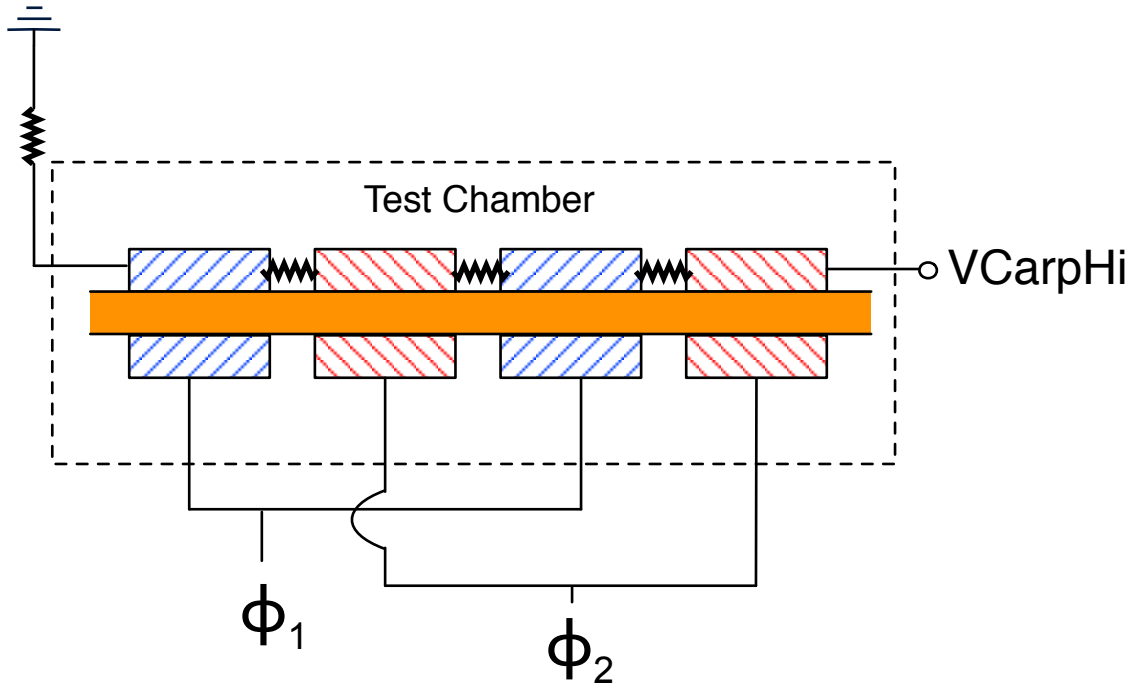

Figure 3.17: Schematic of the method used to apply the dc voltages and rf voltages to the individual traces. The resistor chain and capacitors are located on the inside of the test chamber. The Kapton dielectric is shown in orange. The capacitors are formed from the two Cu traces.

number of additional components on the pcb. A new method was devised to take advantage of the material properties of the different Cu-clad laminates used in flex pcb manufacturing. By using a double-clad Cu laminate (Cu sandwiching a Kapton dielectric) as the material used for the flex circuit, the capacitors for each trace can be created by mirror images of the carpet electrodes on the bottom side of the Kapton substrate. The rf is applied to the underside of the flex circuit which is capacitively coupled to the topside (transport side) of

the flex circuit. The dc voltages were generated with surface mount resistors as in section 3.4.2 and applied directly to the topside of the carpet. This is equivalent to the schematic in Fig. 3.16, but avoids the installation of individual capacitors.

A study was conducted of the amount of rf voltage that was transmitted to the top Cu layer as a function of the amount of overlap between the bottom Cu layer and top Cu layer. The results are shown in Fig. 3.18. From the results, a full mirror image on the bottom side of the Kapton substrate was found to maximize the amount of transmitted rf.

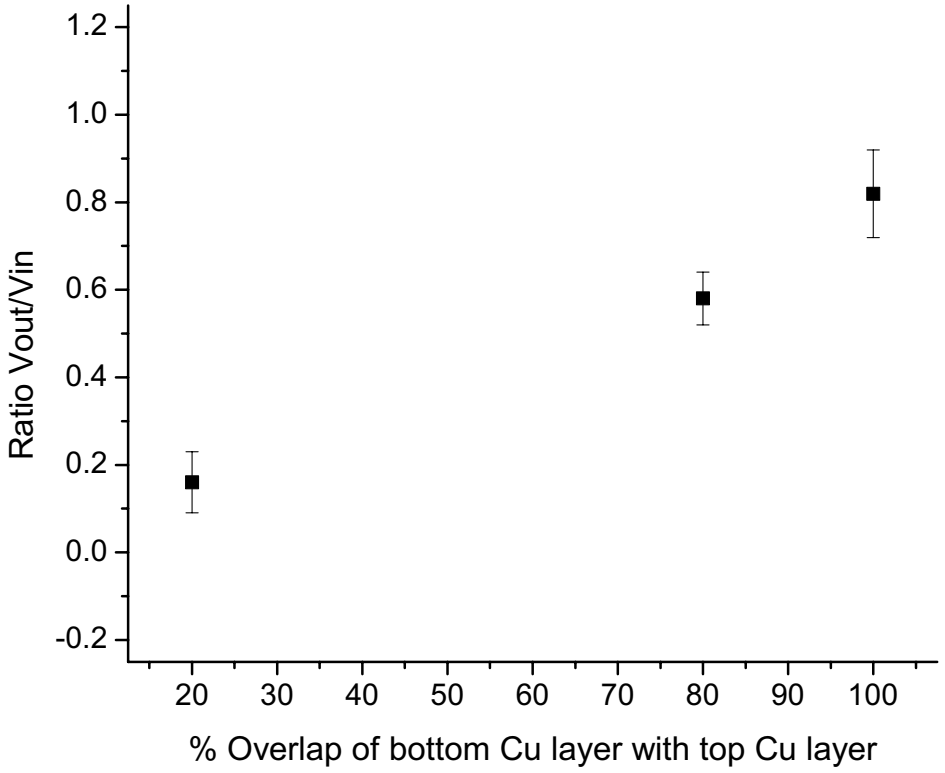

Figure 3.18: Results from the study of capacitive coupling of the voltages to the individual traces. The voltage ratio on the top trace to that on the bottom is shown as a function of fractional overlap of the layers.

3.5 Push electrodes

The push electrodes directed the ions towards the surface of the carpet electrodes by providing a constant electric field perpendicular to the repelling force of the carpet electrodes which then "pushes" the ions near the surface. Aside from the practical aspect of guiding the ions towards the rf carpet, the push field also acted as an artificial space charge field. The reader may recall from Ch. 1 that the space charge field is produced during the thermalization of energetic beams and is primarily responsible for the loss of extraction efficiency with increasing beam rate. Thus, it was important to determine when the repelling force provided by the carpet electrodes was overcome by the space charge field. By measuring the transport efficiency as a function of push field and equivalently, the space charge field, the maximum incoming beam rate that the cyclotron gas stopper could withstand before incurring losses in the extraction efficiency could be calculated. Though the maximum push fields/space charge fields that the rf carpet could operate at were determined, the corresponding beam rates for the push field/space charge fields were beyond the scope of this work. In order to keep

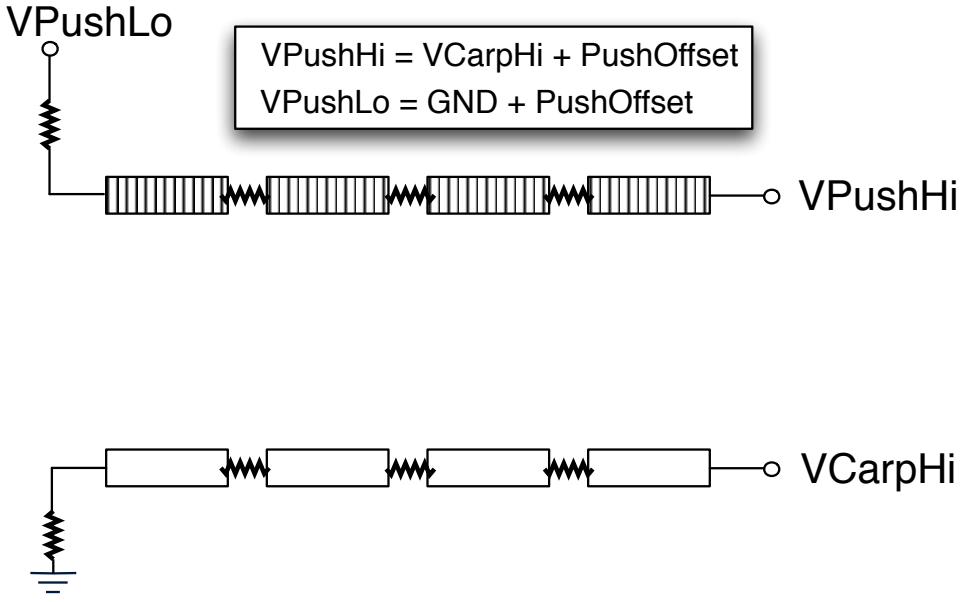

Figure 3.19: Schematic of the voltage designation for the push electrodes using the voltages on the carpet electrodes as a reference.

the push field constant over the full length of the carpet electrodes, exactly the same dc

gradient on the carpet was applied on the push field electrodes as on the transport carpet plus a constant dc offset. The high voltage on the push electrode resistor chain (VPushHi) and the low voltage on the push electrode resistor chain (VPushLo) established the dc gradient. Oftentimes, a copy of the carpet pcb was used to make the push electrodes to match the appropriate shape and dc gradient. The push electrodes were located 13 cm away from the carpet electrodes. The ion source housing was located in between the push and carpet electrodes, and the face was 4 cm away from the carpet electrodes. For instance, if VCarpHi was set to 40 V and the desired push field was 5 V/cm, then VPushHi was set to 85 V and VPushLo was set to 45 V. A photograph of the ion source positioned inbetween the carpet electrodes and push electrodes is shown in Fig. 3.20.

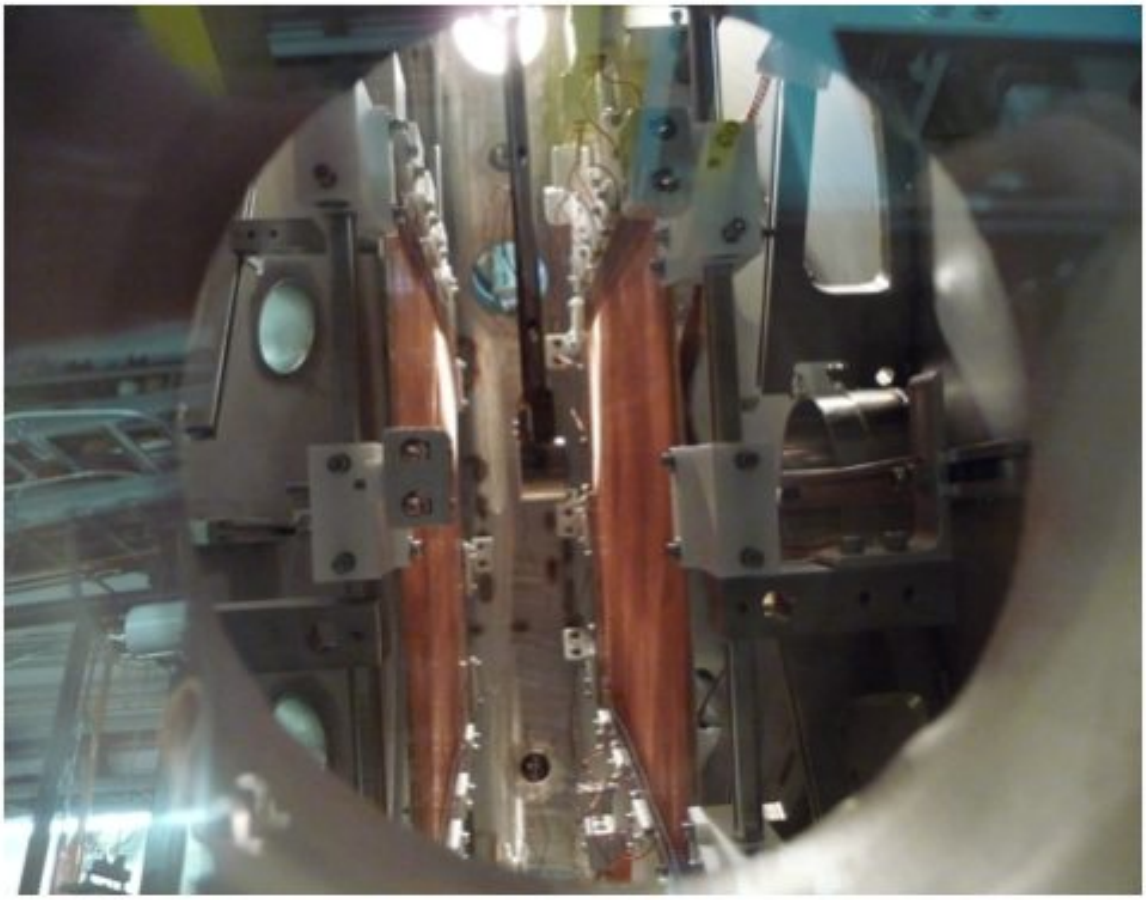

Figure 3.20: A photograph of the ion source located in between a 50 cm rf carpet (right) and the push electrodes (left).

3.6 Calibration of the ion source current

The measurements to calibrate the ion source current were important to establish the size of the ion current leaving the ion source and impinging on the carpet electrodes since that value was used to determine the transport efficiency. With the definitions introduced in section 3.2 to measure the ion current leaving the ion source $[I(IS)]$ and the ion current hitting the ion source housing $[I(Lens)]$, the ion current leaving the ion source housing $[I(Carp)]$ is given by:

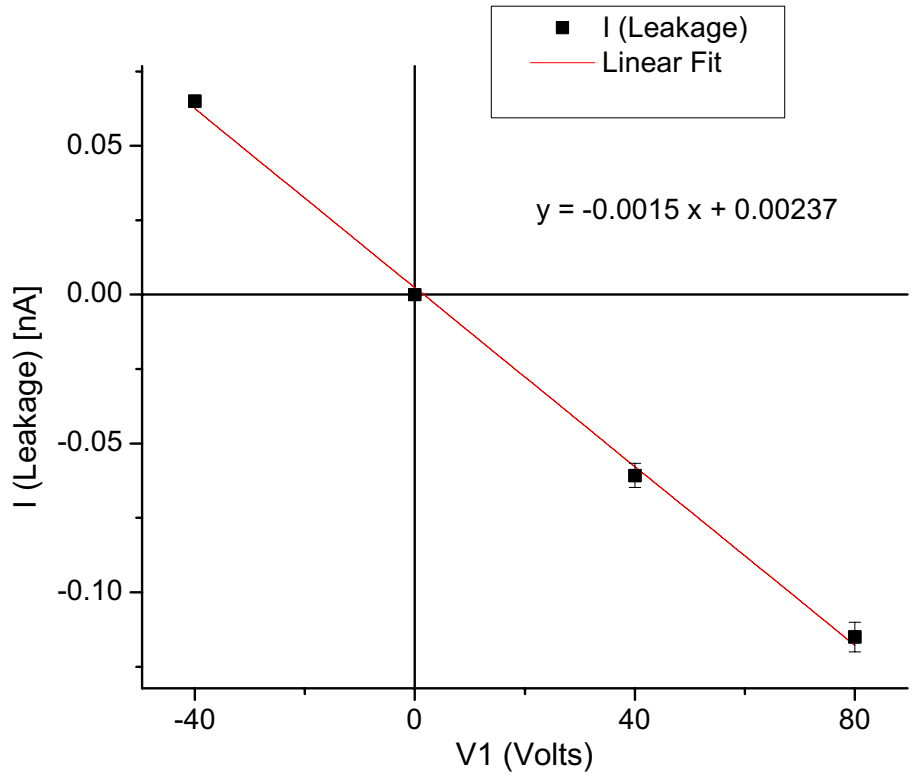

Figure 3.21: Calibration of the ion source output used for transport efficiency measurements.

$$[I(Carp)] = [I(IS)] - [I(Lens)]. \tag{3.4}$$

$[I(Carp)]$ differs from $[I(Coll)]$, the ion current measured on a collection electrode, and $[I(CP)]$, the ion current measured on the collection plate, because $[I(Carp)]$ is not a directly

measured quantity. For transport measurements, $[I(Carp)]$ was typically in the range of 1 - 2.5 nA. With the ion source housing and ion source biased in the range of 50 - 150 V, the current measurements would be sensitive to any leakage current due to stray resistances on the order of GΩ between any ion source component and electrical ground. Due to the humidity of the environment and the cleanliness of the insulating break separating the ion source feedthroughs on the outside from the test chamber at ground potential, a resistance on the GΩ level often did exist and the leakage currents had to be accounted for when calculating the true ion source current output. For calibration purposes, only the voltage on the ion source (V1) and the voltage on the ion source housing (V2) had to be monitored. Calibrations were conducted prior to and following transport measurements. The calibration procedure went as follows: (1) V1 and V2 were kept at the same voltage level and scanned from -40 V to 80 V in steps of 40 V while recording the current measurement for the ion source and ion source housing. The current measurement would vary linearly for the ion source and stay at a constant value for the ion source housing. This would provide enough points for a linear calibration (from Ohm's law). A sample measurement is shown in Fig. 3.21 which indicates the resistance was 667 GΩ.

A check of any resistance between the ion source and ion source housing was made next. (2) V2 was set to 10 V below V1 and the same voltages were stepped through. The current measurements were recorded for both the ion source and ion source housing. A 10 V potential difference was used because this value was typically used for transport measurements. Over the course of the entire study, no noticeable resistance was found between the ion source and the ion source housing down to the level that could be observed with a Keithley picoammeter.

Once the calibration was taken and the ion source temperature reached equilibrium, the calibration could be applied for the determination of the ion source current leaving the ion source housing. A check of this calibration was done by positioning the ion source directly above the collection plate and confirming that:

$$[I(Carp)]_{corr} = [I(CP)] \tag{3.5}$$

where $[I(Carp)]_{corr}$ is the corrected value from the calibration. This allowed a direct check of the calibration without having to disentangle the transport along the rf carpet.

The transport efficiency of the rf carpet, ϵ_{trans}, was then given by the expression:

$$\epsilon_{trans} = \frac{[I(Coll)]}{[I(Carp)]_{corr}}. \tag{3.6}$$

3.7 Linear carpet transport

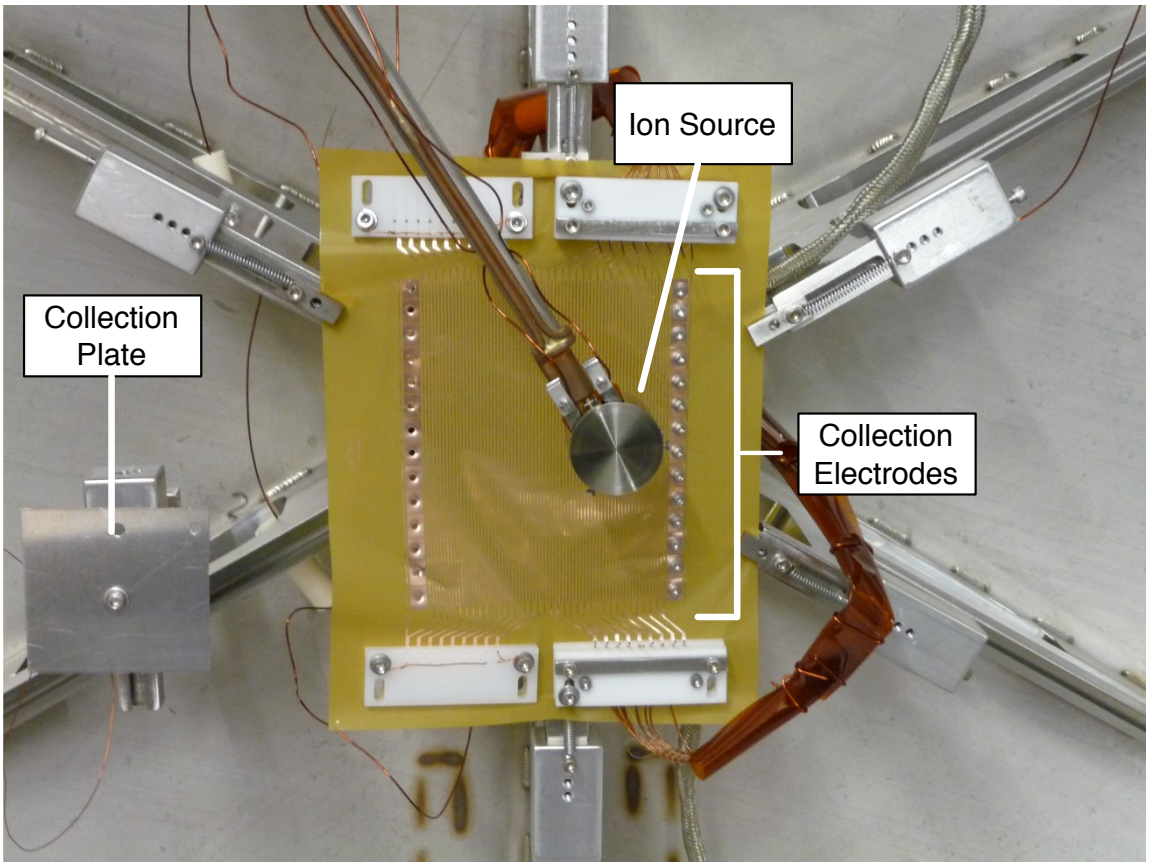

Figure 3.22: A photograph of the setup used in the transport measurements with the linear rf carpet. With this setup, the ion source could be moved to the collection plate to verify the transport efficiency.

A variety of rf carpet designs were studied throughout the measurements, but the general operating principles described in the previous section remained the same. For the most part, the push electrodes were changed to match the shape of the current rf carpet design. The

linear rf carpet transport setup was the first rf carpet setup used for transport measurements. The transport distance was 5.4 cm and the ion source housing acted primarily as the push electrodes because it extended across 80% of the transport length. Since a dc gradient could not be applied to the ion source housing, the push fields were not constant across the transport distance. This setup demonstrated the first ion transport with rf carpets at the NSCL, but more reliable measurements were found in later setups. A photograph of the linear rf carpet setup is shown in Fig. 3.22.

3.8 Semi-circle transport and extended semi-circle transport

The electrode configurations were modified to be larger semi-circular patterns for better ion confinement with transport distances up to 18 cm. The final design consisted of a semi-circular pattern with a radius of 17 cm with a series of arcs that extended the transport distance to 48 cm all within the 40 x 50 cm^2 area. The pitch was 0.38 mm and the gap spacing was 0.19 mm. The setup is shown in 3.23.

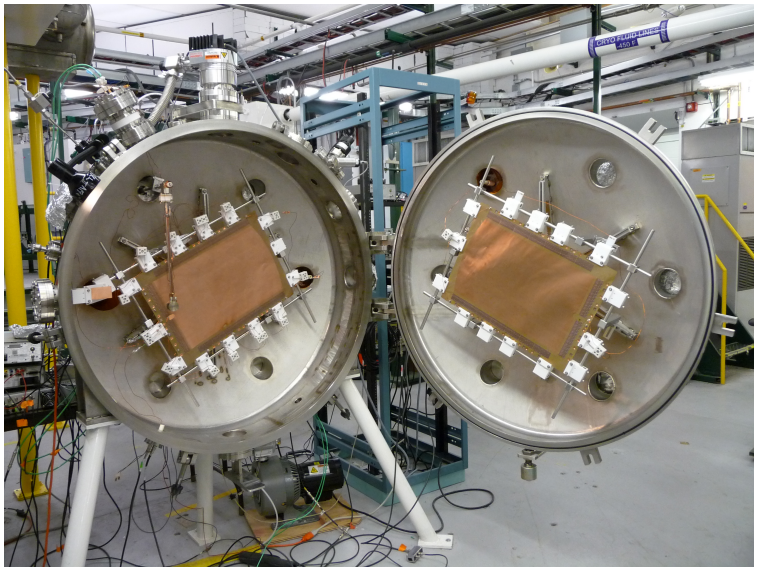

Figure 3.23: Test setup for a large 50 cm rf carpet (a = 0.38 mm, γ = 0.5. Push electrodes are shown on the chamber door.

3.9 Discharge tests

Before transport measurements were conducted, measurements to determine the maximum rf voltage that could be applied to the carpet electrodes before causing dielectric breakdown of the He gas were conducted. Using the same flex pcb material used to fabricate the rf carpets, a small series of test pads were constructed with varying electrode and gap widths ranging from 0.2 mm to 0.7 mm. A small mounting support coupled to a 6" conflat flange

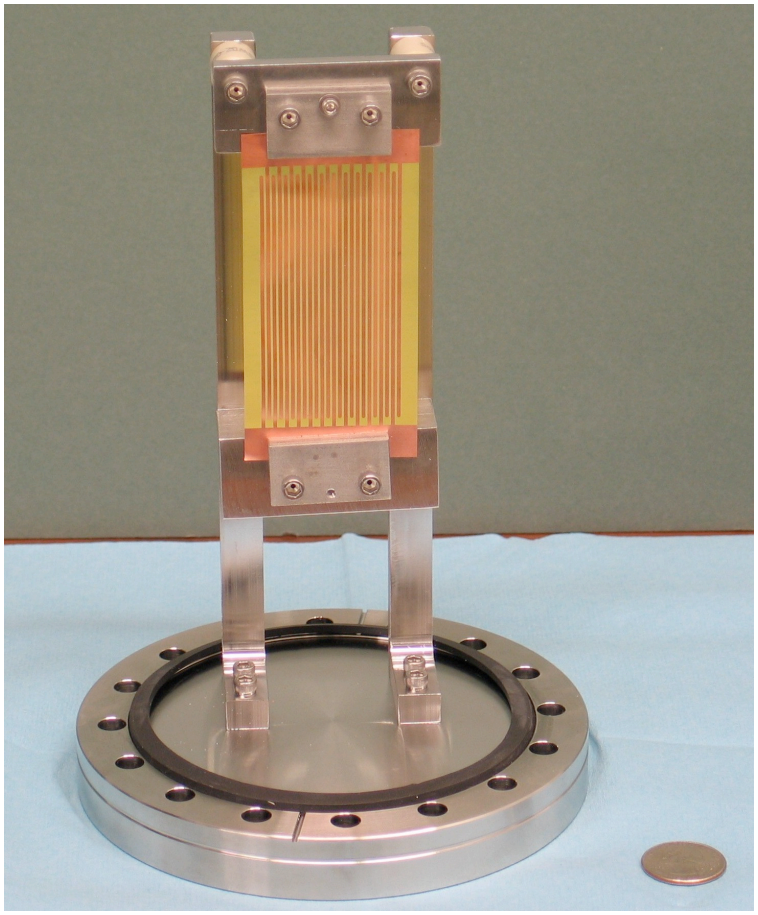

Figure 3.24: A photograph of the support structure and test pad used in the discharge tests on a 6" conflat flange.

was constructed to keep the flex PCB surface uniform with insulated standoffs to apply the voltage to the test pad as shown in Fig. 3.24. Additional insulation in the form of ceramics and Kapton were used to ensure that the discharge occurred between the parallel small electrodes on the pad and not between the structure and the chamber walls. The chamber pressure was set to the desired value and the applied RF voltage increased till a discharge

was observed between the adjacent electrodes.

A set of measurements with one test pad at two different rf frequencies is shown in Fig. 3.25.

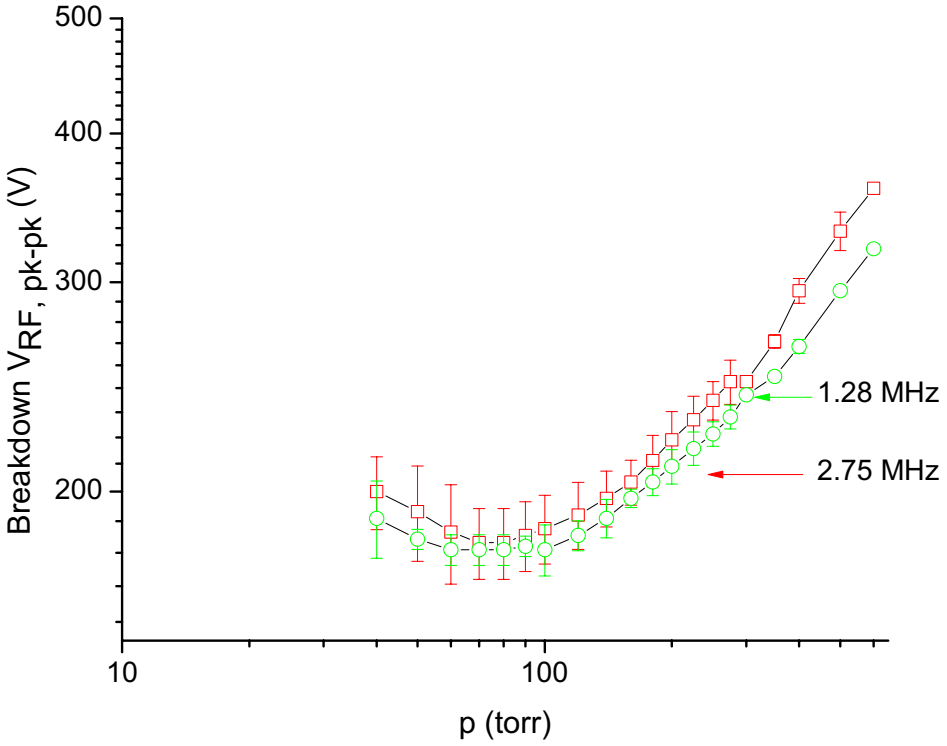

Figure 3.25: Measured rf voltage breakdown voltage (frequency shown in plot) for an electrode gap spacing of 0.7 mm and an electrode width of 1 mm.

These two rf frequencies spanned the initial rf frequency operating range for the rf carpets. This measurement showed that the breakdown voltage had almost no variation over this frequency range. A more instructive method of displaying the breakdown curves was to show them as a function of pressure times distance (pd). This function collapses all of the data (See Fig. 3.26), which then allowed predictions of the rf breakdown voltage at the relevant operating pressures and electrode gaps. This is shown in Fig. 3.26. Unfortunately, the rf breakdown curves indicate that the desired operating pressure and rf carpet electrode gap correspond to the minimum of the breakdown curve!

A strong dependence on the gas purity as evidenced by the number of purge cycles (Sec.

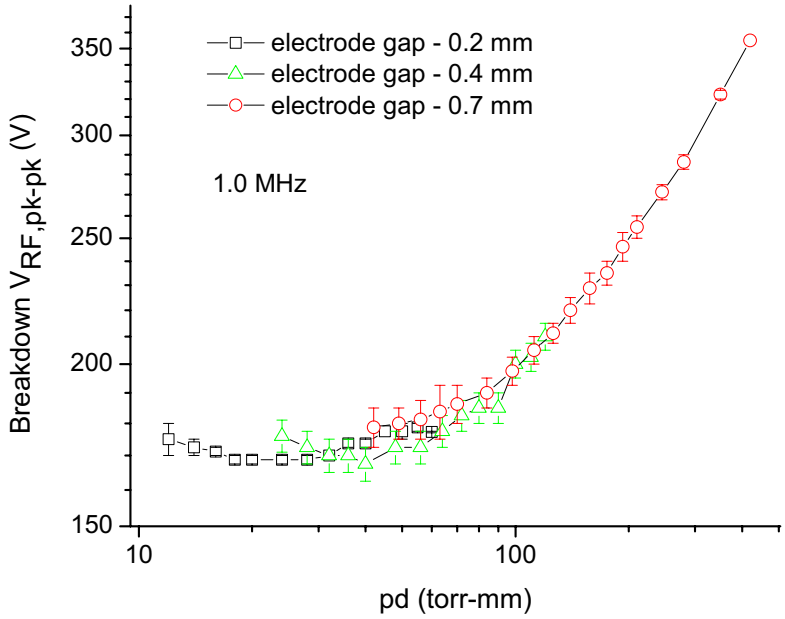

Figure 3.26: Measured rf breakdown voltage as a function of pd constructed from the rf breakdown curves taken at three different electrode gaps.

3.1) was found in the variation of the measured breakdown voltages (see Fig. 3.27.). The variability of the breakdown is due to the different contaminants in the system that can drive the breakdown voltage higher or lower as seen in [21]. Care was then taken to prepare the system and verify that a reference point on the breakdown curve could be reproduced after each time the chamber was opened, pumped down, and purged.

3.10 Setting voltages for transport measurements

The voltages on the rf carpet electrodes and push electrodes were set before the beginning of every transport measurement. Voltage settings were chosen that would lead to stable ion motion over the rf carpet and not incur discharge. An rf frequency of 2 MHz at 160 $V_{RF,pk-pk}$ and a push field and drag field of 3 V/cm at 80 torr was simulated to have stable ion motion over the rf carpet. The E_{pr} and E_d/κ stability parameters for these rf carpet settings are 1.78×10^{-2} and 1.11×10^{1} respectively, and correspond to the region of ion motion stability

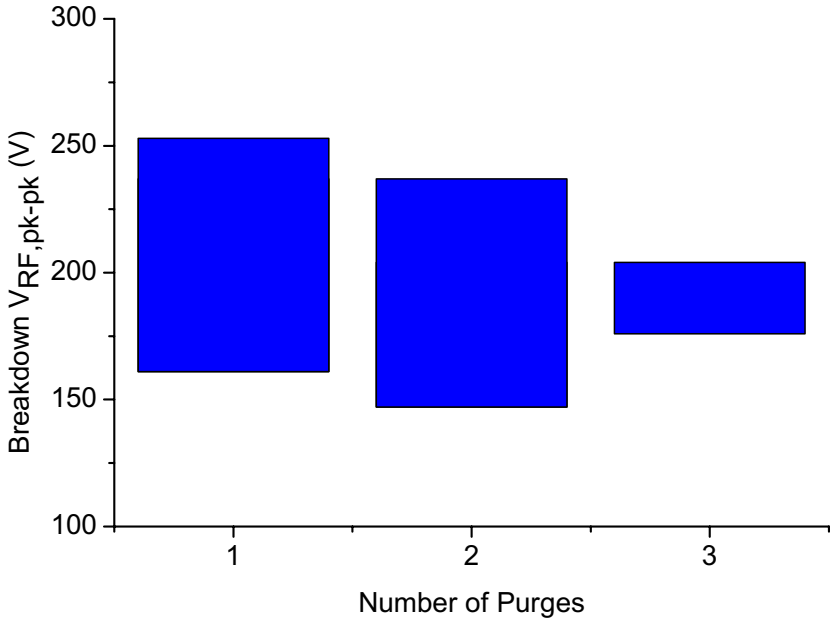

Figure 3.27: Range of the measured rf (1.5 MHz) breakdown voltage as a function of the number of purges at an electrode gap of 0.525 mm and a pressure of 60 torr.

introduced in Sec. 2.6.

The voltages for $VCarpHi$, $VPushHi$, and $VPushLo$ were calculated from the desired electric field strengths for the drag field and the push field. For example, a drag field of 3 V/cm with the collection electrode at ground potential and a transport distance of 48 cm would correspond to $VCarpHi$ being biased to 144 V. The push electrodes were located 13 cm above the carpet electrodes, and a desired push field of 3 V/cm for a rf carpet with a 3 V/cm drag field would correspond to $VPushHi$ and $VPushLo$ being biased to 183 V and 39 V respectively. The voltages that were applied to the ion source housing were calculated in a similar manner. The ion source was located 4 cm away from the carpet electrodes and sat at a variable radial position on the rf carpet. The ion source housing was biased in a manner to have the same electric field strength as the push field. For example, in the scenario of a 3 V/cm drag field and push field, the ion source sitting at a 10 cm radial distance away from the collection electrode would be biased to 69 V.

3.11 Uncertainty in the transport measurements

The error bars for the transport measurements are given by the standard error of the mean (SE) for repeated measurements given by:

$$SE = \frac{\sigma}{\sqrt{n}} \tag{3.7}$$

where σ is the sample standard deviation and n is the number of measurements.

3.12 Transport measurements

The transport measurements mainly consisted of three parts: 1) determining if the rf carpet could operate and transport ions at the operating pressures of the cyclotron gas stopper, 2) if ions could be transported over distances corresponding to the average radius of stopped ions predicted by simulations, and 3) if ions could be extracted from the rf carpet. In addition to these three main studies, many measurements were conducted that gave further insight into the operation of rf carpets and these will also be presented in the following sections.

3.12.1 The effect of the applied rf voltage

This section will initiate the discussion of the transport of ions and reveal the limitations on the transport of ions using rf carpets imposed by the effective potential and the rf discharge limit. These limitations will naturally lead into the discussion of the pressure limits on the operation of rf carpets.

The applied rf voltage to the electrodes plays the most important role in the transport of ions because the strength of the effective potential was proportional to the square of the applied rf voltage. Conceptually, the greater the applied rf voltage, the farther the ions can be transported above the rf carpet surface, and the less likely for a collision between the ions and the electrodes to occur. From the rf discharge limits measured in Ch. 4, the applied rf voltage cannot be increased indefinitely, rather electrical discharge creates a hard constraint

on the ion transport. By measuring the transport efficiency as a function of the applied rf

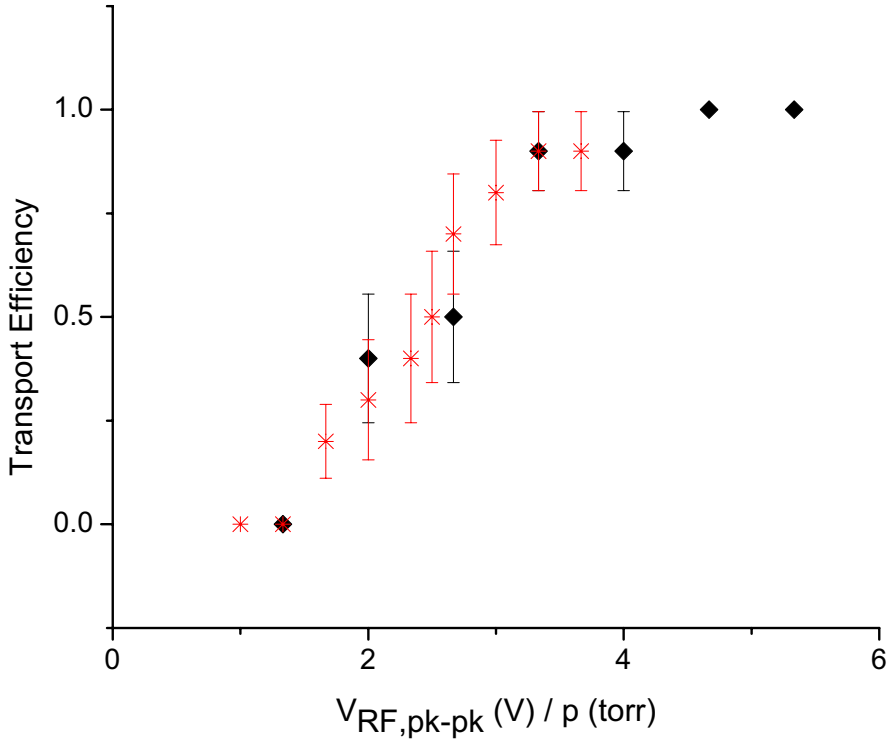

Figure 3.28: Results from simulations of rf carpet ion transport indicating a pressure scaling relationship by the collapse of the transport efficiency curves in $V_{RF,pk-pk}(V)/p(torr)$ space. Rf carpet parameters: Rf = 2 MHz, Drag Field = 3 V/ cm, Push Field = 30 V/cm, Transport Distance = 5 cm, Pitch = 0.38 mm, γ=0.5. Black diamonds: 30 torr, Red stars: 60 torr.

voltage, the transmission efficiency curves can be used to predict the required rf voltages to reach the same transport efficiencies at different pressures. This is possible because the effective potential scales with the ratio $V_{RF,pk-pk}(V)/p(torr)$. This general pressure scaling trend was also confirmed through simulations shown, for example, in Fig. 3.28 using the hard-sphere collision model introduced in Section 2.7.3.

The measurements to determine the effect of the applied rf voltage were conducted with all other experimental parameters held at constant values. The reported rf voltages are the $V_{RF,pk-pk}$ values measured at the surface of the rf carpet electrodes. Since the rf discharge limit was determined before the transport measurements, the maximum applied rf voltage for transport measurements was limited to be 10 - 15 $V_{RF,pk-pk}$ below the discharge limit,

with typical values of 160 - 170 $V_{RF,pk-pk}$ depending on the gas pressure and electrode pitch. The transport efficiency was then determined for different applied rf voltages up to this maximum limit and the data were then used to construct a transport efficiency response curve for those particular settings. A simple example is shown in Fig. 3.29. This process was repeated a minimum of three times in both the direction of increasing and decreasing applied rf voltages for each set of parameters.

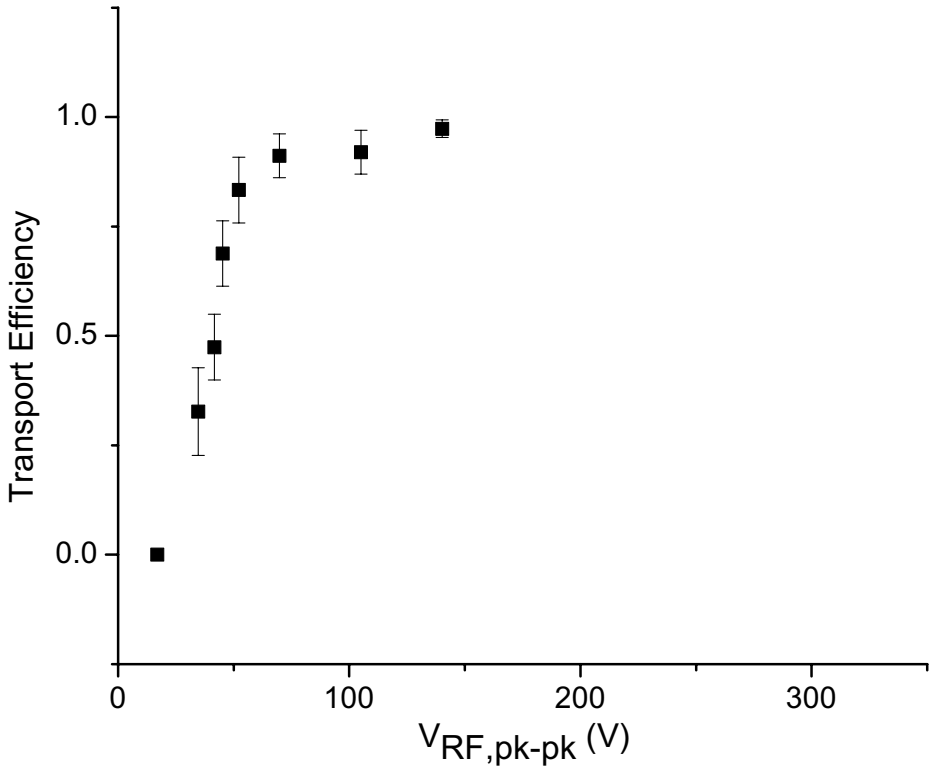

Figure 3.29: Measured transport efficiency as a response to the applied rf voltage on the carpet electrodes. Experimental parameters: Chamber pressure=20 torr, Rf = 3.47 MHz, Drag Field=3 V/cm, Push Field=3 V/cm, Transport Distance=16 cm, Pitch = 0.38 mm, γ=0.5, $I(Carp)$ = 700 pA.

With certain experimental parameters, it was possible that the ions could travel to the collection electrode without any transport along the rf carpet electrodes. With the typical experimental parameters mentioned in the text, this always occurred when the ion source was located less than 3 cm away from the collection electrode. In order to ensure that

the transported current was completely due to transport over the rf carpet, a check was made that there was no current measured on the collection electrode when the rf voltage was reduced to 0 $V_{RF,pk-pk}$. A second check to confirm that the current measured at the collection electrode was all due to transported ions, was that no measured current should be on the collection electrode when the ion current leaving the source was reduced to zero with all the electrodes biased.

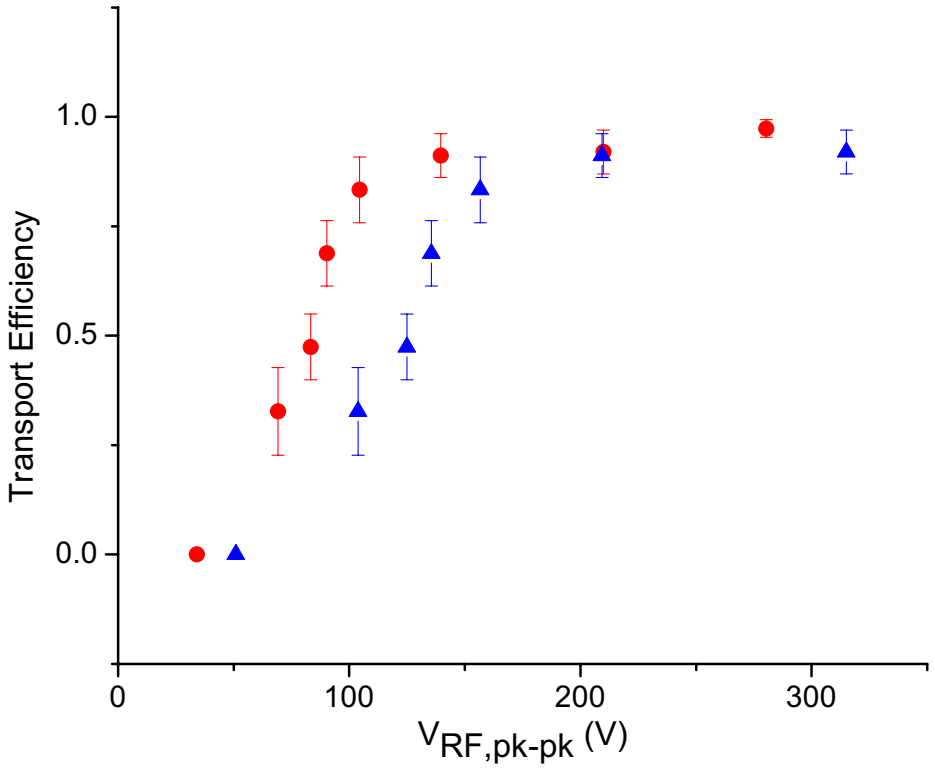

Figure 3.30: Example of the predicted transport efficiency curves scaled from the data in Fig. 3.29 as a function of the applied rf voltage on the carpet electrodes. Rf carpet parameters: Rf = 3.47 MHz, Drag Field=3 V/cm, Push Field=3 V/cm, Transport Distance=16 cm, Pitch = 0.38 mm, γ=0.5. Red circles: 40 torr, Blue triangles: 60 torr.

Verification of the pressure scaling first required a measurement at a gas pressure that could provide the complete shape profile for the efficiency curve and had a transport efficiency near 100% for at least one applied rf voltage value. The complete curve removed the problem of the extrapolation to calculate the applied rf voltage for transport efficiencies approaching

100%. Chamber pressures of 20 - 30 torr typically provided the appropriate gas pressure to obtain a complete transport efficiency profile such as that shown in Fig. 3.29.

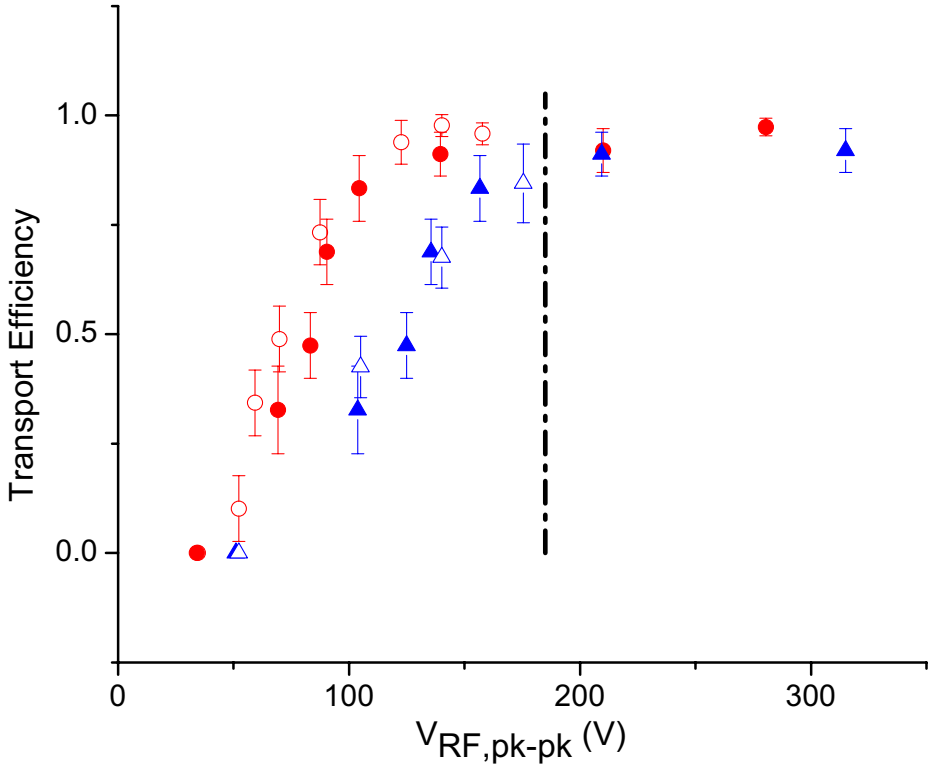

Figure 3.31: Comparison of measured (open symbols) and predicted (closed symbols) transport efficiency curves as a function of the applied rf voltage on the carpet electrodes. Rf carpet parameters: Rf = 3.47 MHz, Drag Field=3 V/cm, Push Field=3 V/ cm, Transport Distance=16 cm, Pitch = 0.38 mm, γ=0.5. $I(Carp)$ = 700 pA Red circles: 40 torr, Blue triangles: 60 torr. Black dot-dash line: discharge limit.

Once the complete transport efficiency curve was obtained, it could be used to predict the applied rf voltage needed at different pressures to achieve the same transport efficiency by scaling the applied pressure with $V_{RF,pk-pk}(V)/p(torr)$. Using this scaling and the results from Fig. 3.29, predictions of the transport efficiency at higher pressures as a function of the applied rf voltage were made. Two example predictions are shown in Fig. 3.30. This pressure scaling technique suggests that a 100% transport efficiency across the rf carpet could be achieved if the applied rf voltage could be increased accordingly. Unfortunately, the

measured transport efficiencies are limited by rf discharge and is shown as the dashed line in Fig. 3.31.

The measured transport efficiencies and the predicted transport efficiencies were in good agreement with each other and provided a useful tool to verify if transport efficiency measurements were consistent amongst each other at different pressures for identical rf carpet parameters over time.

Though scanning the applied rf voltage was instructive, the actual operating mode of the rf carpet would be to apply the maximum rf voltage on the rf carpet electrodes without incurring discharge. The maximum transport efficiency that could be achieved (dictated by the maximum rf voltage that could be applied) at a buffer gas pressure was the truly significant measure of how efficient rf carpets would be in the pressure regime of the cyclotron gas stopper.

3.12.2 Operating pressures of the rf carpet

One of the main requirements for the rf carpet was that it had to transport ions in the pressure regime of the cyclotron gas stopper. The impact of the buffer gas on the confining force of the rf carpet was discussed in Section 2.2.1. From the simulations of the cyclotron gas stopper that included solid degraders arranged azimuthally in the stopping chamber, the pressure range was found to be 40 - 110 torr. This section will present the results obtained for the transport efficiency of the rf carpet in this pressure regime.

Measurements for determining the transport efficiency at different pressures was straight forward once appropriate voltages were determined for the rf carpet electrodes and push electrodes. The applied rf voltage was set to the maximum voltage before discharge occurred. According to the rf discharge curve, the broad minimum sits in the desired pressure range and the rf voltage did not vary by more than 10% over the studied pressure range. The ion source was positioned over the rf carpet and a certain distance away from the collection electrode. The ion current on the rf carpet, $I(Carp)$, was held constant during the pressure scan. The transport efficiency was determined initially at 20 torr and then the pressure of

the test chamber was increased. At each new pressure for which a measurement would be taken, the gas inlet was closed and the ion current on the rf carpet was allowed to stabilize before the transport efficiency was determined. The results from a single measured pressure scan for the rf carpet with one set of rf carpet parameters and the predictions from pressure scaling from the previous section are shown in Fig. 3.32. The predictions of the transport efficiency at different pressures are in good agreement with the measured values, but show a trend of decreasing transport efficiency at the higher pressures needed for the cyclotron gas stopper.

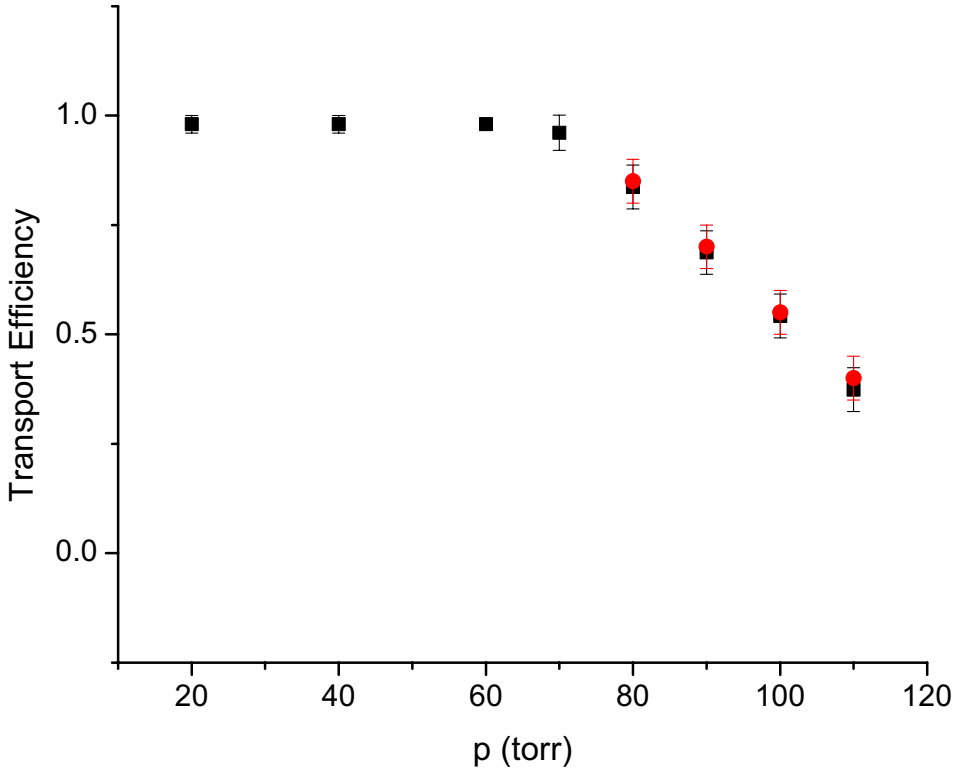

Figure 3.32: Measured (black squares) and predicted (red circles) transport efficiency of the rf carpet over the operating pressure regime of the cyclotron gas stopper. Rf carpet parameters: Rf = 3.47 MHz at discharge limit, Drag Field=3 V/cm, Push Field=3 V/cm, Transport Distance=16 cm, Pitch = 0.38 mm, γ=0.5, $I(Carp)$ = 700 pA. Black squares: Measured, Red Circles: Predictions.

From these measurements, we gained insight into the performance of rf carpets at higher

pressures which would be more suitable for a linear gas stopper. Since the scaled values of the transport efficiency over the pressure range are in very good agreement with the results, the predictions can be extended further to predict the pressure limit of the rf carpets. The predictions were made by using the scaling technique described in the previous section on a transport efficiency profile at 60 torr to arrive at the predicted transport efficiency profiles at the higher pressures. The data points for the predictions shown in Fig. 3.33 were obtained by finding the intersection of the separate transport efficiency curves and an applied rf voltage of 170 $V_{RF,pk-pk}$ corresponding to 10 $V_{RF,pk-pk}$ below the rf discharge limit.

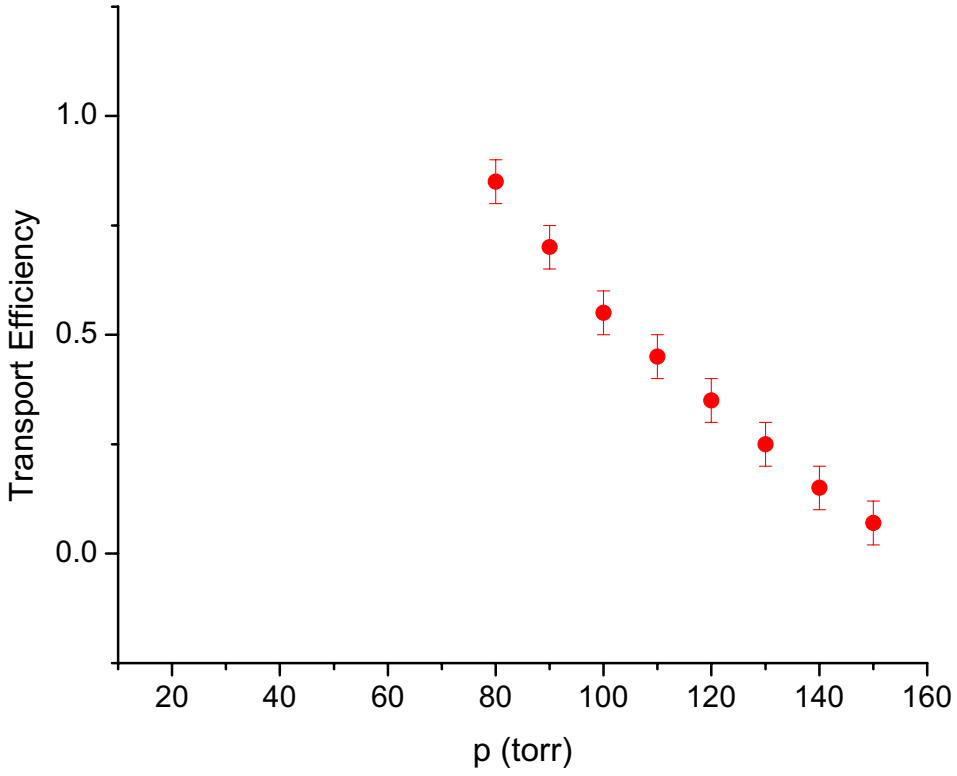

Figure 3.33: Predicted transport efficiency as a function of pressure for the rf carpets. Rf carpet parameters: Rf = 3.47 MHz at discharge limit, Drag Field=3 V/cm, Push Field=3 V/cm, Transport Distance=16 cm, Pitch = 0.38 mm, γ=0.5, $I(Carp)$ = 700 pA.

From the predicted transport efficiencies, the performance of the rf carpet is expected to drop steadily to 150 torr where the transport efficiency is <10%. To put this in perspective,

the NSCL linear gas cell, was operated without rf electrodes at pressures up to 760 torr.

The rf carpet parameters that impact the transport efficiency at higher pressures that can be varied are the rf driving frequency and the pitch. Increasing the rf amplitude would also increase the transport efficiency, of course, but the rf amplitude would always be discharge limited in this pressure and electrode gap regime. Increasing the rf driving frequency, an increase in the transport efficiency was observed. This variation is shown in Fig. 3.34. This

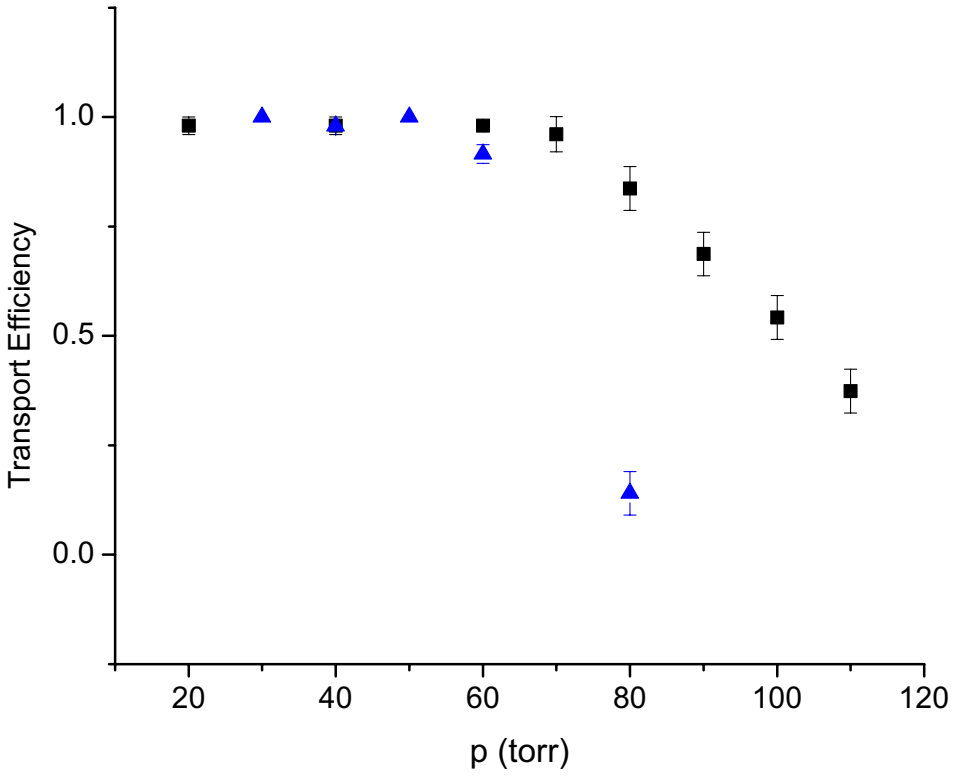

Figure 3.34: Comparison of transport efficiency over the operating pressure regime of the cyclotron gas stopper for a rf driving frequency of 2 MHz (blue triangles) and 3.47 MHz (black squares). Rf carpet parameters: Rf voltage at discharge limit, Drag Field = 3 V/cm, Push Field = 3 V/cm, Transport Distance = 16 cm, Pitch = 0.38 mm, $\gamma = 0.5$, $I(Carp) =$ 700 pA.

increase in transport efficiency is not directly apparent in the effective potential equations, but is revealed when considering the micromotion (oscillations) of the ion due to the applied rf. At lower frequencies, the ion travels a longer distance than it does at higher frequencies

before it undergoes a change in direction due to the change in the phase of the rf. This leads to an ion moving closer to the rf carpet for lower rf frequencies than higher rf frequencies. This can be seen in the example trajectories of ions from simulations of ion transport along an rf carpet shown in Fig. 3.35. This effect becomes exacerbated in more realistic microscopic simulations that include collisions with the neutral buffer gas. Due to the fact that resonant circuits are used to apply the rf voltage, increasing the rf frequency is a challenging task because of the large capacitive load of the rf carpet. The challenges of large capacitive loads in resonant circuits and a method to approach this problem is discussed in detail in Section 3.4.1.

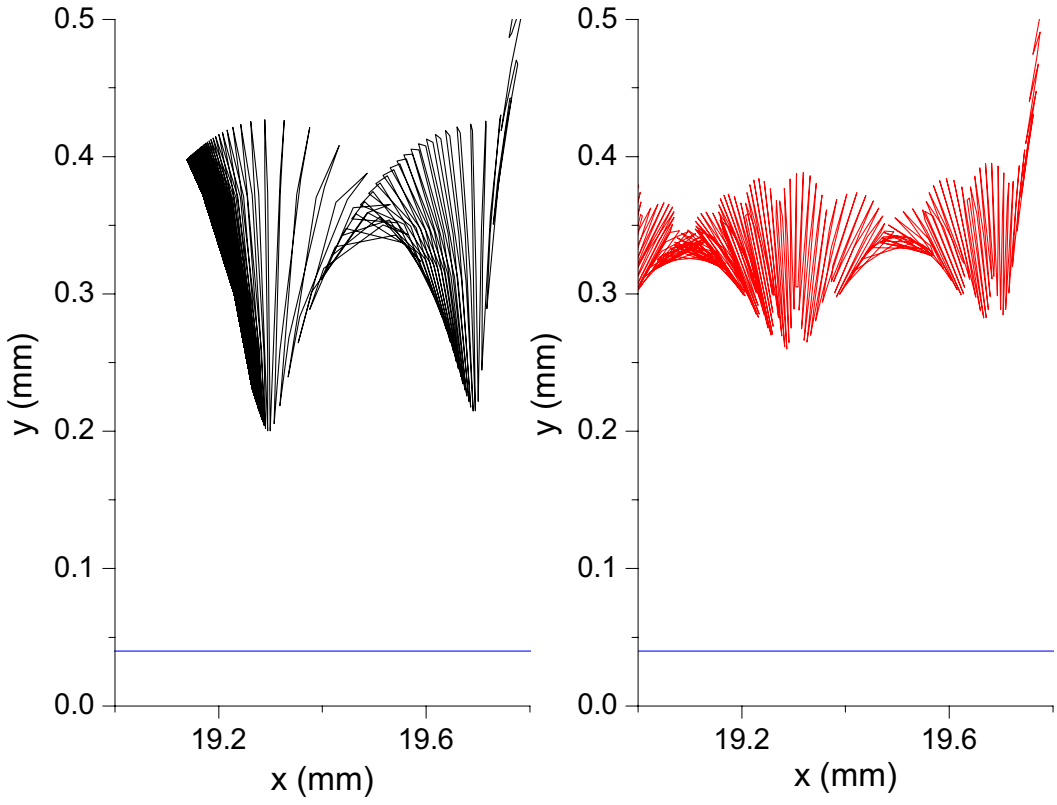

Figure 3.35: Typical simulated trajectories of ions at 2 MHz (black line) and 3.47 MHz (red line) showing that increasing the rf driving frequency increases the ion's minimum distance from the rf carpet surface (blue line) and therefore increases the ion's survivability.

Another rf carpet parameter that has an important effect on the transport efficiency

at higher pressures is the electrode pitch. By decreasing the electrode pitch, an increase in transport efficiency was observed, as is shown in Fig. 3.36. It should be noted that the measurements conducted with the rf carpet with the larger pitch were performed much earlier than those with the smaller pitch and therefore had a $I(Carp) \geq$2.5 nA. Thus, for a proper comparison, the results of a smaller pitch carpet will also be presented for the relatively large values of $I(Carp) \geq 2.5$ nA. It was subsequently observed that localized losses under the ion source were highly dependent on $I(Carp)$ and that the transport efficiencies were not representative of the true performance of the rf carpet for $I(Carp) > 1$ nA. With that said, the results presented for the pitch comparison are sufficient for comparison purposes.

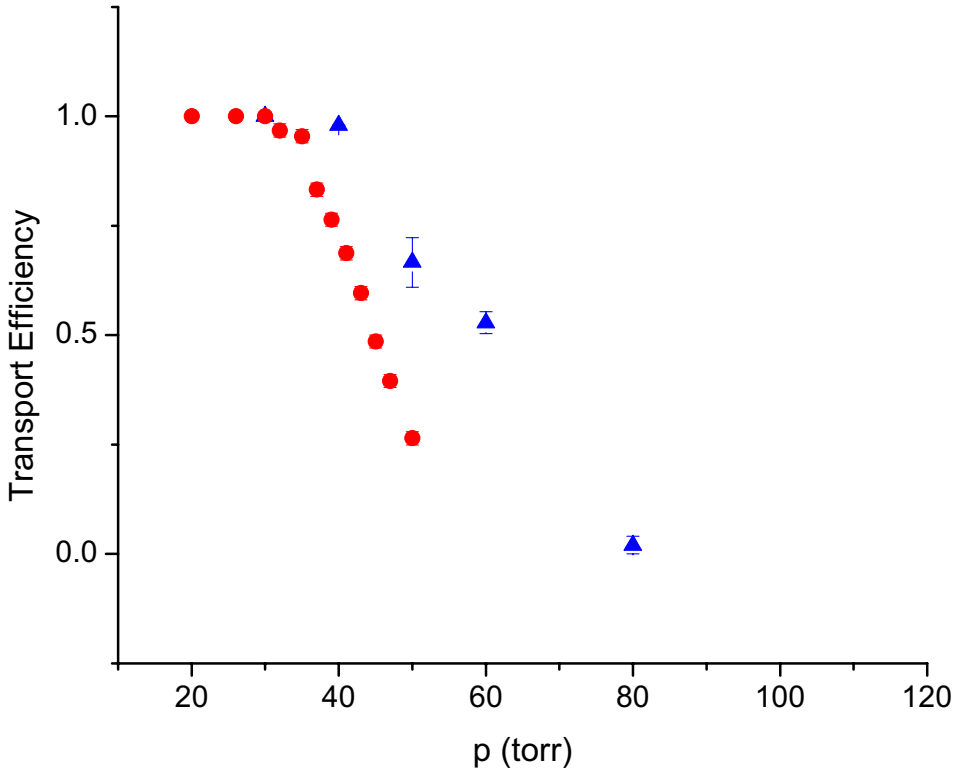

Figure 3.36: Comparison of the transport efficiency for a pitch of 1.5 mm, $\gamma = 0.7$ (red circles) and a pitch of 0.38 mm, $\gamma = 0.5$ (blue triangles). Rf carpet parameters: Rf voltage at discharge limit, Drag Field = 3 V/cm, Push Field = 3 V/cm, Transport Distance = 16 cm, $I(Carp) \geq 2.5$ nA.

This gain in transport efficiency from reducing the pitch arises from an increase in the

effective potential. Pitches of 1.5 mm and 0.38 mm were studied in these measurements. Reducing the pitch much below 0.38 mm is limited by the manufacturing capabilities of pcb companies where a typical 5 mil. gap and trace width are possible corresponding to a minimum pitch of 0.25 mm. The difference in the calculated effective potential provided by a rf carpet with a pitch of 1.5 mm and 0.38 mm is presented in Fig. 3.37 along with the calculated effective potential for a rf carpet with a pitch at the manufacturing limit of 0.25 mm. Note that such a reduction in pitch leads to an increase in the capacitive load and a resultant decrease in the resonant frequency, which goes in the opposite direction of the desired trend. A solution to the increased load would be to use even more additional segmentation along the carpet as discussed in Section 3.4.1 which requires additional rf circuits.

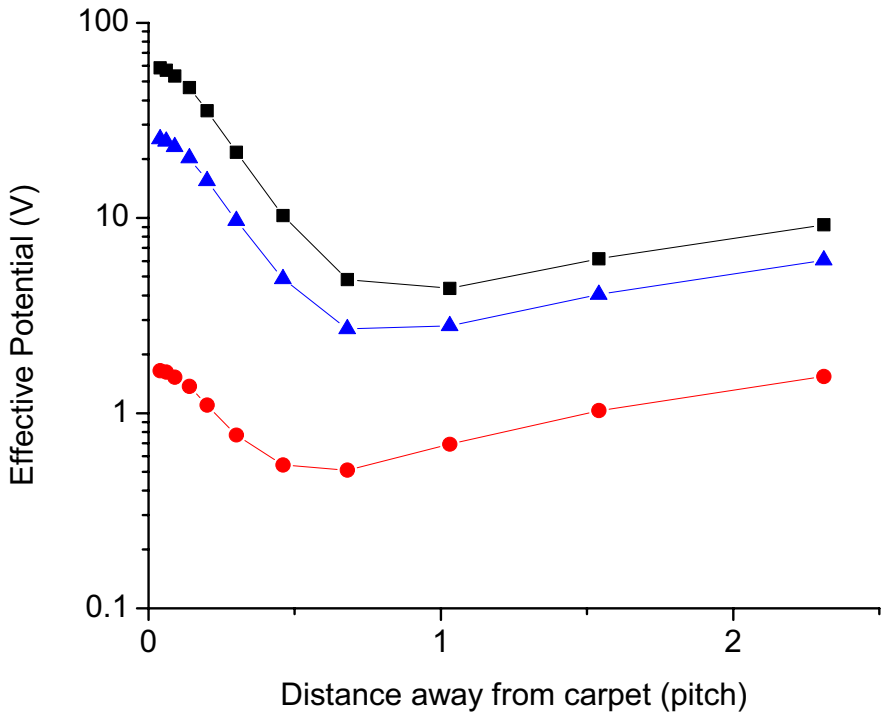

Figure 3.37: Comparison of the calculated effective potential a A=85 ion experiences from a rf carpet with a pitch of 1.5 mm (red circles), 0.38 mm (blue triangles), and 0.25 mm (black squares) in 80 torr of He gas with a driving frequency of 2 MHz, Rf voltage at discharge limit and a push field of 10 V/cm.

Thus, the two rf carpet parameters that can be changed to increase the operating pressure of the rf carpets of reducing the pitch and increasing the rf driving frequency naturally counteract each other. Reducing the pitch to the manufacturing limit of 0.25 mm can easily be accomplished by changing the design sent to the pcb manufacturers. As stated before, this will increase the capacitive load of the rf carpet and bring the resonant frequency down or require the use of multiple circuits or higher rf power. A rf carpet with a 0.25 mm pitch that is 50 cm long will have a capacitive load of approximately 15 nF. Taking a minimum value of 3 μH for the inductance from the secondary winding, wires, etc. for the combined circuit, the rf carpet would have to be broken into approximately 15 segments with a capacitive load of 1 nF each to reach a resonant frequency of only 3 MHz. From the results already described in this section, the rf carpet would have to be driven at a frequency higher than 3.47 MHz to operate with near 100% transport efficiency for the higher pressure regime of the cyclotron gas stopper. For example, to achieve a driving frequency of 6 MHz with a 50 cm rf carpet with a pitch of 0.25 mm would require 64 individual segments and rf circuits!

3.12.3 Transporting ions over long distances

A main requirement for the development of an rf carpet for a cyclotron gas stopper was that it should transport ions over a distance approaching 50 cm, corresponding to the maximum average radius of stopped ions from the cyclotron gas stopper simulations. The stopping radii from simulations for a sample of different ion species at 60 torr in the cyclotron gas stopper is shown in Fig. 3.38. Since Rb ions were primarily studied in this offline characterization, the simulation results for ^{79}Br are most relevant and correspond to a stopping radius and therefore transport distance of approximately 30 cm. Transportation of Rb ions at this distance and greater was achieved at high transport efficiencies and will be presented in this section. Transporting ions over this long distance would also be applicable to the axial transport of ions along a linear gas cell.

The majority of the rf carpets studied had a maximum transport distance of up to 20 cm, and the bulk of the studies and comparisons were for a transport distance of 16 cm.

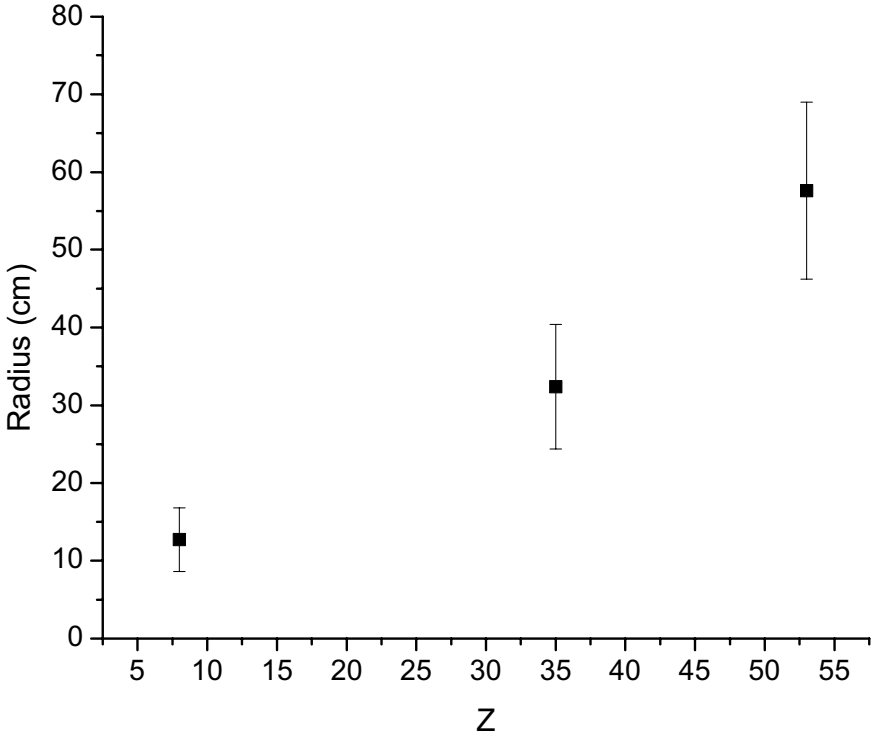

Figure 3.38: Simulated stopping radii for ^{16}O, ^{79}Br, and ^{127}I ions stopped in the cyclotron gas stopper at 60 torr. The stopping radii correspond to the distances the ions would need to be transported along the rf carpet.

Only the final rf carpet design had a large enough electrode structure to transport ions over distances approaching 50 cm. This carpet demonstrated that ions could be transported over that distance and that the electronics to apply the rf and dc components had advanced to the state that one could drive a rf carpet of that size. As discussed in Ch. 3, the maximum panel area for the flex pcb is 45 cm x 60 cm. With a portion of the flex circuit reserved for surface mount components and a physical clamping area, the resultant electrode structure had a maximum transport length of 48 cm.

The technical challenges of transporting ions over long distances using the rf techniques described in Section 3.4, was that the rf carpet had to be segmented into manageable capacitive loads to increase the resonant frequency. At the time of the design, the frequency relationship was not well established determined and the original design had a resonant fre-

quency of 2 MHz. Within the given tolerances, air core coil inductors could be modified and variable capacitors could be used to operate all segments of the rf carpet at a resonant frequency of 2 MHz. The resonant frequency is dictated by the capacitive load of the rf carpet and the tolerances for the 2 MHz system were not sufficient to significantly increase the frequency because of differences in the individual capacitive loads and the entire system could only be driven at a resonant frequency of 2 MHz or less. It is clear from the discussion in section 3.12.2 that increasing the driving frequency would result in a higher transport efficiency regardless of the transport distance. To apply a higher driving frequency than 2 MHz over the entire 48 cm rf carpet requires a redesign.

Another challenge to transporting over longer distances is the maximum dc voltage that could be applied before a discharge occurred across the feed-throughs to the chamber held at electrical ground. This discharge limited the maximum drag and push fields that could be established on the rf carpet. In linear cells, the dc voltages are typically used to establish the drag field at approximately 10 V/cm, but the experimental setup required for testing rf carpets is different. In addition to the dc voltages on the rf carpet needed to establish the drag field, the push electrodes have to be held at an even higher potential to establish the push field. To put things in perspective, a 10 V/cm drag field over 50 cm referenced to electrical ground would require VCarpHi to be 500 V. With the push electrodes 13 cm above the rf carpet, and a desired push field of 10 V/cm, VPushHi would have to be 630 V. These voltages would undergo discharge in the pressure regime for the reference measurements (20 - 30 torr), and so the push and drag fields had to be limited to 3 V/cm at these pressures. In order to compare the data with that for higher pressures, the push and drag fields were maintained at 3 V/cm for the long distance measurements.

Measurements for determining the transport efficiency at different distances were straightforward once the rf carpet electrodes and push electrodes could sustain the appropriate voltages. As with the pressure studies, the applied rf voltage was held at the maximum voltage before rf discharge occurred. The ion source was positioned over the rf carpet and moved to different positions over the rf carpet corresponding to different transport lengths. The

transport efficiency was determined and the ion source was moved to a new position. At every new position, the center of the ion source body was biased at a voltage so that the corresponding electric field between the ion source and the rf carpet matched the push field.

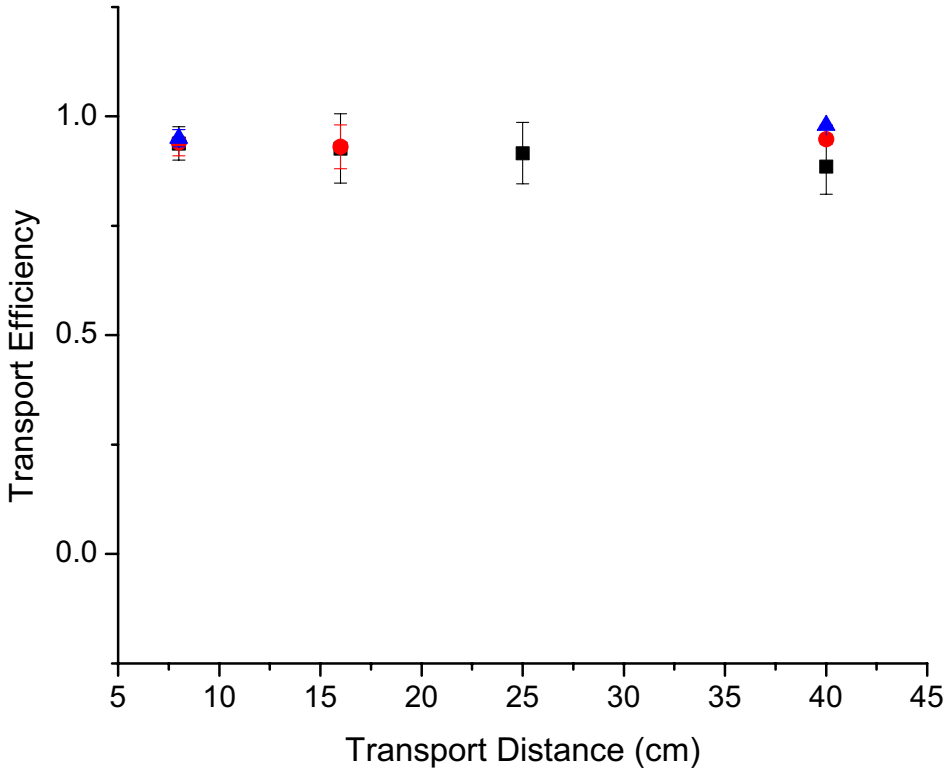

Figure 3.39: Measured transport efficiency at 20 torr (black squares), 40 torr (red circles), and 60 torr (blue triangles) over different transport distances across the rf carpet. Rf carpet parameters: Rf voltage at discharge limit at 2 MHz, Drag Field = 3 V/cm, Push Field = 3 V/cm, $I(Carp) = 500$ pA.

The results of the measurements are shown in Fig. 3.39 and indicate that the rf carpet could be used to transport ions over distances of approximately 40 cm at high transport efficiencies (>90%) depending on the pressure. This distance corresponds to the maximum average stopped radius of ions from the cyclotron gas stopper simulations. It is clear that if the ion motion is stable and well above the rf carpet surface, as in the case of low pressures and low push fields, the ion survives long transport distances at nearly 100% efficiency as

shown in Fig. 3.39. In the case of high pressures and high push fields where ion losses occur on the rf carpet, it is expected that more ion losses would occur as the transport distance is increased, as shown in Fig. 3.40.

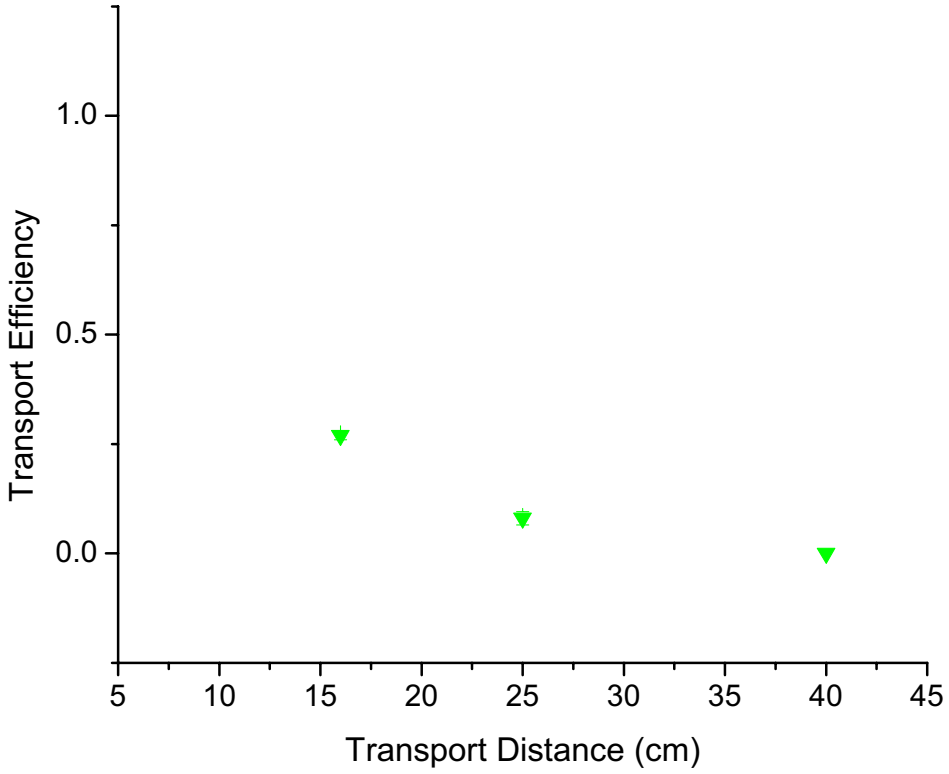

Figure 3.40: Measured transport efficiency at 80 torr over different transport distances across the rf carpet. Rf carpet parameters: Rf voltage at discharge limit at 2 MHz, Drag Field = 3 V/cm, Push Field = 3 V/cm, $I(Carp) = 1$ nA.

On the other hand, the transport efficiency was found to be low but constant for a series of distances which indicated that the losses were localized. This phenomenon is shown in Fig. 3.41, where the data for the 60 torr measurements with an $I(Carp)$=2.5 nA resulted in a relatively constant transport efficiency of approximately 50%. The suggestion is that the ion losses were mainly occurring near the ion source or within 8 cm of the ion source. The constant value of the efficiency at transport distances of 8 cm and 40 cm, suggested that there were no ion losses once past the localized effect of the ion source. Further investigation

showed that $I(Carp)$ also had a large effect on the measured transport efficiency and this is presented in the following section.

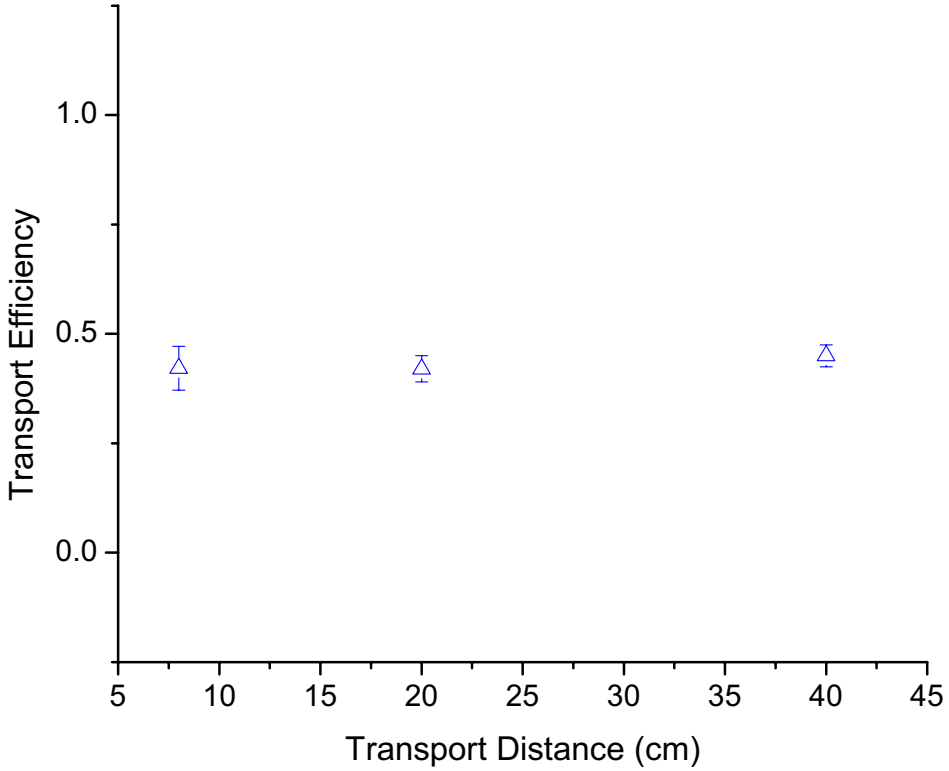

Figure 3.41: Measured transport efficiency at 60 torr with $I(Carp) = 2.0$ nA over different transport distances across the rf carpet. Rf carpet parameters: Rf voltage at discharge limit at 2 MHz, Drag Field = 3 V/cm, Push Field = 3 V/cm.

3.12.4 Effect of ion current and the push field on ion transport

The sensitivity of the transport efficiency to the ion current, $I(Carp)$ was not apparent until long distance transport was possible. Very significant ion losses were observed directly under the ion source. The absolute values of $I(Carp)$ was largely ignored up until that point, as long as ions were impinging on the rf carpet and the transport efficiency could be calculated reliably. The effect of the push field is also part of this section because it was studied at the same time as the variation with $I(Carp)$ because they were the two parameters (aside from

increasing the pressure) that would challenge the operation of the rf carpet. By varying the push field, the effect on the transport efficiency of an opposing electric field on the rf carpet could be determined. Originally, before it was determined that the ion source resulted in localized losses, varying $I(Carp)$ was thought to mainly determine the effect on transport efficiency of the total electric charge moving on the rf carpet.

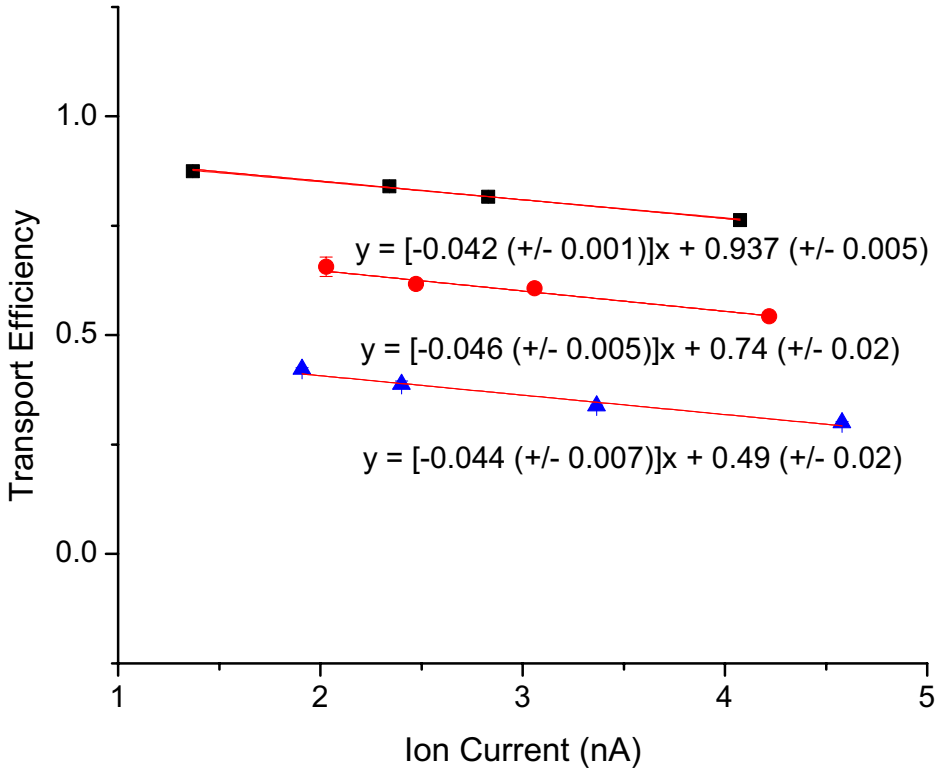

Figure 3.42: Measured transport efficiency at 30 torr with varying $I(Carp)$ for a push field of 10 V/ cm (black squares), 15 V/cm (red circles), and 20 V/cm (blue triangles). Rf carpet parameters: Rf voltage at discharge limit at 2 MHz, Drag Field = 3 V/cm, Transport Distance = 8 cm.

These measurements were conducted by first establishing the appropriate voltages on the rf carpet, the push electrodes, and the ion source. The test chamber was at a static pressure and the rf voltage was 10 $V_{RF,pk-pk}$ under the rf discharge limit. $I(Carp)$ was varied and the transport efficiency was determined for a given distance. Then, the push field was increased and the transport efficiency was determined for a new value of $I(Carp)$ again.

The results of these measurements at 30 torr are shown in Fig. 3.42. The results indicate that, the transport efficiencies decrease linearly with $I(Carp)$. The transport efficiency for the different push fields in the limit of zero ion current (no space charge limit) can be estimated by taking the y-intercept of the linear trends (e.g. $\epsilon = 0.937$ for 10 V/cm).

In order to determine the effect of the push field on the transport efficiency, $I(Carp)$ can be held constant and the push field can be scanned. The measurements at 30 and 60 torr are shown in Fig. 3.43. This can also be inferred, of course, from a slice in constant $I(Carp)$

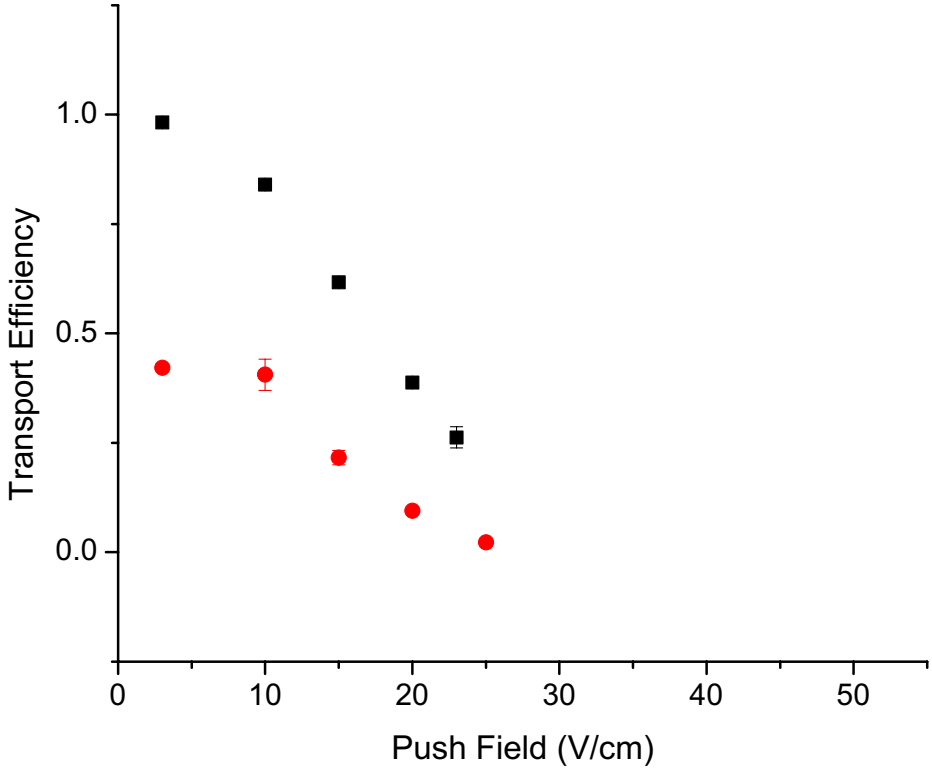

Figure 3.43: Measured transport efficiency at 30 torr (black squares) and 60 torr (red circles) for varying push field strengths. Rf carpet parameters: Rf voltage at discharge limit at 2 MHz, Drag Field = 3 V/cm, Push Field = 3 V/cm, Transport Distance = 8 cm, $I(Carp)$ = 2 nA.

for the 30 torr measurements of the results shown in Fig. 3.42. Since it was impossible to measure the transport efficiency without ion current, simulations using HS-collisions discussed in Sec. 2.6.3 (which don't take into account any space charge effects) were conducted

to determine if the simulated transport efficiencies matched up with the 'no space charge' limit taken from the y-intercepts of the $I(Carp)$ studies. This was done as an attempt to decouple the push field effects from the localized space charge effects produced from the ion source. The comparison between the HS-collision simulations, the 'no space charge' limit, and experimental measurements taken at $I(Carp) = 2$ nA for a case of 30 torr is shown in Fig. 3.44. The comparison shows a stark disagreement between the HS-collision simulations and the experimental measurements. The large discrepancy between the HS-collision simulations and the experiment could possibly be due to the fact that the effects of the $I(Carp)$ and the push field could not be properly disentangled. Thus, independent simulations that

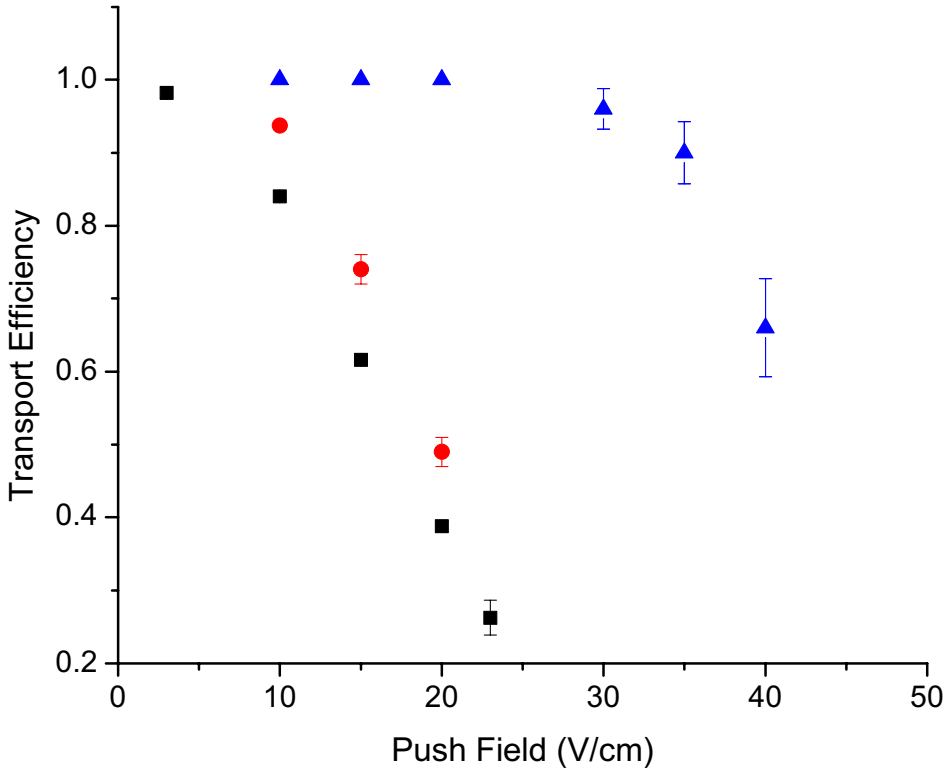

Figure 3.44: Transport efficiency at 30 torr for a varying push field for experiment (black squares), the 'no space charge limit' inferred from experiment (red circles), and HS-collision simulations (blue triangles). Rf carpet parameters: Rf voltage at discharge limit at 2 MHz, Drag Field = 3 V/cm, Push Field = 3 V/cm, Experimental transport distance = 8 cm, Simulated transport distance = 5 cm, $I(Carp) = 2$ nA.

incorporated detailed space charge effects [22] were conducted in an attempt to include all the known processes in the transport of ions with rf carpets: the effects of the buffer gas, the push field, and the space charge. Taking the more interesting gas pressure of 60 torr, a comparison between the HS-collisions simulations, the space charge simulations, and the experimental results is shown in Fig. 3.45. The space charge effects bring the simulation results closer to the data but they still do not match the experimental measurements.

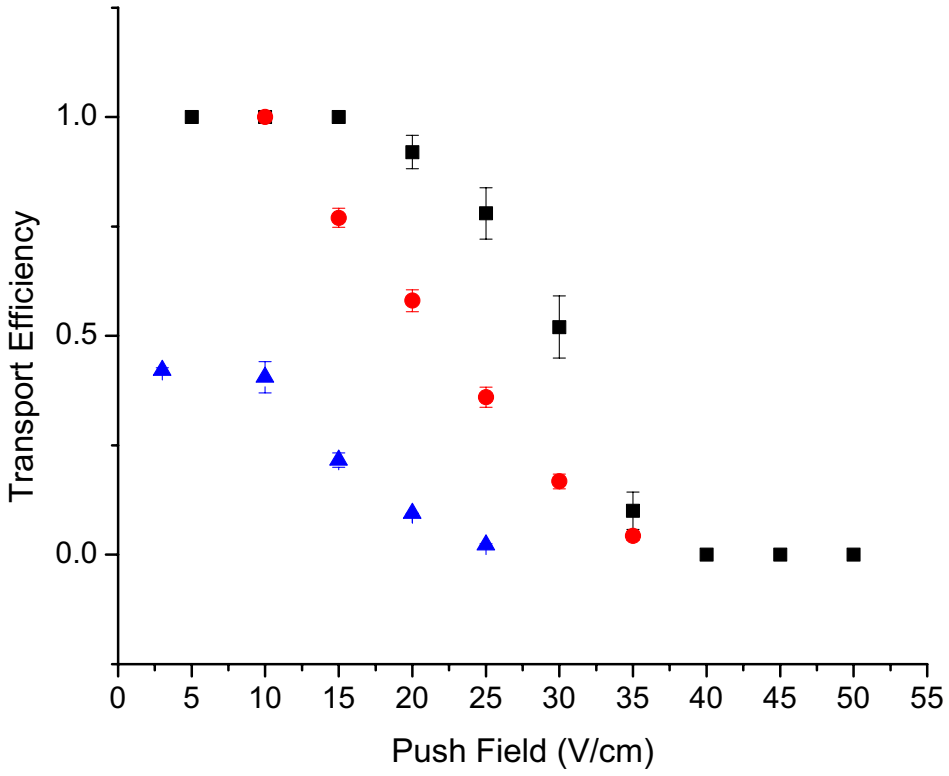

Figure 3.45: Transport efficiency at 60 torr for a varying push field for experiment (blue triangles), space charge simulations (red circles), and HS-collision simulations (black squares). Rf carpet parameters: Rf voltage at discharge limit at 2 MHz, Drag Field = 3 V/cm, Push Field = 3 V/cm, Experimental transport distance = 8 cm, Simulated transport distance = 5 cm, $I(Carp) = 2$ nA.

3.12.5 Ion Extraction from the rf carpet

The last main requirement for the rf carpet studies was to demonstrate that ions could be extracted from the rf carpet. Since the main purpose of the rf carpet was to guide thermalized ions towards the center of the cyclotron gas stopper and bring them to an extraction orifice, it was important to demonstrate that ions could also be extracted efficiently from the rf carpet. Extraction of ions from an rf carpet has already been demonstrated by M. Wada [3], and he contributed a small rf carpet with an aperture in the center. This small rf carpet, called here the extraction rf carpet, was excellently suited for the transition between the high gas pressure in the stopping chamber and the differentially pumped region. A photograph of the circuit board is shown in Fig. 3.46.

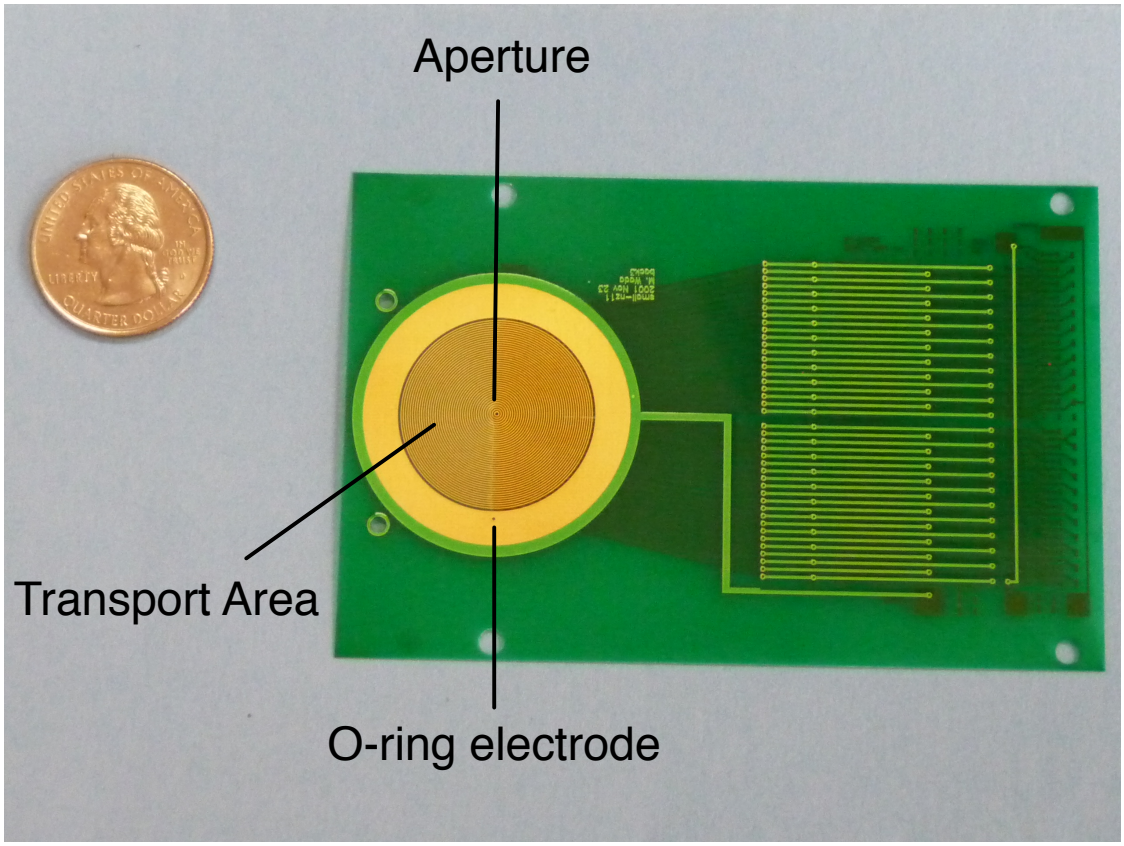

Figure 3.46: Photograph of the extraction rf carpet from Wada [3] with an aperture used for ion extraction measurements. The outer o-ring electrode was used to confine the ions on the rf carpet.

Table 3.3: Parameters for the extraction rf carpet used in extraction measurements.

Parameter	Value
Outer radius of rf electrodes	2.5 cm
Pitch	0.3 mm
Electrode width	0.15 mm
Extraction hole diameter	0.5 mm
$V_{RF,pk-pk}$	< 70 V
Rf frequency	5 - 8 MHz

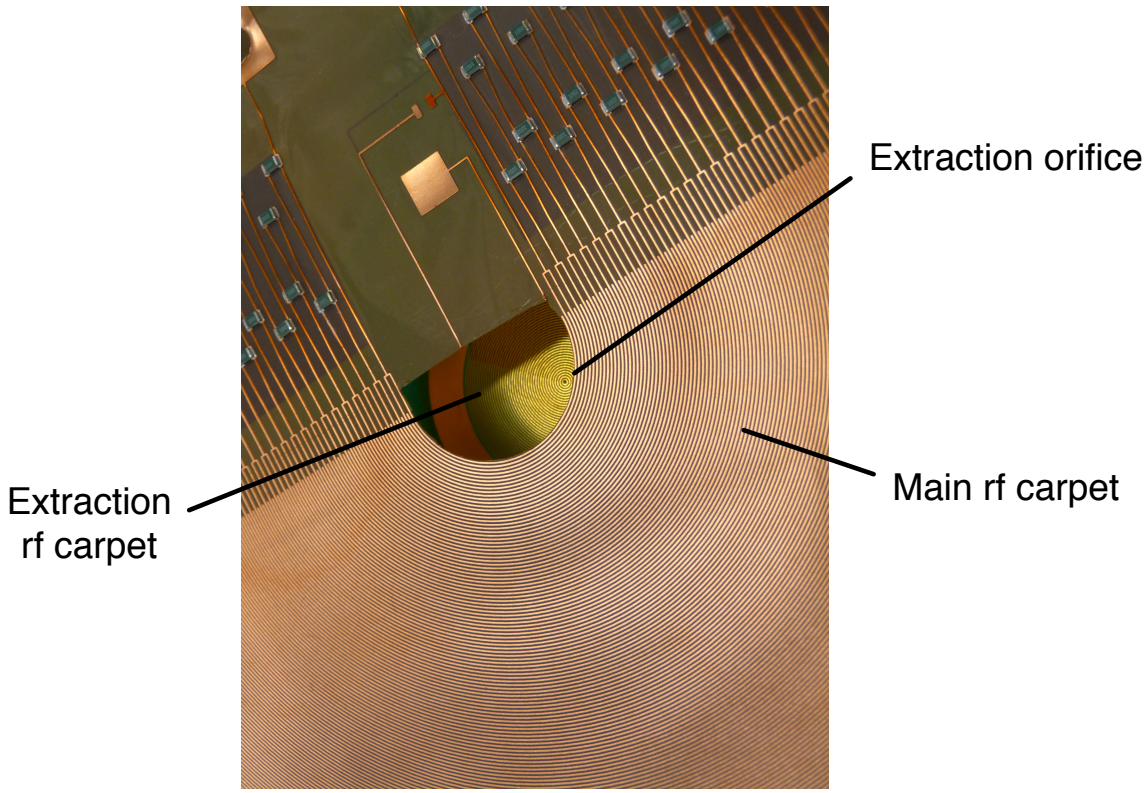

Figure 3.47: Photograph of the setup used for ion extraction. The extraction rf carpet is mounted below the main (large) rf carpet and a collection electrode is mounted below the extraction rf carpet (not shown).

The exact parameters of the extraction rf carpet are listed in Table 3.3. The center aperture diameter was in the sub-mm region which was typical for apertures in gas stopping stations. A small transport area and a small pitch allowed for a high resonant frequency and an increased effective potential, in which the advantages of both parameters have been discussed in previous sections. In fact, the use of the extraction rf carpet was planned during the design phase of the last large rf carpet. Thus, after the suite of transport measurements were completed with the large rf carpet, a hole was cut into the pcb to remove the collection electrode so that the extraction rf carpet could be mounted below the carpet. A photograph of this arrangement is shown in Fig. 3.47. To determine the extraction efficiency from the extraction rf carpet, another collection electrode was mounted below the extraction rf carpet.

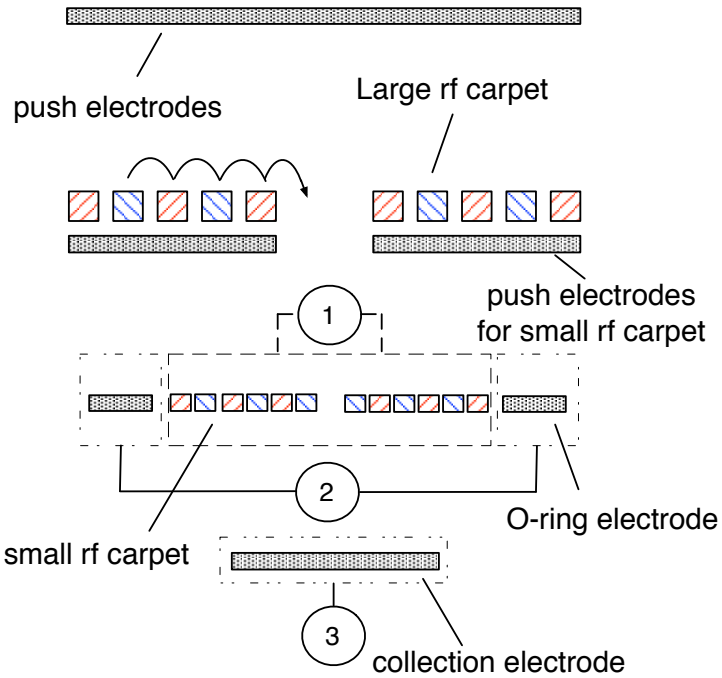

Figure 3.48: Schematic diagram of the setup used for ion extraction. The red and blue hatched marks represent the electrodes in which rf was applied. The dotted electrodes represent the electrodes in which dc voltages were applied. The different collection electrodes for the different transport modes are labeled with their appropriate number designation. Transport mode 1 collected on the extraction rf carpet electrodes encompassed by the dash line. Transport mode 2 collected on the o-ring electrode and is encompassed by the dot-dash line. Transport mode 3 collected on the collection electrode mounted below the extraction rf carpet encompassed by the dot-dot-dash line.

The extraction rf carpet was operated in an identical manner as the main rf carpet as described in Sec. 3.4. The only difference in general operation was the method of applying the rf voltages to each electrode. The device used surface mount capacitors rather than the new technique used to apply the rf underneath the main rf carpet. The smaller transport area and the capacitive load allowed for a resonant frequency in the 5 - 8 MHz range.

It was important to differentiate the ion losses at different parts of the transport process in order to determine which transport stage might need improvement. Thus, the transport efficiency had to be determined for three different transport modes: 1) Transport from the top rf carpet to the extraction rf carpet, 2) Transport to the extraction rf carpet and along the extraction rf carpet, and 3) Transport to the extraction rf carpet and through the central aperture to the collection electrode. The extraction rf carpet electrodes could be used as a collection electrode for transport mode 1 and the o-ring surrounding the extraction rf carpet could be used as a collection electrode for transport mode 2 with reversed drag field on the extraction rf carpet. A schematic of the setup showing the three transport modes is shown in Fig. 3.48.

Transport mode 1 was achieved by establishing the voltages on the large rf carpet electrodes, push electrodes, and the ion source as mentioned in the previous sections. In addition to this, the underside of the main rf carpet was biased with a dc voltage to act as a set of push electrodes in the region between the two rf carpets. The extraction rf carpet was then separately biased and used as the collection electrode. The transport efficiency for transport mode 1 matched the results for pure surface transport. Thus, there were no ion losses during the transport between the large rf carpet and the extraction rf carpet.

Transport mode 2 was achieved by operating the large rf carpet and push electrodes for the extraction rf carpet as in transport mode 1 and also applying a rf voltage and a drag field on the small rf carpet. However, the dc gradient on the extraction rf carpet directed the ions towards the outer radius (rather than towards the inner radius) to be collected on the o-ring that was biased separately. The set of push electrodes for the extraction rf carpet did not have a dc gradient, so the push fields will be presented as a range. The transport efficiency

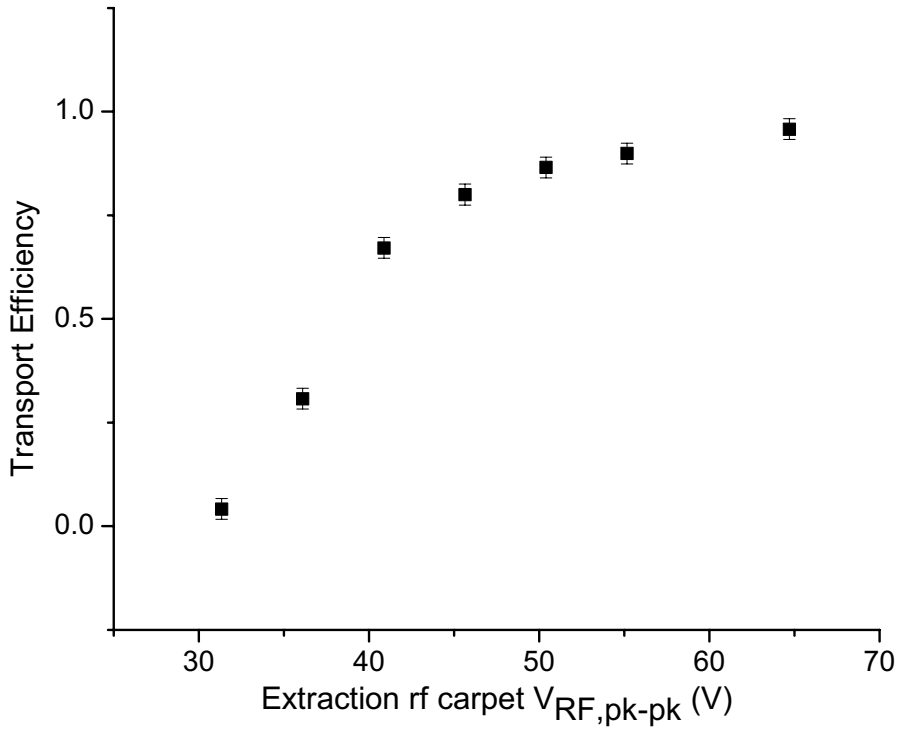

Figure 3.49: Measured transport efficiency for transport mode 2 (collection on the o-ring electrode) as a function of the rf voltage applied to the extraction rf carpet at a gas pressure of 40 torr. Main rf carpet parameters: Rf voltage at discharge limit at 2 MHz, Drag Field = 3 V/cm, Push Field = 3 V/cm, Transport distance before large hole = 8 cm. Extraction rf carpet parameters: Frequency = 5.28 MHz, Drag Field = 8 V/cm, Push Field = 20 - 27 V/cm.

as a function of applied rf voltage on the extraction rf carpet for transport mode 2 is shown in Fig. 3.49 and suggest that none of the ions were lost once they reach the extraction rf carpet. Also, pure transport with the dc fields did not occur because no transported ions were observed when the rf voltages were reduced on the extraction rf carpet.

Transport mode 3 had the same operation as transport mode 2, except for the dc gradient on the extraction rf carpet directed the ions towards the inner radius and the ions were collected on an electrode mounted directly below the aperture of the extraction rf carpet. The o-ring electrode used to collect ions in transport mode 2 was biased to confine the ions on the extraction rf carpet. The electric field between the innermost ring of the extraction

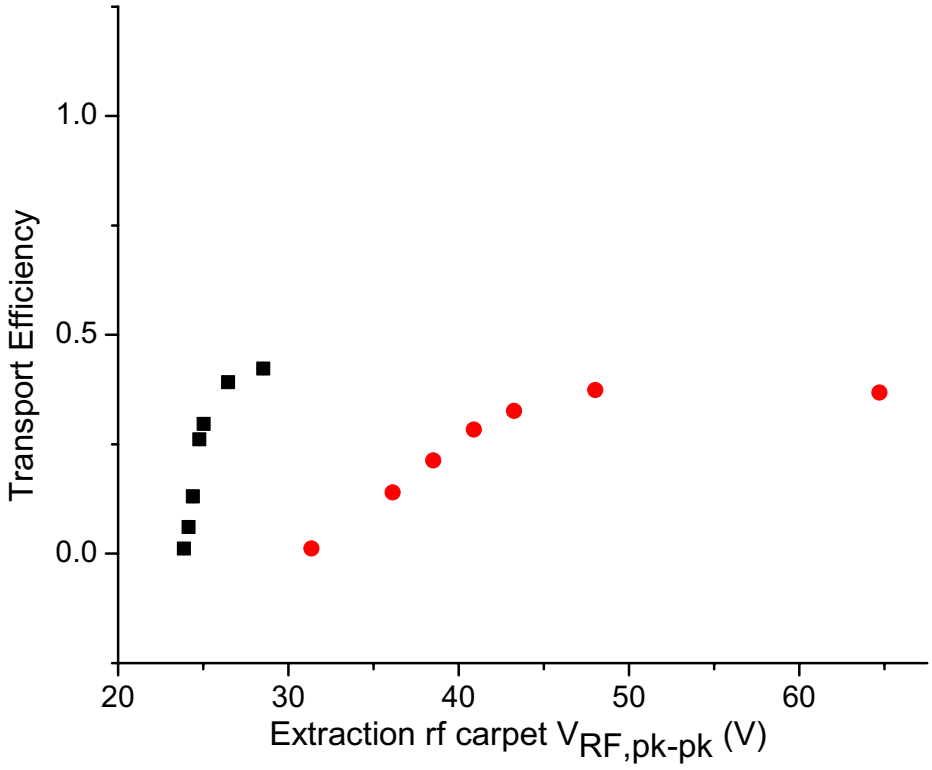

Figure 3.50: Measured transport efficiency for transport mode 3 (collection through the aperture) as a function of the rf voltage applied to the extraction rf carpet at a gas pressure of 40 torr at an extraction rf carpet frequency of 5.28 MHz (red circles) and 8.56 MHz (black squares). Main rf carpet parameters: Rf voltage at discharge limit at 2 MHz, Drag Field = 3 V/cm, Push Field = 3 V/cm, Transport distance before large hole = 8 cm. Extraction rf carpet parameters: Drag Field = 8 V/cm, Push Field = 20 - 27 V/cm, Collect Pull Field = 25 V/cm.

carpet and the collection electrode is referred to as the collect pull field. The results for transport mode 3 for two different extraction rf carpet frequencies are shown in Fig. 3.50. In this transport mode, ion losses were observed through the aperture of the extraction rf carpet. The profile of the transport efficiency curves show that increasing the rf voltage would not substantially improve the ion survival for either rf frequency. In addition to investigating the transport efficiency through the aperture, this transport mode provided further evidence for the advantage of using a higher rf frequency on the rf carpets, as can be seen by the much steeper response curve to the applied rf voltage for the rf frequency of 8.56 MHz compared

to 5.28 MHz. Since transport mode 2 had nearly 100% efficiency, these losses are attributed to the region close to the aperture. It should be noted that gas flow was not present in this experimental setup, and would reduce these losses in an operational device setup. However, ion losses could be expected due to space charge losses near the orifice. Further confirmation that ion losses occurred near the aperture region and that the presence of gas flow would reduce these losses, is shown in the sensitivity of the transport efficiency to the strength of the collect pull field in Fig. 3.51. The stronger the collect pull field, the deeper the electric field penetration through the aperture which pulls the ions through the aperture when the ions are at the innermost radius.

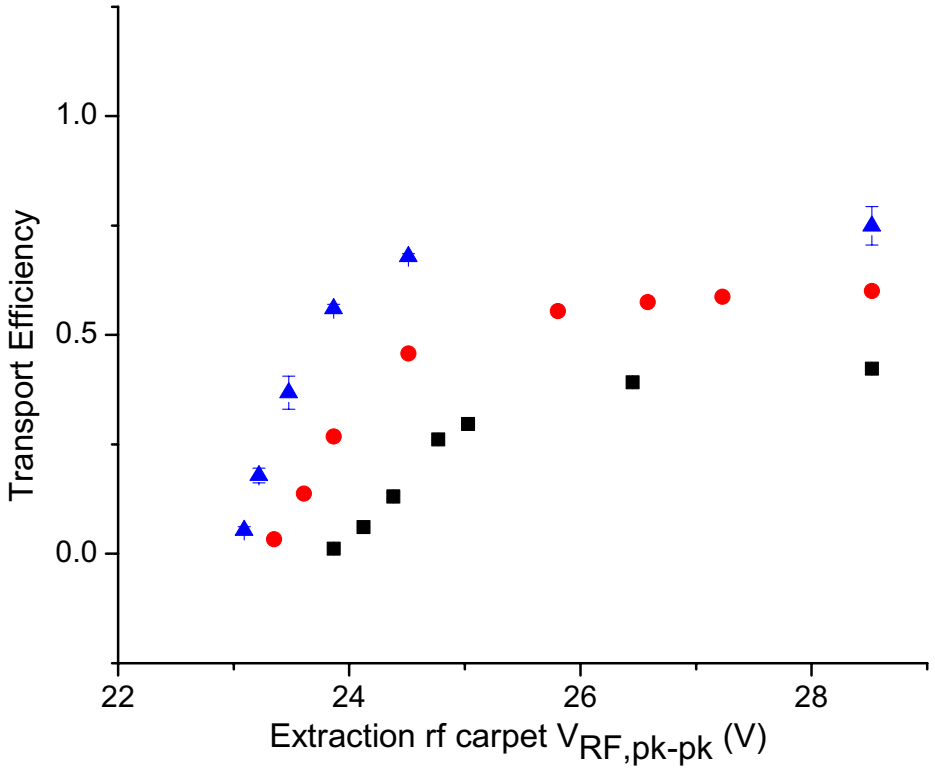

Figure 3.51: Measured transport efficiency for transport mode 3 (collection through the aperture) at Collect Pull Fields of 25 V/cm (black squares), 40 V/cm (red circles), and 70 V/cm (blue triangles) as a function of the rf voltage applied to the extraction rf carpet at a gas pressure of 40 torr. Main rf carpet parameters: Rf voltage at discharge limit at 2 MHz, Drag Field = 3 V/cm, Push Field = 3 V/cm, Transport distance before large hole = 8 cm. Extraction rf carpet parameters: Drag Field = 8 V/cm, Push Field = 20 - 27 V/cm.

The ion extraction measurements also revealed a high transport efficiency in the presence of a strong push field on the extraction rf carpet. The push field that the extraction rf carpet was able to sustain was (20 - 27 V/cm) while still transporting ions. Recall that such high fields resulted in all the ions being lost in the push studies for the main rf carpet. This increased survivability can be directly attributed to the reduced pitch, the increased rf frequency, and the shorter transport distance of this device.

3.12.6 Ion drift time measurements

For rare isotope studies, it is important for the rf carpet to transport ions fast enough to minimize decay losses. The ion drift times for these rf carpets are dictated by the drag field. The drift times predicted by ion mobilities were compared with measurements and generally confirmed the expected ion transport times along the rf carpet.

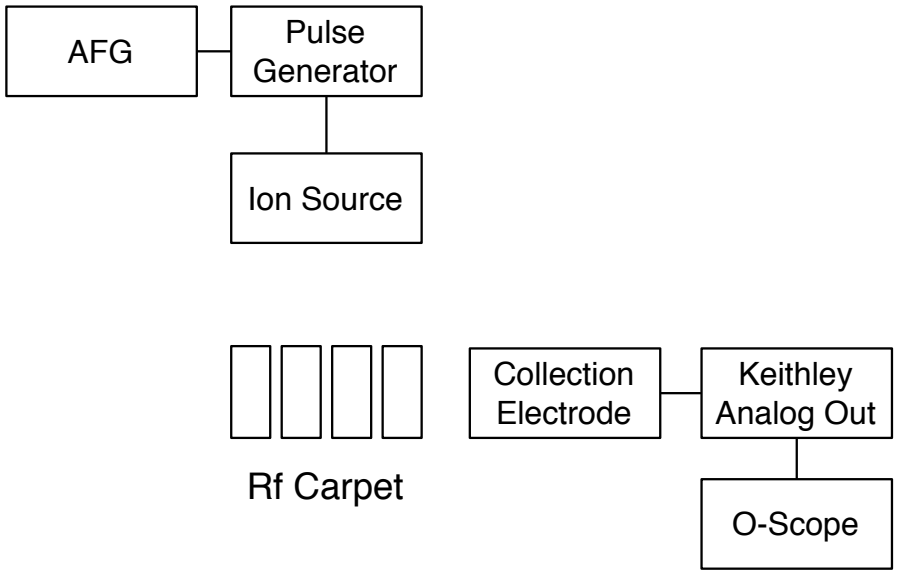

Figure 3.52: Schematic used for the timing measurements.

These measurements were conducted by using an Agilent 33120A arbitrary waveform generator (AFG) to provide a 5 Hz square waveform as an external trigger for a pulse generator that pulsed the ion source (On/Off). The ion current was then measured on the collection electrode by observing the analog output of the Keithley picoammeter on a dig-

ital oscilloscope. In this setup, transport efficiencies were not obtained. A schematic of the experimental setup is shown in Fig. 3.52.

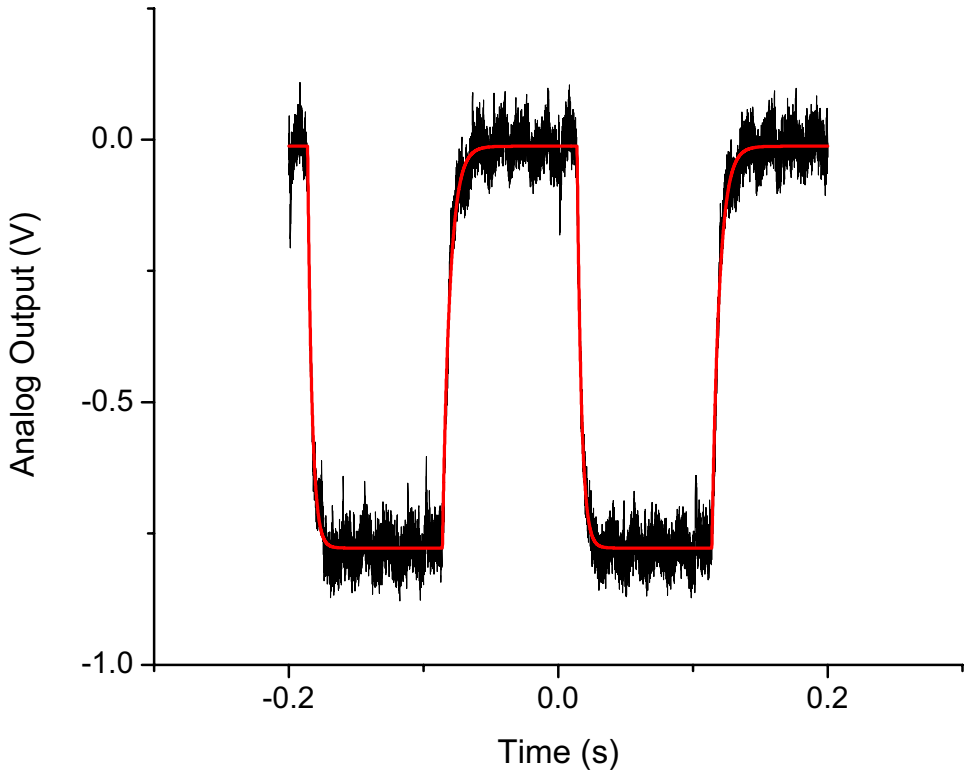

Figure 3.53: Measured pulse train (black) and fit curve (red) at 40 torr for rf carpet parameters: Frequency = 3.47 MHz, Drag Field = 3 V/cm, Push Field = 3 V/cm, Transport Distance = 14.4 cm.

A sample of one of the pulse trains along with a Chi-square minimized curve fit from Igor Pro 9 [23] using a sawtooth function modified by two exponential functions for the rise and fall times is shown in Fig. 3.53. The drift time can be extracted from these fit coefficients and the comparison between a set of sample measurements and the predicted ion mobilities is shown in Fig. 3.54. There is excellent agreement between the predictions and the measurements that confirms the ion transport times follow the expected ion mobilities. From these measurements, ion transport times will be directly given by the drag field which is itself limited by the maximum dc voltage that can be applied without incurring discharge. Ion transport speeds were the same regardless of the rf frequency studied (2 MHz and 3.47

MHz). This problem was discussed in Sec. 3.10.3. We can predict the transport times of an ion with a $K_0 = 20$ cm^2/(V·s) over a 50 cm rf carpet with a typical drag field of 10 V/cm at 80 torr will have a transport time of approximately 24 ms. The maximum drag fields are indeed a known limitation in current gas stopping stations and designs to apply a drag field greater than 30 V/cm (Savard) and 100 V/cm (KVI) at 100 mbar are currently being investigated.

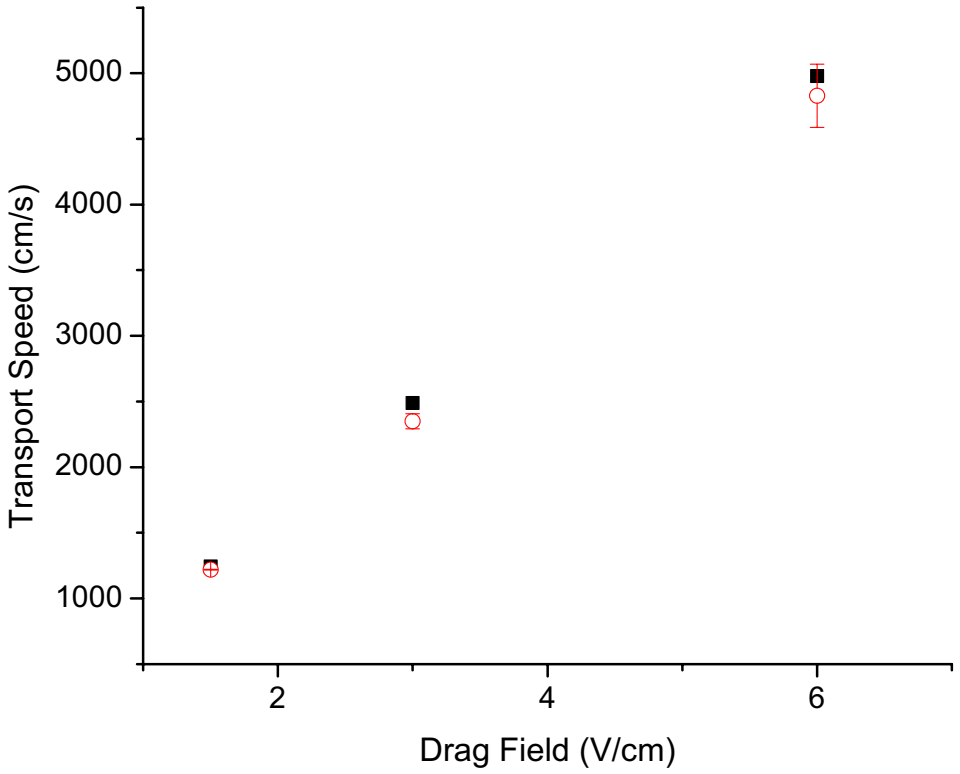

Figure 3.54: Comparison of the measured ion transport speed (open red circles) and the predicted ion transport speeds (black squares) from ion mobility calculations. Rf carpet parameters: Pressure = 20 torr, Frequency = 2 MHz, 3.47 MHz, Push Field = 3 V/cm, Transport Distance = 24 cm.

Chapter 4

Summary and Outlook

In this work, a feasible extraction scheme for a cyclotron gas stopper using rf carpets was developed and characterized. The main requirements of efficient transport of thermal ions in the pressure range of a prospective cyclotron gas stopper, for the required distances of the cyclotron gas stopper, and extraction of the ions from the rf carpet were satisfied.

The rf carpet was demonstrated to transport ions at $\geq$80% efficiency at gas pressures up to 80 torr, which is within the operating pressure range of the cyclotron gas stopper. Ion transport over a distance of 40 cm at pressures up to 60 torr was also achieved at near 100% efficiency. This long distance corresponded to the average distance the ions would have to be transported to the extraction orifice located in the central region of the proposed cyclotron gas stopper. The extraction of ions from the rf carpet was also successfully demonstrated with an efficiency of approximately 75% efficiency without gas flow.

In comparison to the rf carpet from RIKEN with a diameter of 3 cm and a subsequent transport distance of 1.5 cm, this work has demonstrated the transport of ions over an order of magnitude larger distance. Attempts at RIKEN to operate larger rf carpets were hindered due to heating issues [4]. The use of resonant circuits, allowed the successful operation of rf carpets with much larger sizes with less than 1 W of power consumption. The drawbacks of using such techniques are also described in this text. The other experimental systems developed for gas catchers at GSI [24] and Argonne [25], are constructed using discrete

electrodes with a typical electrode pitch on the order of 1 mm, rather than the sub-mm pitch that can be achieved with rf carpets. The rf frequency used in these devices was $\leq$ 1 MHz. In this work, the smallest pitch size studied was 0.38 mm, which showed a clear advantage over a pitch size of 1.5 mm in experiment. The advantages of increasing the rf frequency were also shown in the present measurements. The rf carpet studied in this work has a smaller pitch and increased rf frequency over the ion-guiding devices in the GSI and Argonne gas catchers. From these two parameters that were shown to have the largest impact on transport efficiency, it can be inferred that the rf carpet studied in this work would have a superior transport efficiency than existing systems.

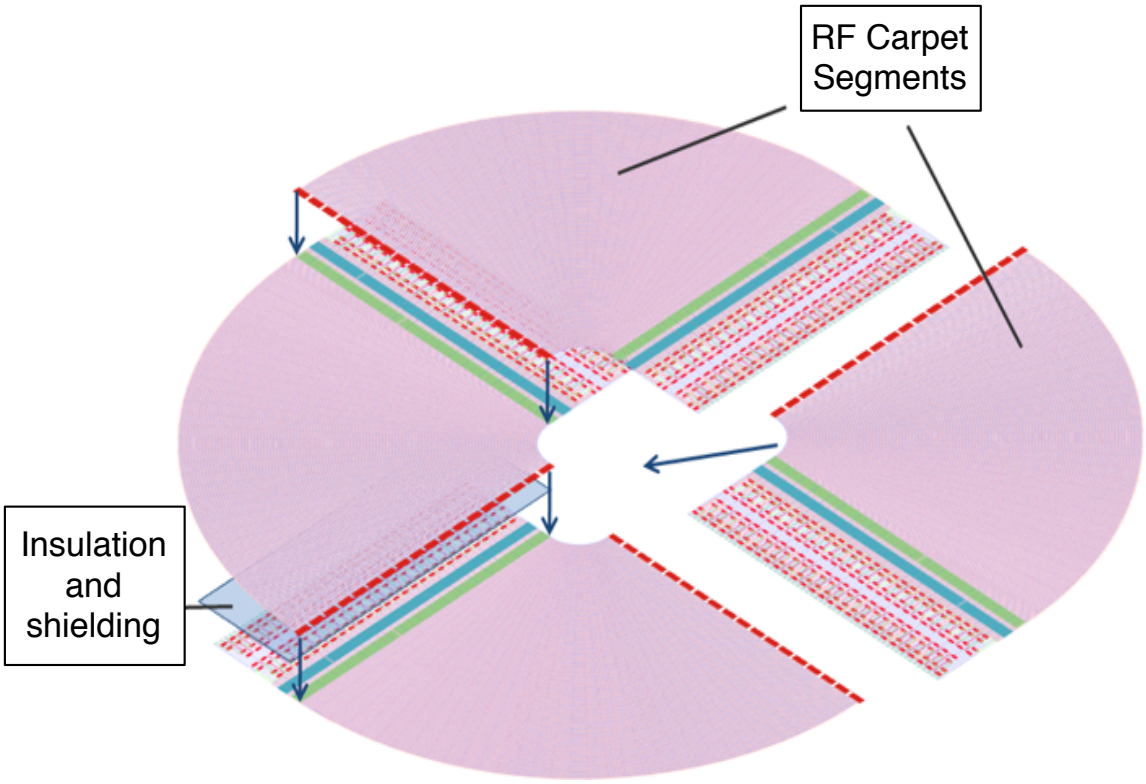

Figure 4.1: Design and arrangement of a series of rf carpets that would allow for a rf carpet coverage of 1 meter in diameter.

Though the results in this work have demonstrated transport distances of 40 cm, the proposed cyclotron gas stopper will require a rf carpet covering an area with a 1 meter diameter. Given the present manufacturing limits of 45 x 60 cm, it would be impossible to cover this area with only one rf carpet. Thus, a method to arrange a series of carpets

azimuthally to cover the full area was developed but not yet fabricated. The technique requires a 4 Cu-layer flex pcb material (Cu-Kapton-Cu-Kapton-Cu-Kapton-Cu) instead of the 2 Cu-layer (Cu-Kapton-Cu) flex pcb material used in this work. These additional Cu layers allow the routing lines for the dc and rf voltages to all be located on one edge of a rf carpet segment while allowing room for a set of dc electrodes arranged on the other edge of the rf carpet segment. These dc electrodes will be responsible for establishing the electric fields in the transition region between two rf carpets pieces. The concept and the orientation of four sectors that would cover the area is shown in Fig. 4.1.

Bibliography

Bibliography

[1] D.J. Morrissey. Extraction of thermalized projectile fragments from gas. *European Physical Journal - Special Topics*, 150(1):365 – 366, 2007.

[2] G. Bollen, D.J. Morrissey, and S. Schwarz. A study of gas-stopping of intense energetic rare isotope beams. *Nuclear Instruments and Methods in Physics Research Section A: Accelerators, Spectrometers, Detectors and Associated Equipment*, 550(1-2):27 – 38, 2005.

[3] Michiharu Wada, Yoshihisa Ishida, Takashi Nakamura, Yasunori Yamazaki, Tadashi Kambara, Hitoshi Ohyama, Yasushi Kanai, Takao M. Kojima, Youichi Nakai, Nagayasu Ohshima, Atsushi Yoshida, Toshiyuki Kubo, Yukari Matsuo, Yoshimitsu Fukuyama, Kunihiro Okada, Tetsu Sonoda, Shunsuke Ohtani, Koji Noda, Hirokane Kawakami, and Ichiro Katayama. Slow ri-beams from projectile fragment separators. *Nuclear Instruments and Methods in Physics Research Section B: Beam Interactions with Materials and Atoms*, 204:570 – 581, 2003. 14th International Conference on Electromagnetic Isotope Separators and Techniques Related to their Applications.

[4] A. Takamine, M. Wada, Y. Ishida, T. Nakamura, K. Okada, Y. Yamazaki, T. Kambara, Y. Kanai, T.M. Kojima, Y. Nakai, N. Oshima, A. Yoshida, T. Kubo, S. Ohtani, K. Noda, I. Katayama, P. Hostain, V. Varentsov, and H. Wollnik. Space-charge effects in the catcher gas cell of a rf ion guide. *Review of Scientific Instruments*, 76:103503–1–103503–6, 2005.

[5] L. Weissman, D. A. Davies, P. A. Lofy, and D. J. Morrissey. Stopping energetic heavy-ions in one-bar helium: broad incident momentum distributions. *Nuclear Instruments and Methods in Physics Research Section A: Accelerators, Spectrometers, Detectors and Associated Equipment*, 531(3):416 – 427, 2004.

[6] L. Weissman, D.J. Morrissey, G. Bollen, D.A. Davies, E. Kwan, P.A. Lofy, P. Schury, S. Schwarz, C. Sumithrarachchi, T. Sun, and R. Ringle. Conversion of 38ca/37k projectile fragments into thermalized ion beams. *Nuclear Instruments and Methods in Physics Research Section A: Accelerators, Spectrometers, Detectors and Associated Equipment*, 540(2-3):245 – 258, 2005.

[7] L. Weissman, D. A. Davieas, P. A. Lofy, and D. J. Morrissey. Stopping energetic heavy ions in one-bar helium: narrow incident momentum distributions. *Nuclear Instruments and Methods in Physics Research Section A: Accelerators, Spectrometers, Detectors and Associated Equipment*, 522(3):212 – 222, 2004.

[8] G. Bollen, D. Davies, M. Facina, J. Huikari, E. Kwan, P. A. Lofy, D. J. Morrissey, A. Prinke, R. Ringle, J. Savory, P. Schury, S. Schwarz, C. Sumithrarachchi, T. Sun, and L. Weissman. Experiments with thermalized rare isotope beams from projectile fragmentation: A precision mass measurement of the superallowed β emitter ^{38}ca. *Phys. Rev. Lett.*, 96(15):152501, Apr 2006.

[9] G. Sikler, D. Ackermann, F. Attallah, D. Beck, J. Dilling, S. A. Elisseev, H. Geissel, D. Habs, S. Heinz, F. Herfurth, F. Heberger, S. Hofmann, H. J. Kluge, C. Kozhuharov, G. Marx, M. Mukherjee, J. Neumayr, W. R. Pla, W. Quint, S. Rahaman, D. Rodrguez, C. Scheidenberger, M. Tarisien, P. Thirolf, V. Varentsov, C. Weber, and Z. Zhou. First on-line test of shiptrap. *Nuclear Instruments and Methods in Physics Research Section B: Beam Interactions with Materials and Atoms*, 204:482 – 486, 2003. 14th International Conference on Electromagnetic Isotope Separators and Techniques Related to their Applications.

[10] G. Savard, J. Clark, C. Boudreau, F. Buchinger, J. E. Crawford, H. Geissel, J. P. Greene, S. Gulick, A. Heinz, J. K. P. Lee, A. Levand, M. Maier, G. Mnzenberg, C. Scheidenberger, D. Seweryniak, K. S. Sharma, G. Sprouse, J. Vaz, J. C. Wang, B. J. Zabransky, and Z. Zhou. Development and operation of gas catchers to thermalize fusion-evaporation and fragmentation products. *Nuclear Instruments and Methods in Physics Research Section B: Beam Interactions with Materials and Atoms*, 204:582 – 586, 2003. 14th International Conference on Electromagnetic Isotope Separators and Techniques Related to their Applications.

[11] G. Bollen, C. Campbell, S. Chouhan, C. Gunaut, D. Lawton, F. Marti, D.J. Morrissey, J. Ottarson, G. Pang, S. Schwarz, A.F. Zeller, and P. Zavodszky. Manipulation of rare isotope beams - from high to low energies. *Nuclear Instruments and Methods in Physics Research Section B: Beam Interactions with Materials and Atoms*, 266(19-20):4442 – 4448, 2008. Proceedings of the XVth International Conference on Electromagnetic Isotope Separators and Techniques Related to their Applications.

[12] M. Sternberg and G. Savard. A study of the cyclotron gas-stopping concept for the production of rare isotope beams. *Nuclear Instruments and Methods in Physics Research Section A: Accelerators, Spectrometers, Detectors and Associated Equipment*, 596(3):257 – 268, 2008.

[13] Mark Huyse, Marius Facina, Yuri Kudryavtsev, Piet Van Duppen, and ISOLDE collaboration. Intensity limitations of a gas cell for stopping, storing and guiding of radioactive ions. *Nuclear Instruments and Methods in Physics Research Section B: Beam Interactions with Materials and Atoms*, 187(4):535 – 547, 2002.

[14] H.G. Dehmelt. Radiofrequency spectroscopy of stored ions - i: Storage. *Adv. At. Mol. Phys.*, 3:53–72, 1967.

[15] Raymond E. March and Richard J. Hughes. *Quadrupole Storage Mass Spectrometry*. John Wiley and Sons, 1989.

[16] Taeman Kim, Aleksey V. Tolmachev, Richard Harkewicz, David C. Prior, Gordon Anderson, Harold R. Udseth, Richard D. Smith, Thomas H. Bailey, Sergey Rakov, and

Jean H. Futrell. Design and implementation of a new electrodynamic ion funnel. *Analytical Chemistry*, 72(10):2247–2255, 2000.

[17] S. Schwarz. Rf ion carpets: The electric field, the effective potential, operational parameters and an analysis of stability. *International Journal of Mass Spectrometry*, 299(2-3):71 – 77, 2011.

[18] T. Hasegawa and K. Uehara. Dynamics of a single particle in a paul trap in the presence of the damping force. *Applied Physics B*, 61:159 – 163, 1995.

[19] http://www.simion.com.

[20] A. James Diefendefer. *Principles of Electronic Instrumentation*. Brooks/Cole, 1994.

[21] J. Park, I. Henins, H.W. Herrmann, and G.S. Selwyn. Gas breakdown in an atmospheric pressure radio-frequency capacitive plasma source. *Journal of Applied Physics*, 89:15 – 19, 2001.

[22] R. Ringle. 3dcylpic–a 3d particle-in-cell code in cylindrical coordinates for space charge simulations of ion trap and ion transport devices. *International Journal of Mass Spectrometry*, 303(1):42 – 50, 2011.

[23] http://www.wavemetrics.com.

[24] J.B. Neumayr, L. Beck, D. Habs, S. Heinz, J. Szerypo, P.G. Thirolf, V. Varentsov, F. Voit, D. Ackermann, D. Beck, M. Block, Z. Di, S.A. Eliseev, H. Geissel, F. Herfurth, F.P. Heberger, S. Hofmann, H.-J. Kluge, M. Mukherjee, G. Mnzenberg, M. Petrick, W. Quint, S. Rahaman, C. Rauth, D. Rodrguez, C. Scheidenberger, G. Sikler, Z. Wang, C. Weber, W.R. Pla, M. Breitenfeldt, A. Chaudhuri, G. Marx, L. Schweikhard, A.F. Dodonov, Y. Novikov, and M. Suhonen. The ion-catcher device for shiptrap. *Nuclear Instruments and Methods in Physics Research Section B: Beam Interactions with Materials and Atoms*, 244(2):489 – 500, 2006.

[25] W. Trimble, G. Savard, B. Blank, J.A. Clark, F. Buchinger, T. Cocolios, J.E. Crawford, A. Frankel, J.P. Greene, S. Gulick, J.K.P. Lee, A. Levand, M. Portillo, K.S. Sharma, J.C. Wang, B.J. Zabransky, and Z. Zhou. Development and first on-line tests of the ria gas catcher prototype. *Nuclear Physics A*, 746:415 – 418, 2004. Proceedings of the Sixth International Conference on Radioactive Nuclear Beams (RNB6).